Optical High Temperature Sensor Based on Fiber Bragg Grating

Bowei Zhang

A Thesis

in

The Department

of

Electrical and Computer Engineering

Presented in Partial Fulfilment of the Requirements

for the Degree of Doctor of Philosophy at

Concordia University

Montreal, Quebec, Canada

October, 2007

Your file Votre référence
ISBN: 978-0-494-37761-1
Our file Notre référence
ISBN: 978-0-494-37761-1

Abstract

Optical High Temperature Sensor Based on Fiber Bragg Grating

Bowei Zhang, Ph.D.
Concordia University, 2007

The aim of this thesis is to fabricate a fiber Bragg grating (FBG) temperature sensor that is capable to measure temperatures in excess of 1100 °C. For this purpose, two topics have been studied and investigated during this project. One of them is the development of a high temperature resistant molecular-water induced FBGs; and the other is to investigate the effect of microwave-irradiation on the hydrogen-loaded FBG.

The molecular-water induced FBGs are different from the other types of FBG. In these devices the refractive index is modulated by the periodic changes of molecular-water concentration within the grating. The device was developed using thermal annealing technology based on hydrogen-load FBG. Thermal stability of these devices was studied by measuring the grating reflectivity from room temperature to 1000°C. The stability of the device was tested by examining the FBG reflectivity for a period of time at certain temperatures. The results show that these devices are extremely stable at temperatures in excess of 1000 °C.

The hydroxyl concentration in the grating has been also investigated during this thesis. Based on the knowledge of hydroxyl groups inside FBG, a microwave treatment was designed to increase the hydroxyl concentration in the FBG area. The results show that the molecular-water induced grating, which was fabricated using microwave radiated hydrogen-loaded FBG, are stable at temperatures above 1100 °C.

Acknowledgements

There are a number of people whom have been both directly and indirectly responsible for the successful completion of my thesis. I would like to give special thanks to my supervisor, Professor Mojtaba Kahrizi, for his guidance, encouragement and support. He not only introduced me to the experimental techniques in optics, but also showed me how to present my work more effectively and professionally. He has spent a significant amount of time supervising this work and always had time for my questions over my Ph.D. study at Concordia University.

I would also like to thank the Faculty of Electrical and Computer Engineering at Concordia University and the Natural Sciences and Engineering Research Council (NSERC) of Canada for their financial support.

A special acknowledgement must also be made to the faculty members of Electrical and Computer engineering who have ever taught me during my Ph.D. study. I would also like to express my thanks to Mr. Shailesh Prasad at the Microelectronics Fabrication Lab for his help during the course of this thesis.

I would also like to thank all the people that I have had the honor to collaborate with over my Ph.D. study.

Finally, I would like to express my gratitude to all my friends and family for their tireless love and support over the years, most notably: to my dearest wife, Ning, and to my son, Oliver, who have been supporting me during these years, allowing me to stay in the lab until late nights and during weekends, listening to my problems, encouraging me, and understand me. Their supports provide me a solid foundation for both mind and heart so that I can have the freedom and opportunity to chase my dreams.

Many thanks to all of you!

Bowei Zhang

Table of Contents

List of Figures

List of Tables

Chapter 1 Introduction

1.1 Goal of the project

This thesis is focused on the development of an innovative high temperature fiber optical sensor by fabricating high temperature resistance Bragg gratings using hydrogen loaded FBG. Moreover, the performance of the high temperature resistance FBG temperature sensors should be capable of measuring temperatures higher than 1100 °C (2000 °F) with acceptable reflectivity. These unique high temperature resistance FBG sensors can precisely monitor the temperature inside a boiler. Since the thermal stability of conventional FBG is limited by the low bonding energy of germanium-oxygen and silicon-oxygen, it is impossible to develop traditional FBG based distributed temperature sensors for high temperature application. To solve this problem, a novel FBG fabrication method – molecular-water induce high temperature resistance FBG, is suggested to investigate. During my Ph.D. thesis, the microwave irradiation effect to the hydroxyl in the FBG area is also investigated in order to increase the reflectivity of molecular-water induced FBG.

1.2 Environmental impacts using coal fired power generation

Perhaps the most serious environmental challenge we face in the coming decade and century is global warming. According to the report of NCDC (U.S. National Climatic Data Center), the global surface temperatures have increased by about 0.6°C since the late-19th century. About 0.2 °C to 0.3 °C, it happed the past 25 years as shown in Figure

1.1. The world's most respected climate scientists have concluded that our planet is warming as a result of manmade pollution. They also conclude that unless we act quickly to reverse this trend, we would be facing catastrophic changes in weather systems and our climate across the globe [1].

Some emissions of greenhouse gases occur naturally, while others result from human activities. Carbon dioxide, methane, nitrous oxide, and ozone are greenhouse gases that have both natural and human-related emission sources. Historically, energy-related activities have accounted for more than three-quarters of the global warming potential (GWP)-weighted greenhouse gas emissions [2]. Most of these are carbon dioxide emissions; however, some emissions of methane and nitrous oxide also result from stationary and mobile combustion. Almost all emissions from the energy sector result from fossil fuel combustion, which includes the burning of coal, natural gas, and petroleum. Fossil fuel combustion from stationary sources, such as electricity generation, generates more than half of energy-related emissions, while combustion of fossil fuels by mobile sources, such as automobiles, represents approximately one-third. In addition to fossil fuel combustion-related activities, carbon dioxide is also emitted as a result of natural gas flaring and biomass burning, and methane is emitted through coal mining as well as the production, processing, transmission of natural gas and petroleum.

According to a report of Environmental Protection Agency (EPA) [2], the power plants in the United States are responsible for 40 percent of all emissions of carbon dioxide (CO_2), the leading cause of global warming (Figure 1.2). Burning coal results in more CO_2 emissions than any other method of generating electricity, yet people continues to rely on coal for more than half of our electricity generation.

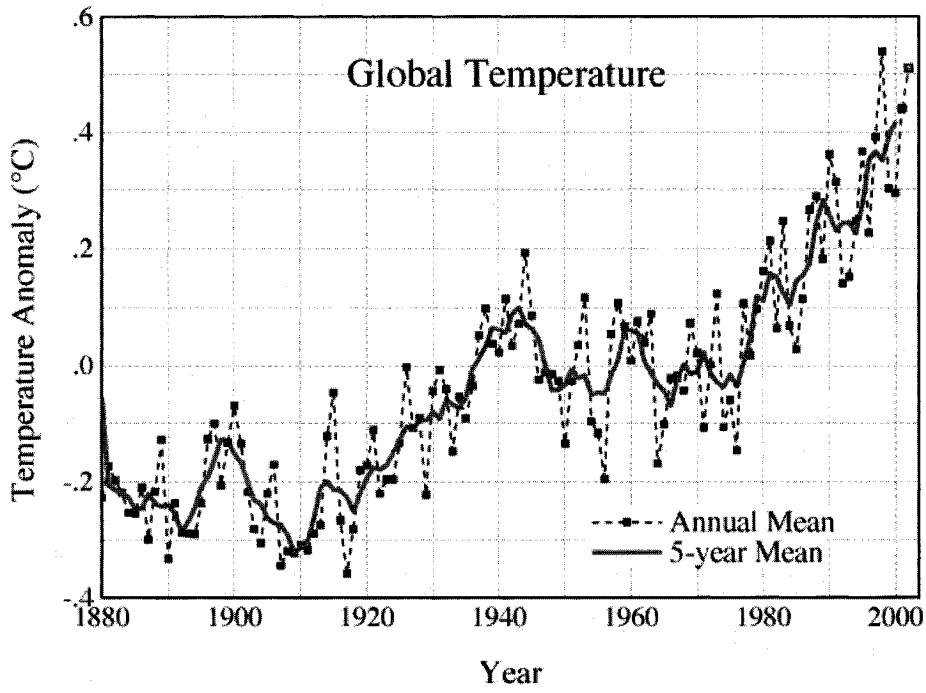

Figure 1.1 *Graph shows annual mean global temperature anomalies over the period 1880-2001. The zero line represents the long term mean temperature from 1880-2001*[1].

Besides the global warming, the fossil fuel power contributes to acid rain, and air pollution (electricity generation is responsible for 38 percent of USA carbon dioxide emissions) [3]. Acid rain is caused by the emission of nitrogen oxides and sulfur dioxide into the air. These themselves may be only mildly acidic, yet when it reacts with the atmosphere, it creates acidic compounds such as nitric acid and sulfuric acid that fall as rain, hence the term acid rain. In Europe and the USA, stricter emission laws have reduced the environmental hazards associated with this problem.

Another danger related to coal combustion is the emission of fly ash, tiny solid particles that are dangerous for public health (Natural gas plants emit virtually no fly ash).

These can be filtered out of the stack gas, although this does not happen everywhere. The most modern plants that burn coal use a different process, in which synthesis gas is made out of a reaction between coal and water. This is purified of most pollutants and then used initially to power gas turbines, and then the residual heat is used for a steam turbine. The pollution levels of such plants are drastically lower than those of "classical" coal power plants. However, all coal burning power plants emit carbon dioxide. Research has shown that increased concentration of carbon dioxide in the atmosphere is positively correlated with a rise in mean global temperature, also known as climate change.

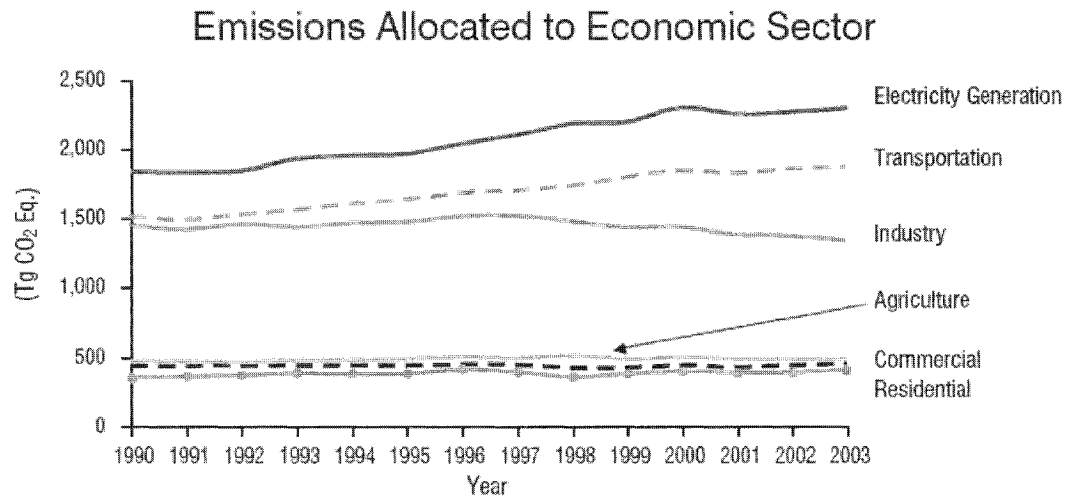

Figure 1.2 *1990-2003 green house gas emissions Trends. Total GHG emissions rose 13 percent since 1990. Dominant gas emitted was CO_2, mostly from fossil fuel combustion1 power plant* [2].

Coal also contains low levels of uranium, thorium, and other naturally-occurring radioactive isotopes whose release into the environment leads to radioactive contamination. While these substances are present as very small trace impurities, enough coal is burned that significant amounts of these substances are released. A 1,000 MW coal-burning power plant could release as much as 5.2 tons/year of uranium (containing 74 pounds of uranium-235) and 12.8 tons/year of thorium. The radioactive emission from

this coal power plant is 100 times greater than a comparable nuclear power plant with the same electrical output; including processing output, the coal power plant's radiation output is over 3 times greater [4].

Trace amounts of mercury can exist in coal and other fossil fuels.[5] When these fuels burn, mercury vapor can be released and the mercury is a neuron-toxic heavy metal which bio-accumulates in food chains and is especially harmful to aquatic ecosystems. According to the United States Department of Energy, the worldwide emission of mercury from both natural and human sources was 5,500 tons in 1995 [5] and coal-fired plants in the U.S. release an estimated 48 tons annually, which is less than 1 percent of the worldwide emissions [5]. The Environmental Working Group (a privately funded environmental advocacy organization) alleges that coal-fired power plants are the largest emitters of mercury in the USA [6].

Today's state-of-the-art enables efficiencies of over 45 % and 43 % (LHV) for bituminous coal and lignite-fired power plants respectively (corresponding to steam outlet temperatures of 600 / 620 °C [7]), compared to a 35 % average in the 1970s. In the mid 1990s manufacturers and utilities decided to make the step towards the 700 °C technology for coal-fired power plants, a step that is equivalent to a net efficiency of over 50 % (LHV) for coal-fired power plants [8]. The advantages of this development are obvious:

The increased efficiency offers a satisfactory response to the requirements for lower Cost of Electricity (CoE), reduction of all primary emissions, saving resources and reduction of CO2 emissions.

Since the energy efficiency of coal fired power plant is related to the pressure and temperature of steam ([7], 44.2%/25MPa/600 °C; 41.4%/24.1MPa/538 °C). The closer the steam temperature reaches to the critical temperature the more efficient energy conversion. However, if the steam temperature is over the critical temperature point, the heat exchange system and steam pipes will be damaged by the high pressure steam. The aim of this thesis is to develop the high temperature FBG temperature sensor array, which is capable operated at 1100 °C. This high temperature FBG sensor can be used to detect the temperature of the steam generator system and the creep corrosion of stream pipes in the steam generator system. According to the measured temperature, the control system of the coal fired power plant will automatically optimize operation parameter for the system. In the meantime, the thermal efficiency of the steam generator will also be increased; the green house gas emission will be reduced as well.

1.3 Coal fired power generation

Coal has played a major role in electrical production since the first power plants that were built in the United States in the1880's. The earliest power plants used hand fed wood or coal to heat a boiler and produce steam. This steam was used in reciprocating steam engines which turned generators to produce electricity. In 1884, the more efficient high speed steam turbine was developed by British engineer Charles A. Parsons which replaced the use of steam engines to generate electricity. In the 1920s, the pulverized coal firing was developed. This process brought advantages that included a higher combustion temperature, improved thermal efficiency and a lower requirement for excess air for combustion. In the 1940s, the cyclone furnace was developed. This new

technology allowed the combustion of poorer grade of coal with less ash production and greater overall efficiency.

Presently, coal fired power plant is still based on the same methods started over 100 years ago, but improvements in all areas have brought coal power to be the inexpensive power source used so widely today and shows in Figure 1.3 [9].

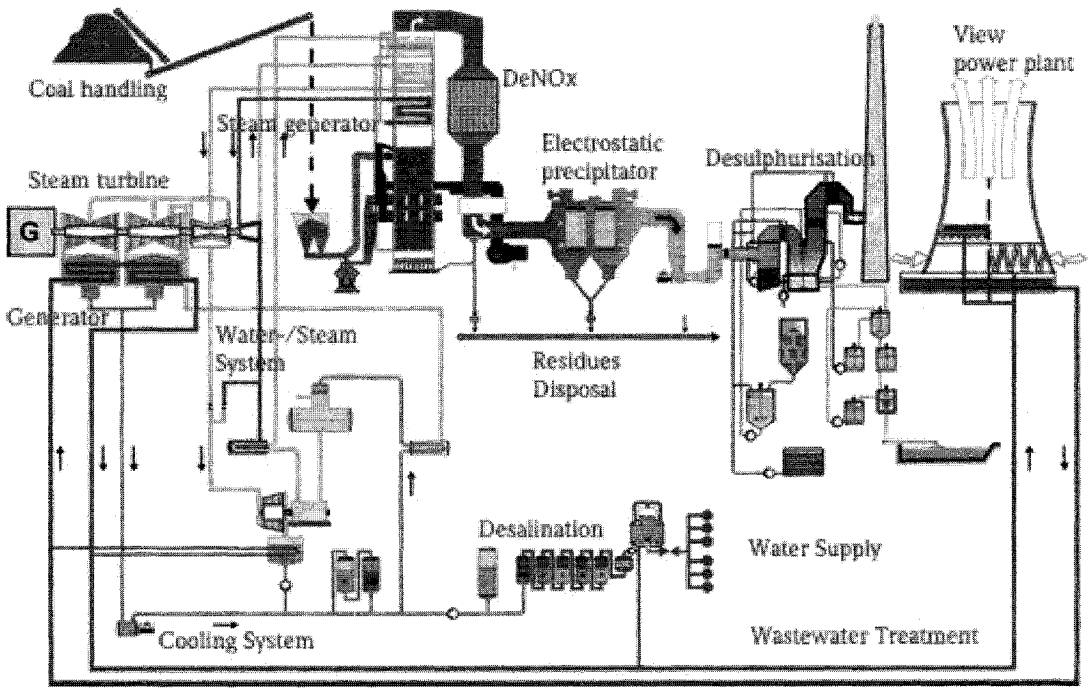

Figure 1.3 *Schematic design of coal fired power plant [9].*

The coal is transported from the storage to the coal grinding mills by way of transport systems where it is ground to finest coal dust. By way of hot air, the dust is blown into the combustion chamber of the steam generator. In the piping system of the steam generator, the water is converted to steam at high pressures. The steam drives the turbine which in turn powers the connected generator. The steam is, after it has expended

its energy in the turbine, liquefied in the condenser at ambient temperature. This water is returned to the steam generator over the heater and the supply pumps. The cooling water circuit is used to transmit the heat from the condenser to the atmosphere. The required cooling water is usually extracted from a river to be discharged to the river after heating up by circa 5 °C to 9 °C. If the warming capacity of the river is insufficient, then the discharged heat can be transmitted to the air in part or completely by way of a cooling tower. During the combustion of coal, harmful substance, such as CO_2, SO_2, NOx, ash, slag, and gypsum) will be brought into atmosphere and polluted environment.

The steam generator has the task to change the chemical energy which was changed to heat in the firing process, into enthalpy of a high pressure steam, making the unit a heat exchanger. At the beginning of its development it had been simply a heated container to generate saturated steam. The steam generator consists of the two main systems: "firing" and "evaporation".

In a Coal fired power plant steam generator system, temperature information is sought from the following 3 regions:

Application Area 1: Furnace zone: It is closed volume which houses air ports, fuel ports; has cylindrical turbulent coal flame extending in its centre, and through which lot of corrosive exhaust gas passes out to the chimney. The walls of enclosure are made up of hanging heat exchanger tubes which transfer heat from the flame radiation to water circulating within them. This area is also called as 'First pass' of a boiler. A temperature map of this entire volume on-line will enable monitoring combustion system performance as well as ensure optimum steam generator efficiency. Also required is the temperature

gradient map of the heat exchanger tube through its height (to get an idea about thermal stress it undergoes). Typical temperature is lower than 1100 °C.

Application Area 2: Exhaust Gas path 1: This is located downstream to furnace and is comparable to furnace in width & depth and may be half the height of the furnace. No flame is present. Lots of corrosive gas flows to exhaust across heat exchanger tube assemblies hanging from top. Heat exchanger tubes transfer heat from gas to water/steam mixture circulating inside them. Gas from here passes to exhaust chimney and the steam within the tubes gets directed to steam turbine. This area is also called 'Second pass' of steam generator system. A temperature map of this entire volume on-line will enable monitoring of heat transfer efficiency as well as tube assembly residual life. Also required is the temperature gradient map of the different heat exchanger tubes through their height across their width (to get an idea about thermal stress they undergo). Typical temperature in this area is 900 °C for flue gas and 600 °C for heat exchanger tubes.

Application Area 3: Exhaust Gas path 2: This is located downstream to 'Second pass' of boiler and lies between first pass & chimney. Usually of reduced cross section, it is a large duct through which relatively cool combustion gas flows toward exhaust chimney. On-line temperature sensor at the duct outlet enables to monitor the heat losses. The flue gas temperature range in this area is between 150 °C and 300 °C.

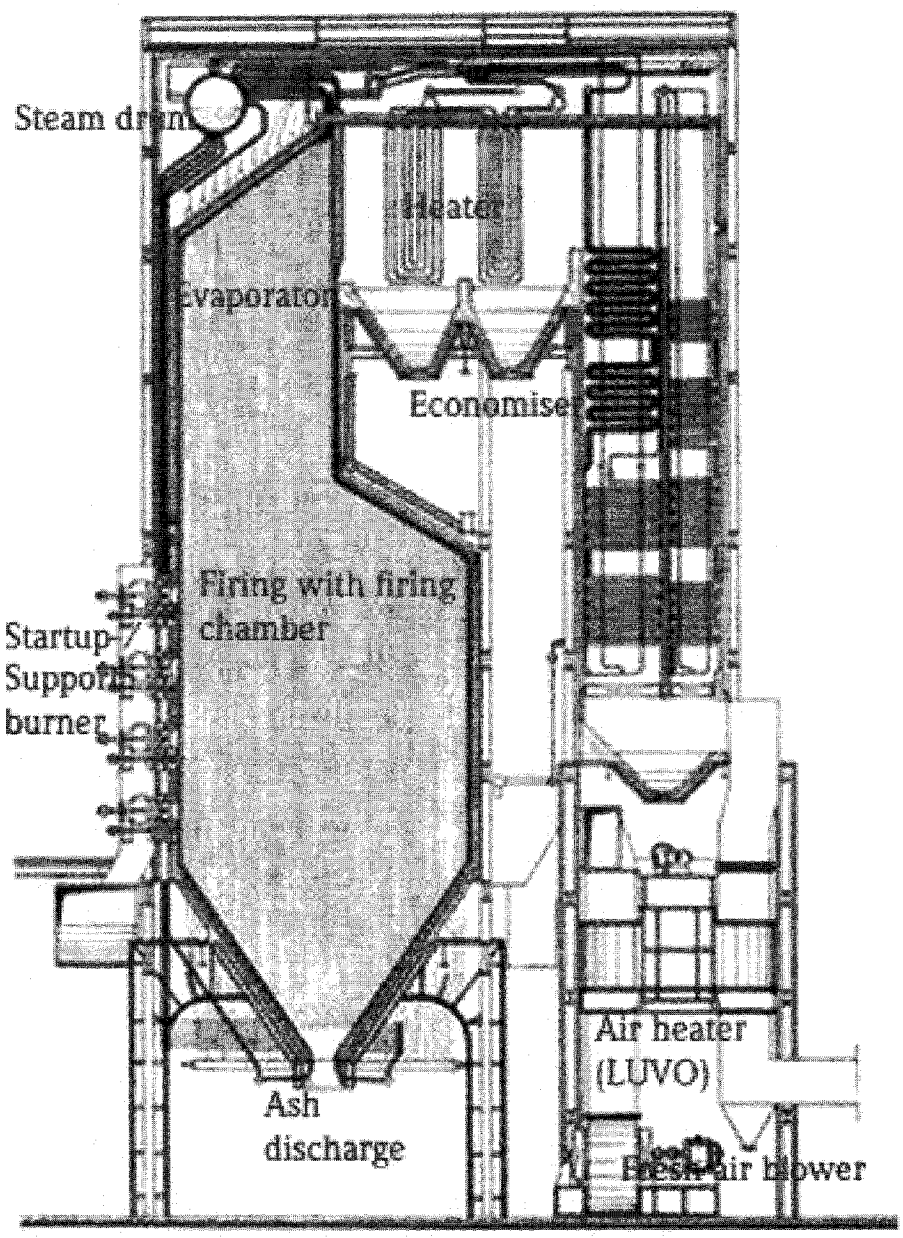

Figure 1.4 Steam Generator: Double pass-vertical tube boiler [9].

The gas emanates from the flame & traces an upward path within the first pass where it is directed to turn downward into the second pass .The gas continues to travel downward where again it is directed to turn horizontal into the gas dust toward chimney. The exit gas temperature at this duct outlet cross section shows in Fig. 1.4 [9].

1.4 Temperature monitoring system

Recently, the U.S. Department of Energy has started to reevaluate coal-fired steam generation plants and, in particular, the designs based on supercritical and ultra supercritical steam conditions. The ultimate goal of the staged development of power systems is to change steam pressure and temperature from the current values of 16.5-24 MPa (2400-3500 psig) and 540°C (1000°F), respectively, to 34.5 MPa (5000 psig) and 650°C (1200°F). Development of a revolutionary boiler design for U.S. markets, based on superheater/reheater temperatures >760°C, is also proposed. The higher steam temperature is expected to lead to another 2-3% increase in efficiency over a 700°C design, thus improving fuel usage and CO_2 emissions. Figure 1.5 shows the available materials for the critical boiler components [7].

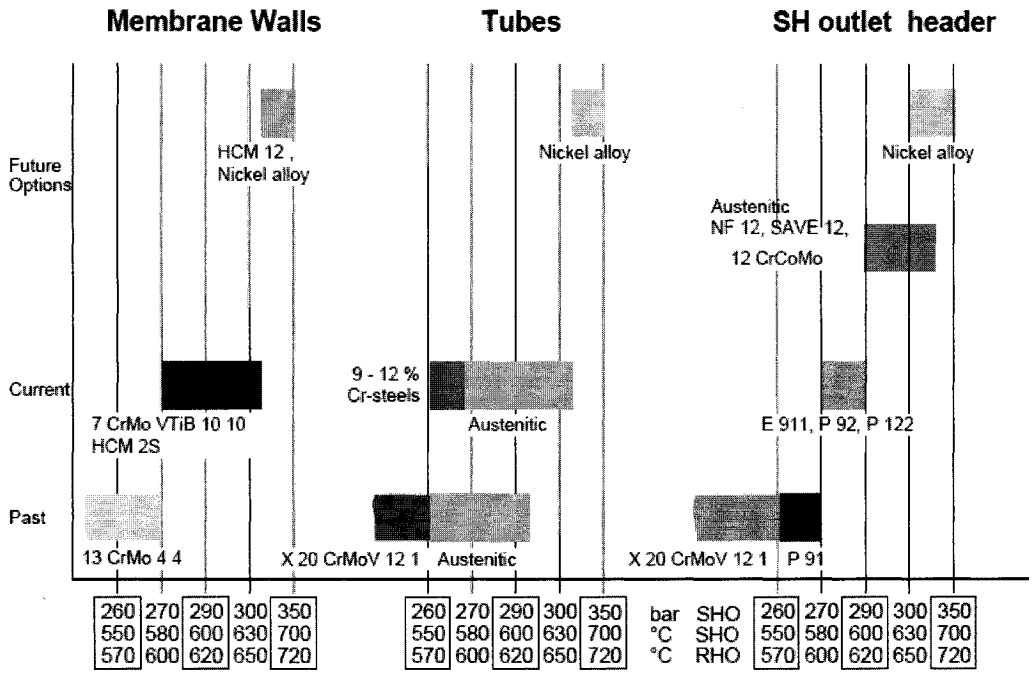

Figure 1.5 Available materials for boiler components at different steam outlet conditions [7].

To meet these new steam cycles, attention must be paid to ensure that material selection is appropriate and adapted to the new steam cycle requirements. The increase of steam conditions primarily affects the water walls, final super-heater and re-heater tubing, and the thick-walled components, mainly the high pressure outlet headers and the piping to the turbine. The super-heater coal fired power plant needs new real time temperature/structure monitoring system to control the combustion, in order to ensure the thermal efficiency; as well as to detect the corrosion/distortion (Figure 1.6 [10]) for the critical boiler components, and to extend the life time for the boiler system.

No matter what type of power plant (coal-fired, oil, or gas-based), temperature measurement remains high on the list for operational excellence throughout the coal fired power plant. Implementation of some of the new technologies results in improved safety and lower installation and maintenance costs. Incorrect measurement information due to temperature effects, non-linearity, or stability can result in damage to major equipment. In the U.S. over half of the temperature applications, and most often in power plants, involve the direct wiring of a temperature sensor to the controls system, such as RTD and thermocouple.

An RTD will provide higher accuracy and more stability than thermocouples. However, thermocouples are less expensive than RTDs, and they are more durable in high vibration and mechanical shock applications, and also tolerate higher temperatures than RTDs. For the volume, the thermocouple can be smaller than RTDs. Nowadays; the RTD and thermocouple temperature sensor probes are industrial standard temperature sensor, especially, in power plant. The common trait for the RTD and thermocouple

temperature sensors is that they must be wired to couple the sensor to the measurement device.

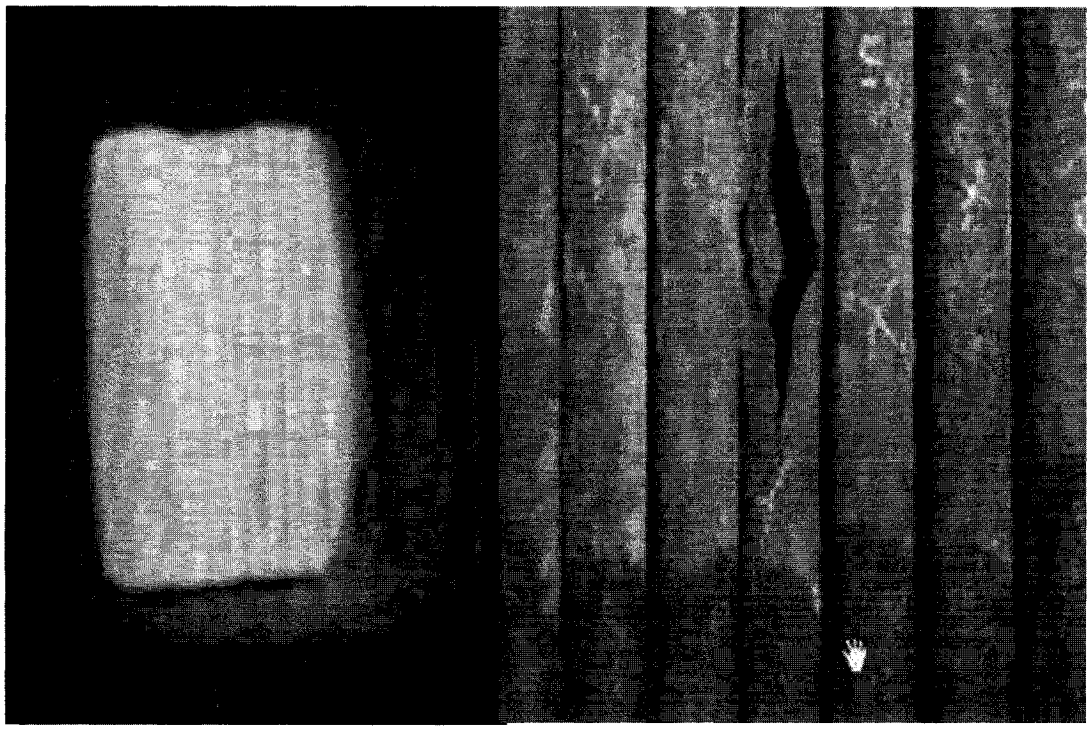

Figure 1.6 Corrosion Tube failure is the leading cause of boiler shutdowns [10].

Although both RTD and thermocouple temperature sensors are widely used in power plant temperature measurement, they have fatal problems, which are listed below:

1. Although, both devices are inexpensive and simple, it's difficult and expensive to built temperature sensor array and temperature (array) monitoring system.
2. Because of the wiring of the RTD and thermocouple temperature sensors, both devices are not immunity to the EMI.
3. Both devices have corrosion problem in the hashed environment, especially in the high temperature and high concentration alkali sulfate environment in the superheater region of coal fired power plant.

4. Both devices are difficult to install in the boiler system of coal fired power plant (Figure 1.7 [11]).

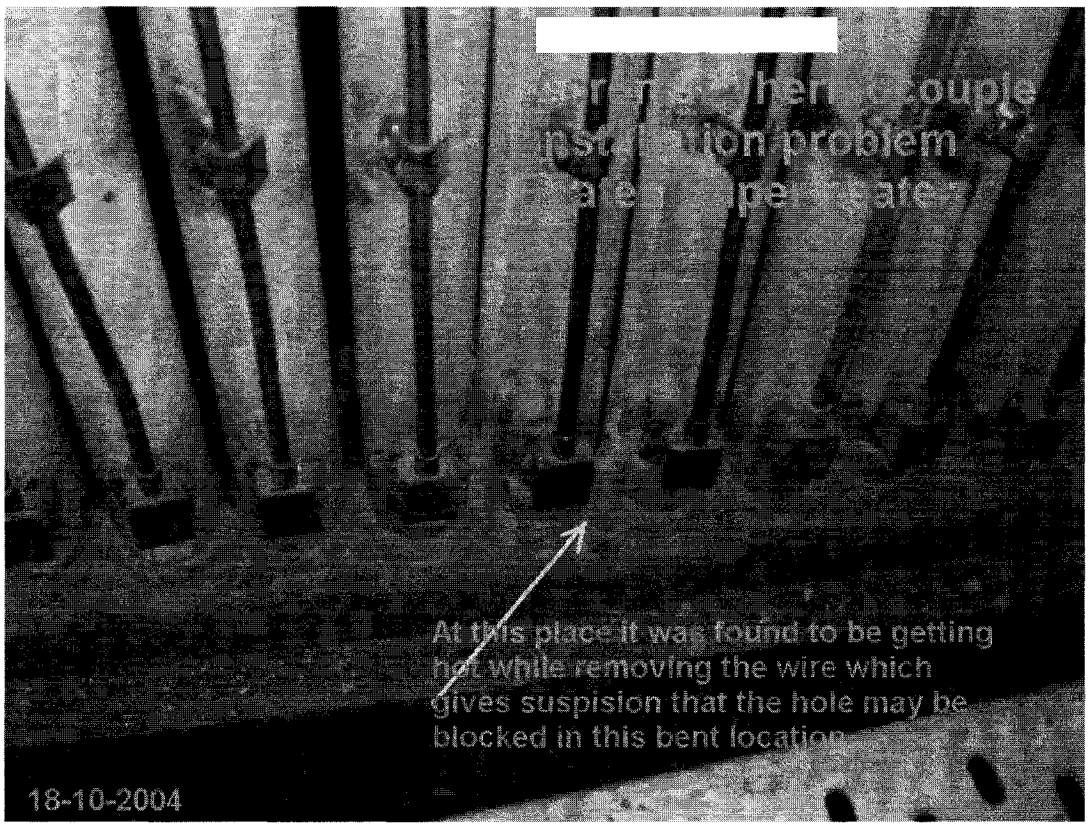

Figure 1.7 Picture shows the thermocouple sensor array and the temperature sensor installation problem in steam pipe system of coal fired power plant [11].

1.5 FBG temperature sensor

FBGs are emerging as very important elements for both of the optical fiber communications and sensing fields. Applications include wavelength routing, filtering, gain flattening, dispersion compensation in communications systems, a range of distributed strain [12], and temperature sensing systems. The inherent advantages of fiber optical sensors areas follow:

1. Lightweight, tiny, passive, low-power and immune to EMI.

2. High sensitivity.
3. Huge bandwidth and can multiple sensors to built sensor array [13].
4. Environmental ruggedness.

The concept of fiber optic sensing is based on the modulation in the sensing head, by a particular measurand, of one or more of the parameters of the light, which is guided by an optical fiber, being possible the measurand to act directly on a particular section of the fiber, in case the light never exits the fiber (intrinsic sensor), or acting on a structure illuminated by light guided by the fiber (extrinsic sensor).

The light parameters that can be modulated are intensity (energy), polarization state, phase, and wavelength. Each of these parameters gives to the correspondent class of fiber optic sensors. Conceptually, the intensity based sensors are the one that requires more accessible fiber technology (multimode technology); therefore, the intensity based sensors was the first being researched and also the first having more deeply penetrated the market. Later on, considerable work was directed to polarization and phase based fiber optic sensors essentially due to the possibility of measuring large electric currents (polarization modulation via Faraday Effect) and the possibility of measurement to a large range of parameters with very high sensitivity (phase modulation). In parallel, substantial effort was concentrated with the objective of studying the criteria for the most efficient multiplexing of these sensors.

FBGs are simple, intrinsic sensing elements, which can be "writing" in to a photosensitive fiber using the UV light and have all the advantage attributed to fiber sensors. FBGs behave like "flake mirrors" in fiber that reflect specific wavelengths due to periodic changes in the index of refraction of the fiber core. The small reflections from

these "flake mirrors" add together in a phenomenon known as the Bragg reflection, where a single large reflection results from the coherent addition of many small reflections spaced a multiple of half the wavelength apart ($m\lambda = 2L$) (See chapter 2). The wavelength, which is reflected by the FBG, can be changed in two ways, changing the ambient temperature of the fiber grating, or inducing strain in the fiber grating along the direction of the fiber.

In principle, wavelength modulation should be the most favorable sensing method owing to its absolute nature and basically unaffected by environmental noise or power loss; however, in the past several years, research on fiber sensing dodged this type of sensors, because of lacking of fiber components with appropriated performance. In recent years, FBGs proved a breakthrough being an almost ideal component for the in-fiber localized monitoring of physical parameters, of notably strain and temperature. It can be stated that a large effort of research in fiber optic sensors will be directed to the application of these devices in functional sensing structures in the future.

Fiber optic sensor technology, particularly FBGs, has enabled the implementation of this type of systems by providing sensors that are small and rugged enough that they can be integrated and consolidated directly into materials; therefore, these sensors brings with them weight reduction, minimization of points of ingress into materials, electrical isolation and immunity to electromagnetic interference. In addition, the devices have an inherent self referencing capability and easily multiplexed in a serials fashion along single fiber. Grating based sensors appear to be useful for a variety of applications. In particular the area of distributed embedded sensing in materials for creating "smart structures" is of primary interest. Fibers with sensor arrays can be embedded into the

materials to allow measurement of parameters such as load, strain, temperature, and vibration.

For the FBG based temperature sensor, a variation in temperature causes a modification of the grating period and an induced modification of the refractive index of the material. The variations in the period and refractive index of the grating cause a shift in its reflected peak wavelength. And by measuring this shift, the applied temperature can be measured. The change of the temperature induces variations in the wavelength of the grating, which can be observed in either optical spectrum analyzers (OSA) or wavelength interrogators. The over change is ~6.8pm/°C near the Bragg wavelength of 830 nm, ~10pm/°C near 1300 nm, and ~13pm/°C near 1550nm although the values depend on FBG types [14]. The Bragg wavelength with temperature has been widely used for temperature sensing or temperature compensation over a lower temperature range [15] because Type I grating is erased within seconds when exposed to temperature of the order of 500 °C [16]. The accuracy of these temperature sensors depend on the wavelength detector. As an example [17], Figure 1.8 shows FBG based temperature sensors into the stator bars of a two pole air cooled turbo generator.

Using FBGs as sensor heads has a series of advantages that make it very attractive for smart structures over the other conventional fiber optic and electrical sensors. Firstly, the Bragg wavelength shifting is a linear function of the measurands over large ranges. Secondly, the measurand information is encoded as the wavelength change; hence, the sensor signal are basically unaffected by environmental noise or power loss. Thirdly, FBGs are absolutely light in weight. Due to their small diameters, they can be inserted into composite materials without disturbance. Finally, various types of sensor

multiplexing such as Time Division Multiplexing (T.D.M.), Wavelength Division Multiplexing (W.D.M.), Spatial Division Multiplexing (S.D.M.), and code division multiple accesses (CDMA) etc., as well as their combinations, can be implemented to form quasi-distributed or quasi-point sensor array systems.

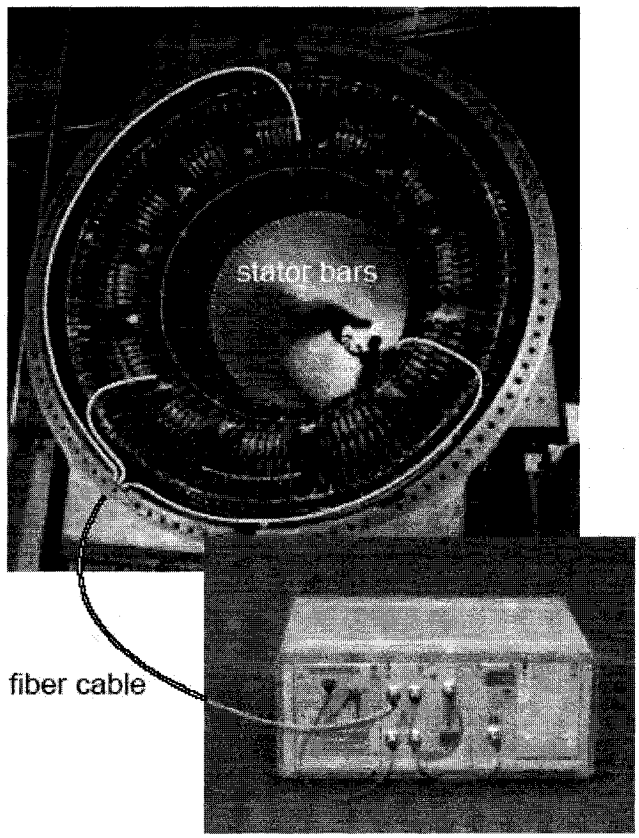

Figure 1.8 *Fiber Bragg grating based temperature sensor system built into the stator bars of a two pole air cooled turbo generator* [17].

Bragg gratings are refractive index structures manufactured by exposing the core of an optical fiber to intense periodic ultraviolet radiation. The ability of change the refractive index with radiation is referred to as photosensitivity (See chapter 2). Although photosensitivity in optical fiber has been extensively studied over several decades, no unified theory for the physical and chemical mechanisms responsible for the changes in

refractive index has been provided. One explanation of the lack of a unified theory is that the photosensitive response may differ significantly depending on several factors such as the type of fiber, prior treatment of the fiber, UV writing wavelength, and the UV laser writing power.

In most cases, the ideal situation would be to inscribe gratings into the low-loss standard telecommunications fiber that are used in optical networks today. This would enable 100 % fiber compatibility and the use of low-cost mass-produced fibers; however, standard telecommunications fibers used today have a very low photosensitivity. Solutions to this problem have been designed special photosensitive fibers and/or methods to make non-photosensitive fibers more sensitive to UV radiation. Recently, the most used technique is the standard telecommunication fiber (SMF-28 silica fiber with 3% GeO_2) loaded with hydrogen. This loaded fiber is called hydrogen loaded fiber. Because it has extremely high photosensitive for the 248 nm wavelength, nearly all the commercial FBGs are produced using the hydrogen-loaded fiber.

This technique that Bragg gratings are made by hydrogen loaded fiber has fatal limitation. It was found that when increasing the ambient temperature the grating reflectivity started to decay and did not completely stabilize even for long treatment times. Additional increased temperature result in an even larger decrease in reflectivity. Although the gratings appeared to be stable at room temperature, this behavior placed significant limitations on deployment, considering the required lifetime of some components in the telecommunications industry exceed several decades. The problems facing sensor applications are even more stringent, as the temperature sensor may be used

in harsh environment comparing with the typical –40 to +80 °C temperature requirements for telecommunications.

1.6 Thesis layout

Chapter 1 Fiber Bragg grating sensors, especially the applications of high temperature resistance FBG temperature sensors was introduced in this prologue.

Chapter 2 This chapter is divided into two parts. In section 2.1 to 2.5, It will present a general understanding of different areas in the field of FBG, such as FBGs and photosensitivity of FBG. This part deals with definitions of Bragg gratings, their applications, fabrication technique and a short summary of the color center mode theory of the mechanisms responsible for the change in refractive index.

The second part of this chapter, section 2.6 to 2.7 deals with an overview of photosensitivity of hydrogen loaded fiber Bragg grating – as nowadays, most of FBG are hydrogen loaded FBGs due to the high photosensitivity of hydrogen-loaded fiber under the 240 nm UV laser. In these sections, the hydroxyls were introduced.

Chapter 3 This chapter discusses an overview of the problems related to the sensor, the reduction of FBG reflectivity and the shifting of Bragg wavelength in a high temperature environment.

Chapter 4 The goal of this chapter is to present the development of high temperature resistance FBG.

Chapter 5 This chapter presents the microwave irradiation effect for the hydrogen-loaded FBG and its application in the development of high temperature resistance FBG.

Chapter 6 This chapter is a summary of contributions to the field. Some suggestions for the future works are given.

Chapter 2 Fiber Bragg gratings

FBGs are refractive index structures manufactured by exposing the core of a germanium doped silica fiber to intense periodic ultraviolet radiation. The ability to a permanent change in the refractive index of the fiber core with radiation is referred to as photosensitivity.

The standard single-mode telecommunication fibers, doped with 3% germanium, typically display index change to ~$3x10^{-5}$. In general, increasing the doping level or subjecting the fiber or preform to reduce conditions at high temperature can result in large index change to ~$5x10^{-4}$. This index modulation is more often desirable; however, the photo-induced devices in standard optical fibers are fabricated for compatibility with existent systems. Sensitization techniques have been developed for writing high reflectivity gratings in these fibers. An increased photo-induced index modulation to values of the order of 10^{-3} or higher have been realized via low temperature hydrogen loading (hydrogenation). Recently, the hydrogen loaded standard communication fiber is the most used fiber for FBG production.

This chapter is an introduction of FBG and the hydrogen-loaded FBG. The first part (Section 1 to 5) is an introduction to FBGs and photosensitivity. And it also gives a basic understanding of different areas in the field. The second part (Section 6 and 7) is the mechanisms of the hydrogenation increased photosensitivity of the standard communication fiber and the fabrication of hydrogen-loaded FBG.

2.1. Fiber Bragg gratings

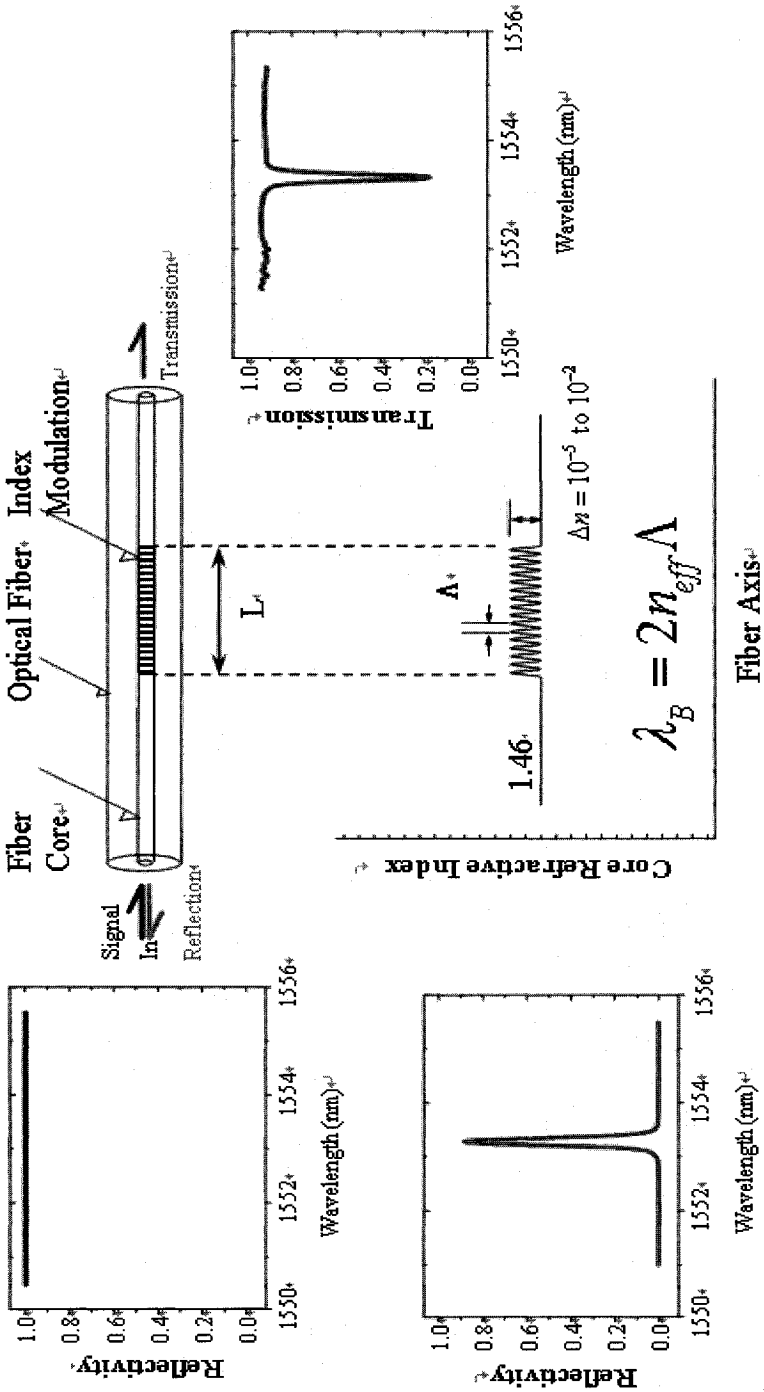

Figure 2.1 *Illustration of uniform fiber Bragg grating and its wavelength selective reflection property.*

A FBG is an optical fiber for which the refractive index in the core is forming a periodic or quasi-periodic index modulation profile. One of the most important properties of FBGs is wavelength-selective reflection. Assume that a broadband light is coupled into a fiber with FBG inside. The light whose wavelength matches the Bragg condition will be reflected back. The light whose wavelength does not match the Bragg condition will be transmitted through the fiber, as shown in Figure 2.1.

The Bragg grating condition is simply the requirement that satisfies both energy and momentum conservation. Energy conservation ($\hbar\omega_f = \hbar\omega_i$) requires that the frequency of the incident radiation and the reflected radiation is the same. Momentum conservation requires that the incident wave-vector, κ_i, plus the grating wave-vector, K, equal the wave-vector of the scatted radiation κ_f. This simply stated as

$$\kappa_i + \mathrm{K} = \kappa_f \tag{2.1}$$

Where the grating wave-vector, K, has a direction normal to the grating planes with a magnitude $2\pi/\Lambda$ (Λ is the grating spacing shown in Figure 2.1). The diffracted wave-vector is equal in magnitude, but opposite in direction, to the incident wave-vector. Hence, the momentum conservation condition becomes

$$2\left(\frac{2\pi n_{eff}}{\lambda_B}\right) = \frac{2\pi}{\Lambda} \tag{2.2}$$

Mathematically, the first order Bragg condition is give by:

$$\lambda_B = 2n_{eff}\Lambda \tag{2.3}$$

where λ_B is the Bragg wavelength, n_{eff} is the effective modal index and Λ is the perturbation period. By modulating the quasi-periodic index perturbation in amplitude and (or) phase, we may obtain different optical filter characteristics.

The simplest uniform FBG structure in optical fibers is an axial (z) and periodic change of the refractive index of the core, as shown schematically in Figure 2.2, with a refractive index modulation given by [18]:

$$n(z) = n_0 + \Delta n \cos(\frac{2\pi z}{\Lambda}) \tag{2.4}$$

where Δn is the amplitude of the induced refractive index perturbation (typical values 10^{-5}~10^{-2}); n_0 is the average refractive index; z is the distance along the fiber's longitudinal axis; and Λ is the geometrical grating period.

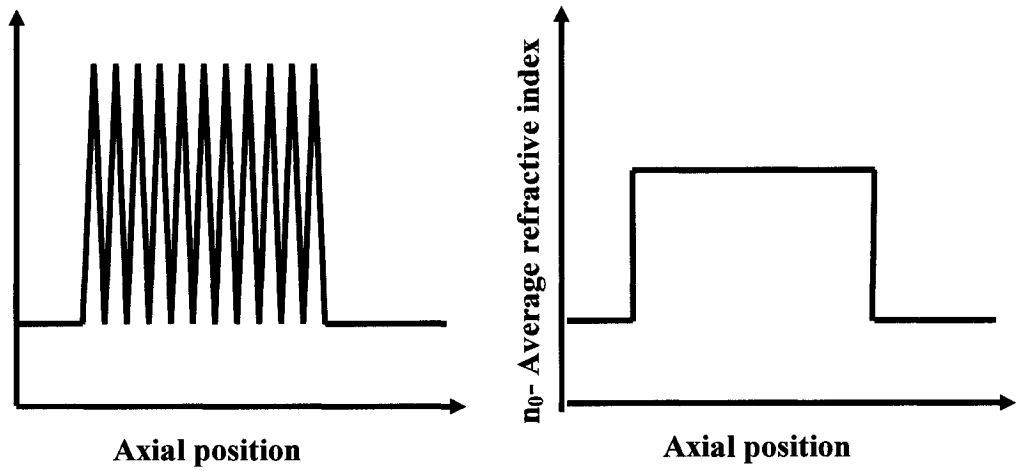

Figure 2.2 *Schematic of refractive index modulation and effective refractive index of the grating structure.*

The spectral reflectivity of the grating, solved using coupled-mode theory, is given by: [19]

$$R(L,\lambda) = \begin{cases} \dfrac{\Omega^2 \sinh^2(SL)}{\Delta\beta^2 \sinh^2(SL) + S^2 \cosh^2(SL)} & \text{for } \Omega^2 > \Delta\beta^2 \\ \dfrac{\Omega^2 \sinh^2(QL)}{\Delta\beta^2 - \Omega^2 \cosh^2(QL)} & \text{for } \Omega^2 < \Delta\beta^2 \end{cases} \tag{2.5}$$

where R(L,λ) is the reflectance as a function of wavelength λ, and FBG length L; Ω is the coupling coefficient; $\Delta\beta = \beta - \pi/\Lambda$ is the detuning wave-vector; $\beta = 2\pi n_0/\lambda$ is the

propagation constant; and $S = \sqrt{\Omega^2 - \Delta\beta^2}$, Q = iS For the single-mode sinusoidal modulated grating as described by Eq. (2.2), the coupling constant Ω is given by[3]:

$$\Omega = \frac{\pi \Delta n}{\lambda} \eta \tag{2.6}$$

where η is the fraction of the fiber mode power contained by the fiber core , which can be approximately expressed as

$$\eta = 1 - V^2 \tag{2.7}$$

where V is the normalized frequency of the fiber and it is given by $V = (2\pi a / \lambda)\sqrt{n_{co}^2 - n_{cl}^2}$, where a is the core radius and n_{co} and n_{cl} are the core and cladding refractive indices, respectively.

As an example, a calculated refraction spectrum as a function of the wavelength is shown in Figure 2.3. The following parameters are used during calculation: $NA = 0.14$, $a = 4.2$ μm , $\Delta n = 5 \times 10^{-4}$ $\Lambda = 0.532$ μm , and the grating length $L = 8$ mm . The dashed line corresponds to the strong coupling case, with $\Delta n = 5 \times 10^{-4}$. The solid line corresponds to the strong coupling case, with $\Delta n = 2 \times 10^{-4}$. The dash-dot line corresponds to the weak coupling case, with $\Delta n = 0.5 \times 10^{-4}$. From this figure, it can be seen that a higher reflectivity is achieved for the stronger coupling case.

At the Bragg grating center wavelength, the detuning factor $\Delta\beta = 0$. Thus, the peak reflectivity of the Bragg grating is [20]

$$R(L, \lambda) = \tanh^2(\Omega L) \tag{2.8}$$

From Eq. (2.8), it can be seen that the peak reflectivity increases as the refractive index modulation depth Δn and/or grating length L increases. A general expression for the

approximate full width at half maximum (FWHM) bandwidth of the grating is give by [21]

$$\Delta\lambda = \lambda_B \cdot q\sqrt{\left(\frac{\Delta n}{2n_0}\right)^2 + \left(\frac{\Lambda}{L}\right)^2} \tag{2.9}$$

where q is a parameter that approximately equals 1 for strong gratings (with near 100% reflection), whereas q ~ 0.5 for weak grating. Λ/L is the number of fringes (typically Λ/L~20 000 for a 10 mm long grating).

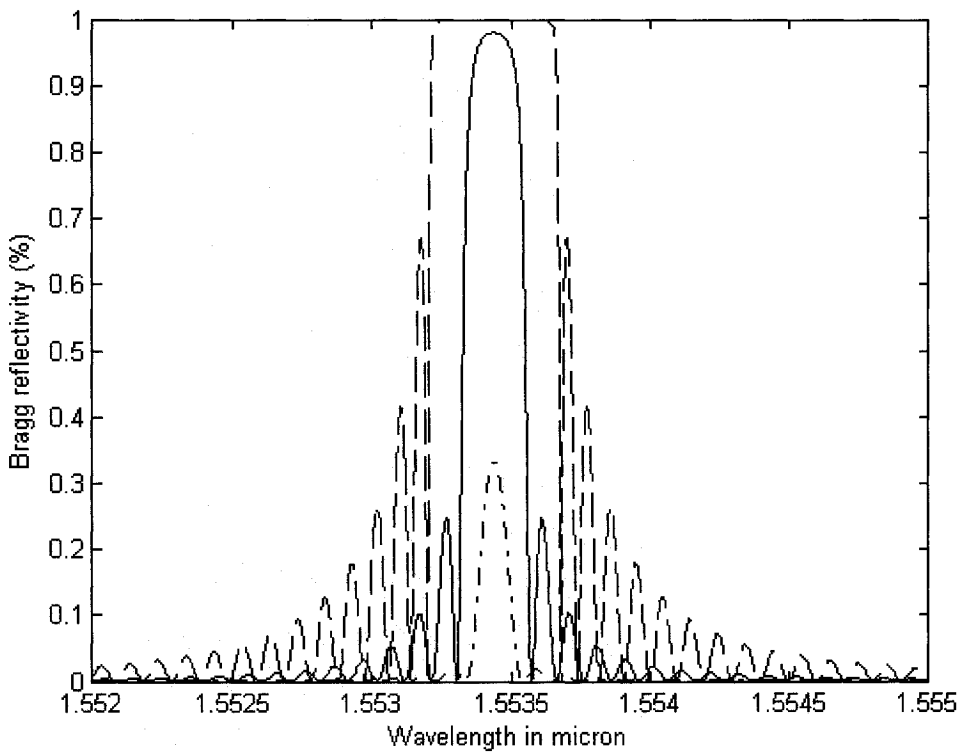

Figure 2.3 *Simulation of the reflection spectra of an 8 mm long uniform Bragg grating as a function of wavelength with different coupling constant. Dashed line:* $\Delta n = 5\times10^{-4}$ *; solid line:* $\Delta n = 2\times10^{-4}$ *; and dash-dot line:* $\Delta n = 0.5\times10^{-4}$.

2.2. History

In 1978, Hill and coworkers [22] reported the first observation of photosensitivity in optical fibers when exposing a germanium doped silica core fiber with coherent counter propagating light from an argon-ion laser at 488 nm wavelength. The result was a periodic change in the refractive index corresponding to the period of the interference pattern generated by the two beams. As the light reflected from the gratings has the same wavelength as that used to write the grating, this technique is limited to applications using wavelengths at or near the writing wavelength. Almost a decade later, in 1989, Meltz *et al.* [20] presented the transverse holographic method using a writing wavelength of 244 nm (5 eV), which made it possible to write gratings at wavelengths other than the writing wavelength. Previous studies of the growth dynamics of the grating strength, when using counter propagating waves, showed that the photosensitivity using 488 nm wavelength was a two-photon process . The writing wavelength of 244 nm used by Meltz et al. coincided with a germanium oxygen-vacancy defect band and the second harmonic of the wavelength used by Hill. Since the discovery of photosensitivity in optical fiber by Hill and the developments of the transverse holographic writing method by Meltz, thousands of articles have been published concerning photosensitivity and Bragg gratings. Today, FBGs have become almost synonymous with the field itself. Most fiber-optics sensor system makes use of Bragg grating technology [15, 16].

2.3. Classification of FBGs

Several types of FBGs have been reported. The following sections briefly describe two different classification schemes based on the coupling characteristics and the growth behavior of the grating during manufacturing [14, 15].

2.3.1. Classification by coupling characteristics

There are three different types of basic gratings depending on the coupling function. The Bragg gratings described previously are usually referred to as ***short period gratings***. The grating period is typically 0.22-0.54 μm with the light coupled into the backward propagating direction, reflection. By tilting the fringes of short period gratings, it is possible to couple light out from the core into backward propagating radiation modes. These loss gratings are usually referred to as ***slanted*** or ***tilted gratings*** [23]. Such gratings have been used for gain equalization in erbium-doped fiber amplifiers.

The third type of gratings is referred to as ***long-period gratings*** [24]. These gratings have a period that is typically 100-500 μm and the light is coupled into forward propagating cladding modes. Acting as loss filters, these gratings are typically used for gain equalization. Due to the long period of the grating, they can be successfully manufactured using point-by-point writing with either UV exposure or heat. For local heating of the fiber, a CO_2-laser or an electric-arc discharge can be used.

2.3.2. Classification by growth characteristics

There is also a classification scheme used depending on the growth behavior of the grating during inscription. This scheme is mainly used to describe short-period gratings.

Prior to the discovery of photosensitivity in fibers, ***surface relief gratings*** was used for some applications. Here a surface corrugation/modification of cladding near the core results in interacting with the evanescent field causing strong reflection. These gratings were typically manufactured through etching or polishing [25].

Type 0 gratings or *Hill gratings,* are the self-organized gratings, discovered by Hill *et al.* [22], formed by launching light in the fiber from which partial reflection at the cleaved fiber end-face creates the periodic interference pattern. As the grating is formed more light will be reflected within the fiber and hence increase the growth rate of the grating. These gratings have limited use, as the writing wavelength is also the Bragg wavelength of the grating.

Type I gratings refers to the most common gratings characterized by a monotonous growth. It is commonly observed in most photosensitive fibers under either continuous wave (CW) or pulsed UV irradiation. More specifically, this classification refers to a grating produced with $100mJ/cm^2$/pulse. It is interesting to note that the reflection spectrum of the guiding mode is complementary to the transmission signal, implying that there is negligible loss due to absorption or reflection into the cladding. This is a fundamental characteristic of a Type I Bragg grating. Furthermore, due to the photosensitivity type of the Bragg grating, the grating itself has a characteristic behavior with respect to temperature erasure. Type I gratings can be erased at relatively low temperatures (approximately 200 °C). Nevertheless, Type I gratings are the most utilized Bragg gratings and operate effectively from -40 °C to +80 °C, a temperature range that satisfactorily covers most telecommunications and sensor applications [16].

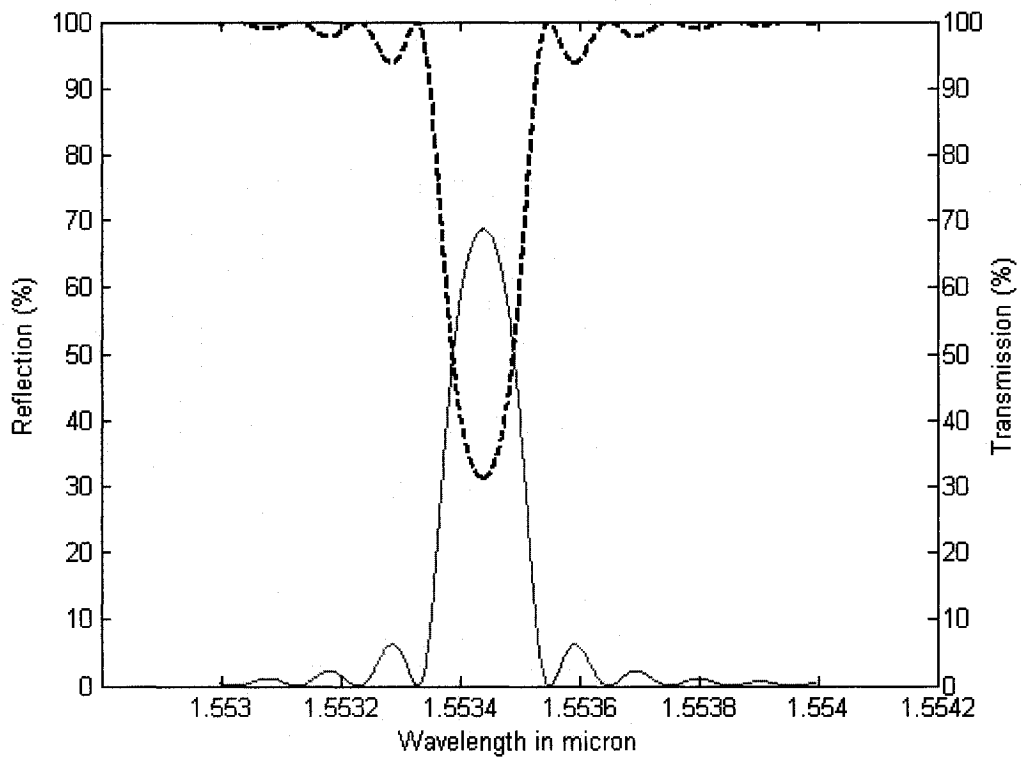

Figure 2.4 *A typical spectral response of a uniform period, Type I grating. Transmission and reflection spectral of a broadband light source in the region of the Bragg condition is satisfied.*

Type II gratings are high power single-pulse (>0.5J/cm^2) "damage" gratings characterized by large losses on the short wavelength side of the Bragg wavelength [26]. The damage is often localized at the core-cladding interface. The typical transmission and reflection spectrum of Type II grating can be described as following: The reflection appears to be broad and several features over the entire spectral profile are believed to be due to non-uniformities in the excimer beam profile that are strongly magnified by highly nonlinear response mechanism of the glass corn. Type II gratings pass wavelengths longer than Bragg wavelength, whereas shorter wavelengths are strongly coupled into the cladding, as is observed for etched or relief fiber grating, permitting their use as effective wavelength selective taps.

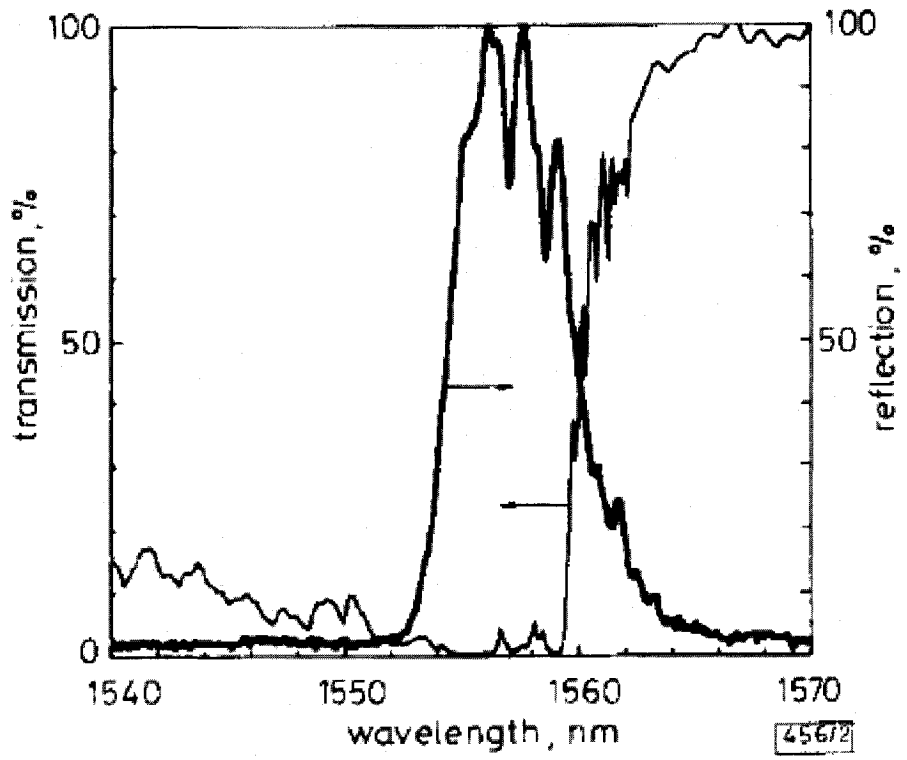

Figure 2.5 *Reflection and transmission spectra of a Type II grating. At wavelengths below the Bragg wavelength of 1556 nm the light is strongly coupled into the cladding* [26].

Results of stability tests have shown Type II gratings to be extremely stable at elevated temperature. At 800 ^{O}C over a period of 24 hours, no degradation in grating reflectivity was evident. At 1000 ^{O}C most of the gratings disappears after 4 hours, implying that the localized fusion has been thermally "washed out". This superior temperature stability can be utilized for sensing applications in hostile environments [16].

Type IIa gratings are characterized by the fact that the reflection initially grows as for type I gratings then decreases followed by a subsequent growth. Also referred to as negative index gratings, these gratings probably contain two components; one positive index grating (type I) and one negative index grating [27]. Type IIa gratings are most often observed in high GeO_2-doped fiber (>25%, high numerical aperture (NA) fibers). It

is almost certain that the mechanisms responsible for Type I and Type IIa are different. It is interesting to point out that the formation and erasure of a Type I spectrum induces a shift in Bragg wavelength toward the red part of spectrum, increase both the mean and modulated index changes. At the time of erasure, the Bragg wavelength either shifts toward the blue part of the spectrum or does not significantly shift in the course of the Type IIa grating inspection [16].

2.4. Mechanisms of photosensitivity

This section is a short summary of the color-center model to clarify different suggested mechanisms for photosensitivity. Here just give references [15], [16], and [28].

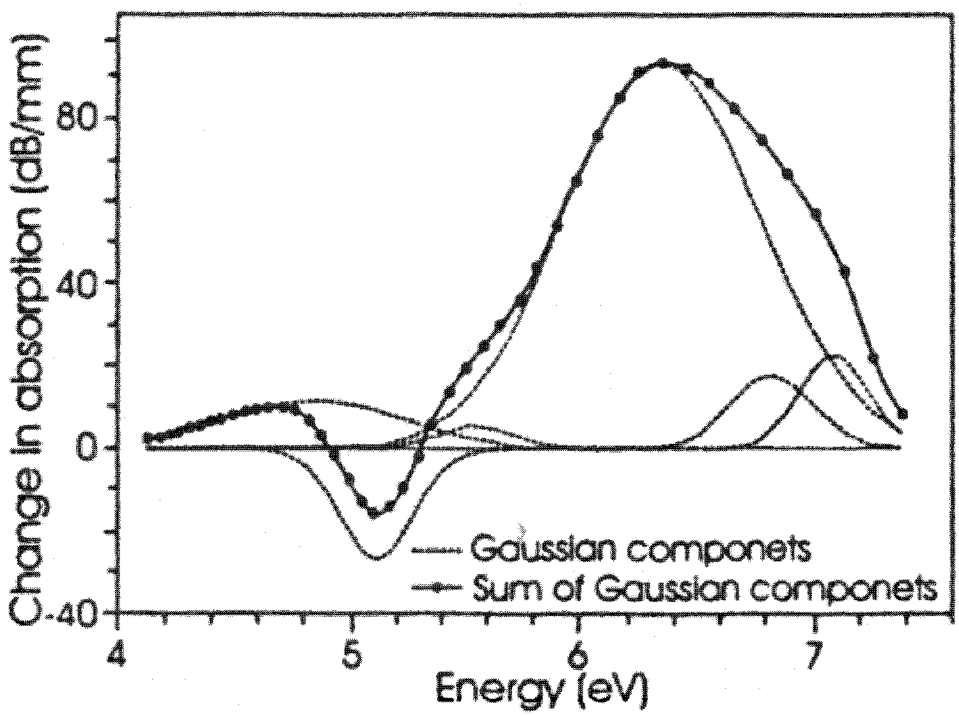

Figure 2.6 *Changes in the UV absorption spectra for 3 mol% germania MCVD fiber preform core: data point (solid circuits), six Gaussian components of fit (dashed line), and sum of Gaussian components (solid line)* [31].

Defects are important to optical fibers because their absorption bands cause deleterious transmission losses; these defects are called color-centers. Photosensitivity in germanium doped fibers was an absorption band peaking at ~240 nm [20] which was attributed to germanium-oxygen deficiency [29]. Irradiating the core, using near 240 nm wavelength, results in bleaching of the 240 nm band and growth of absorption bands located near 190 nm [30]. An example from R. M, Atkins *et al.* [31] of changes in the absorption of germanium doped silica after 248 nm UV irradiation is shown in Figure 2.6. The absorption spectrum in the UV range is as shown in Figure 2.7 [31].

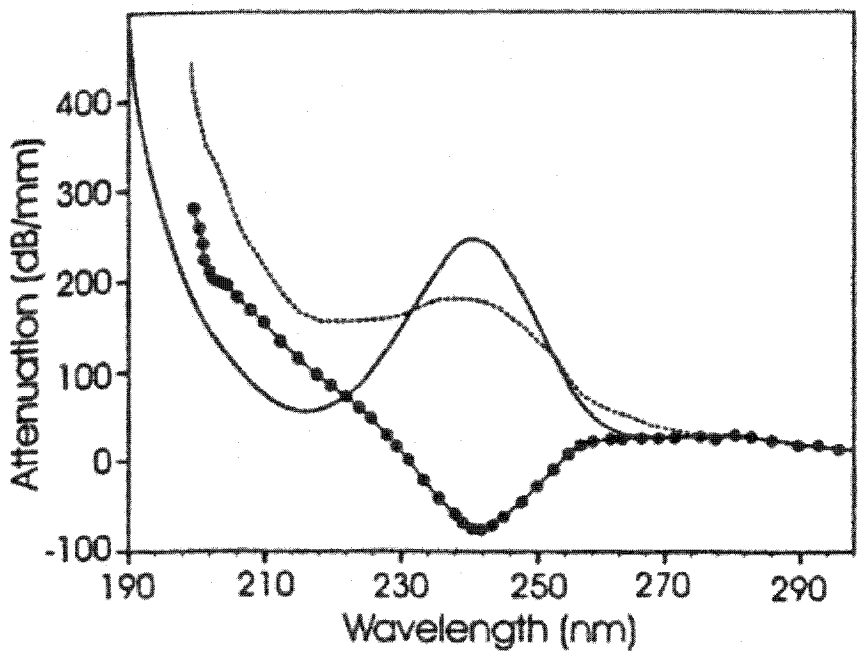

Figure 2.7 *UV absorption spectra before (solid line) and after 248 nm exposure (dashed line) writing an 81% peak reflectivity grating in AT&T Accutether single-mode fiber. The change in attenuation (solid circles) is also shown* [31].

A number of different defects [16] have been observed of which the most commonly discussed are schematically shown in Figure2.8 and Figure2.9. Correlative absorption bands for the main defects are given in Table 2.1.

TABLE 2.1: CORRELATIVE ABSORPTION BANDS FOR THE MOST COMMON DEFECTS RELATED TO PHOTOSENSITIVITY.

TABLE 2.1 ABSORPTION BANDS FOR THE DEFECTS		
Defect	Absorption peak	Reference
NBOHC	260 nm	[15]
Peroxy radical	160 nm	[16]
SiE'	215 nm	[16]
GODC	240 nm	[16]
Ge(1)	282 nm	[31]
Ge(2)	214 nm	[31]
GeE'	195 nm	[16]

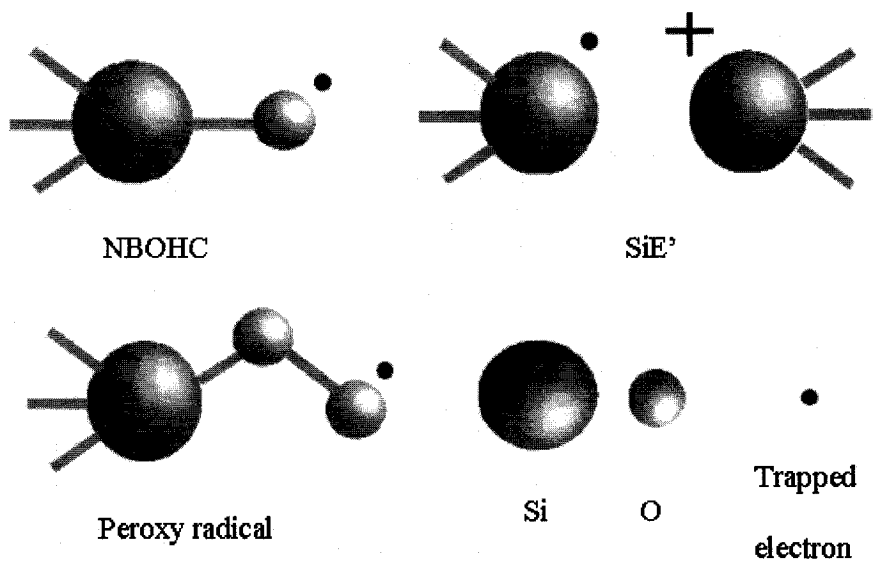

Figure 2.8 *The structure of point defects in silica (NBOHC – Non bonding oxygen hole center)* [15, 16].

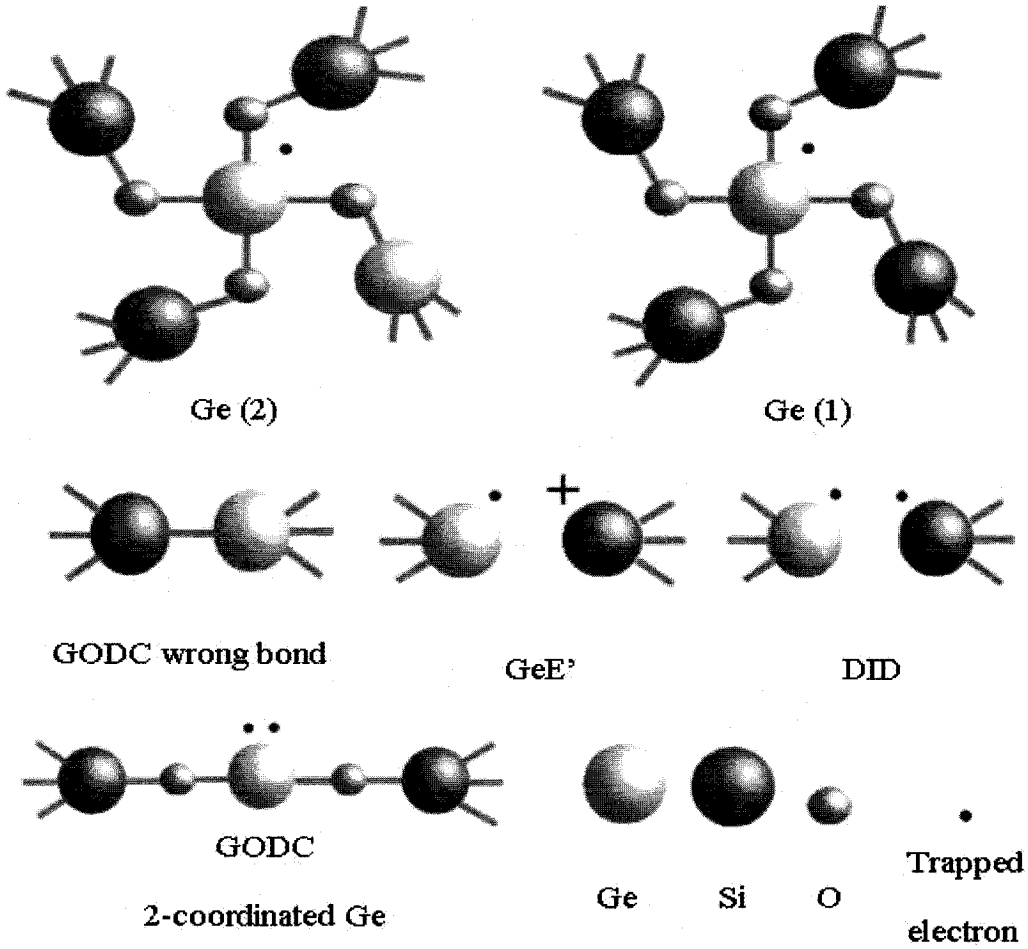

Figure 2.9 *Possible GODC (GODC – Germanium oxygen deficient center) candidates. The GeE' center and the Ge(1) and Ge(2) electron trap centers and DID (DID -- Drawing induced defect)* [15, 16].

Generally, Germanium oxygen deficient centers (GODC) are precursors [16] and GeE′, Ge(1) and Ge(2) are products of the photochemical processes although there are numerous different photochemical pathways, which have been presented to explain transformation of defects and the glass structure. The results of Atkins *et al.* [31], who measured the UV induced absorption change down to 165 nm, indicated that the main absorption changes in germanium-doped silica are due to bands at 195 nm (6.35 eV) and 242 nm (5.1 eV).

The photosensitivity of germanosilicate optical fibers has attracted considerable interest because it allows one to imprint index gratings in the fiber core. Such gratings can be written by pulse UV radiation with the excitation of a singlet–singlet (S_0 –S_1) transition band (240 nm) of a germanium–oxygen-deficient center (GODC) [32]. The mechanism of the index change has been actively debated, but this phenomenon has not been completely clarified to date. Nevertheless, the GODC photo-excitation is certainly an initial stage of this process for the Type I and Type IIa gratings. A schematic for the GODC singlet-singlet (S_0-S_1) transition band is shown in Figure 2.10 and 2.11.

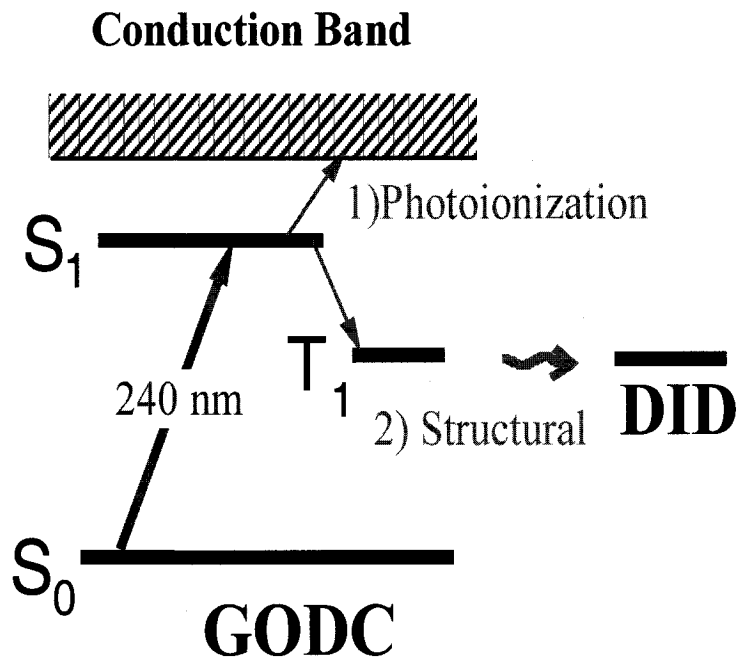

Figure 2.10 *Energy level diagram of a germanium oxygen deficient defect, showing proposed pathway with pulsed UV light at 240 nm. The excited triple state relaxes into a new defect state, a drawing-induced defect. This relaxation causes the index change that makes the Bragg gratings.*

Light at 240 nm excites a GODC from its ground single state S_0 to its excited state S_1 from which it can ionize spontaneously or by absorbing another 240 nm photo-such

ionization is thought to be necessary for an index change. However, a GODC excited to S_1 can also relax to the long-lived triplet-stat T_1. From there the defect undergoes a metamorphosis and changes its structure to a DID. It is proposed that structural rearrangement of GODC into the DID is the principal cause of light induced change of refractive index modulation.

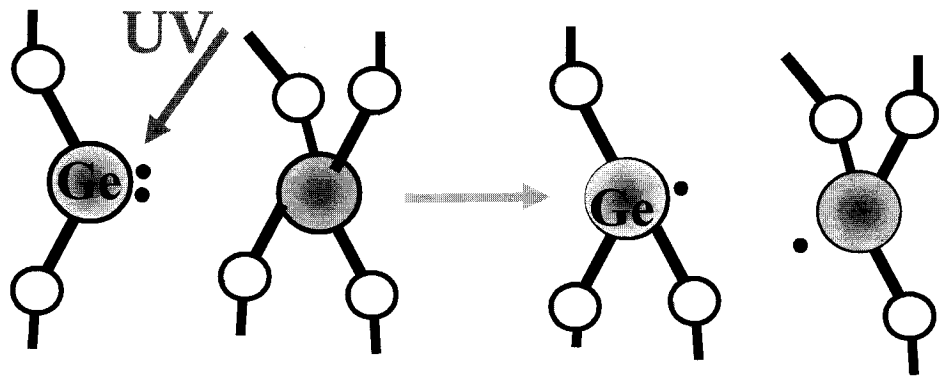

Figure 2.11 *Model of pulsed UV-induced structure change in germanosilicate optical fibers. The structural rearrangement of GODC into the DID is the principal cause of light induced refractive index change.*

2.5 FBG fabrication using phase mask

The previous section described the absorption and photosensitivity of the optical fiber. Now, we turn to the more challenging task of fabricating Bragg gratings using the phase mask technology. As discussed in section 2.3.1, the periodicity of Bragg gratings ranges from 220 – 540 nm, which places them just beyond the reach of conventional photolithography. The purpose of this section is to introduce phase mask interference lithography and the fabrication of the conventional Bragg gratings using phase mask technology briefly.

2.5.1 Phase mask interference lithography

One of the most effective methods for patterning Bragg gratings in photosensitive fiber is the phase mask technique [20]. This method employs a diffractive optical element to modulate the UV writing beam. Generally, phase masks may be formed either by holography or by electron beam lithography. One of the advantages of the electron beam lithography over the holographic technique is that complicated patterns can be written into the mask's structure such as quadratic chirps and patterns.

Phase masks are corrugated circular pieces of silica. Usually, it is a relief grating etched in a silica plate. Each phase mask has a different pitch (periodicity) to the corrugated ridges on its surface. This pitch determines what wavelength of Bragg grating will be manufactured. Figure 2.12 depicts the most common configuration for phase mask photolithography. The phase mask functions to split the incoming UV light into multiple diffracted beams. For the UV radiation at normal incident (the incident angle is equal zero), the diffracted radiation is split into $m = 0$ and ± 1 orders, as shown in Figure 2.12. The phase mask, which is used in fabrication of Bragg gratings, is carefully designed to suppress the 0^{th} diffracted order (the etched depth $d = \lambda_{uv} /(2\bullet(n_{uv} - 1))$). The $+1$ and -1 diffracted orders interfere, leading to a standing wave pattern. It is relatively easy to verify that the periodicity of the resulting standing wave is half the period of phase grating on the mask [15].

$$\Lambda_g = \frac{N\lambda_{Bragg}}{2n_{eff}} = \frac{\Lambda_{PM}}{2} \tag{2.10}$$

where N≥1 is an integer indicating the order of the grating period.

This result applies regardless of the wavelength of illumination (provided the illuminating wavelength is short enough to produce ±1 orders.) This means the phase mask lithography does not require narrowband coherent laser to produce a grating.

Furthermore, phase mask lithography systems are typically more stable than conventional interference lithography systems. In a conventional interference lithography system, the split beams traverse two relatively long paths before interfering on the fiber, whereas in a typical phase mask system the mask is usually held rigidly against the fiber. Provided the phase mask and fiber are rigidly connected, the illuminating source can be scanned over the phase mask to expose the desired area. For these reasons, phase mask lithography is the method of choice for patterning FBGs.

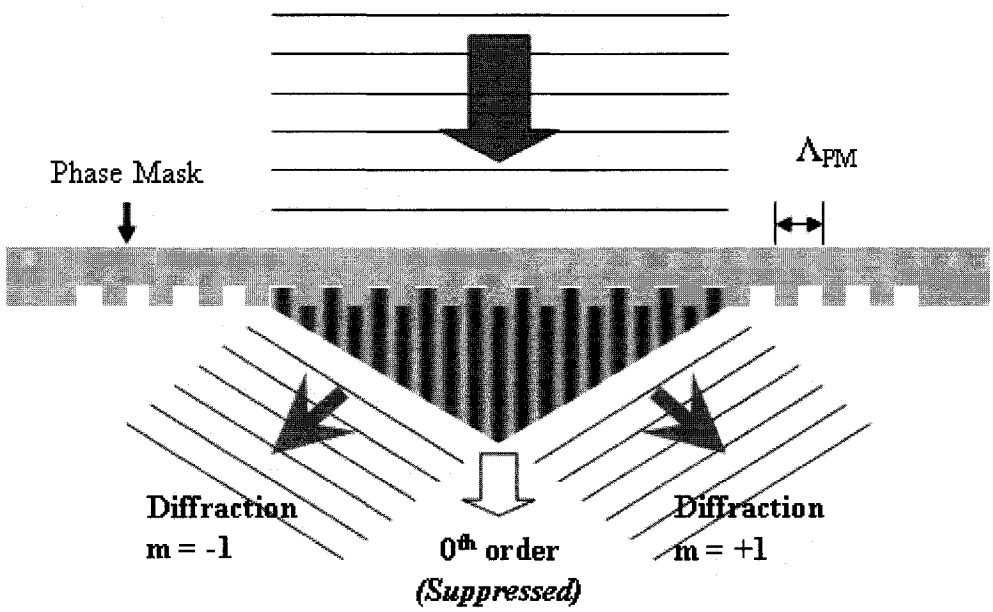

Figure 2.12 *Diagram of a phase mask interference lithography system (sometimes also called near-field holography.) Normally incident UV beam diffracted into ±1orders. The remnant radiation exits the phase mask in the zero order ($m = 0$).*

The major disadvantage of phase mask lithography is that the period of the exposed grating cannot be changed without replacing the phase mask. Another limitation is that it is difficult to completely eliminate the 0th order.

2.5.2 FBG writing system

The FBG fabricating system (in *Bragg Photonics Inc.*) is shown in Figure 2.13. The pulse power of the excimer laser (BraggStar 500 from Tuilaser AG) centered at 248 nm was adjusted to 10 mJ and the repetition rate to 50 Hz. The Plano-cylindrical lens was used to focus the fringe pattern along the fiber core. A stripped photosensitive optical fiber placed in close proximity and immediately behind the phase mask. The distance between the phase mask and the fiber is in micron level. The interference pattern photo-imprints a refractive index modulation in the core of a photosensitive optical fiber. The photosensitive fiber is connected to a broadband light source and an optical spectrum analyzer (OSA). The OSA is used to monitor the effects on the FBG writing process. The position of the slit is front of the phase mask and very close to the phase mask. The function of the slit is to control the width of the focused laser beam and also indirectly control the FWHM of the Bragg grating (See section 2.1 and Equation 2.9).

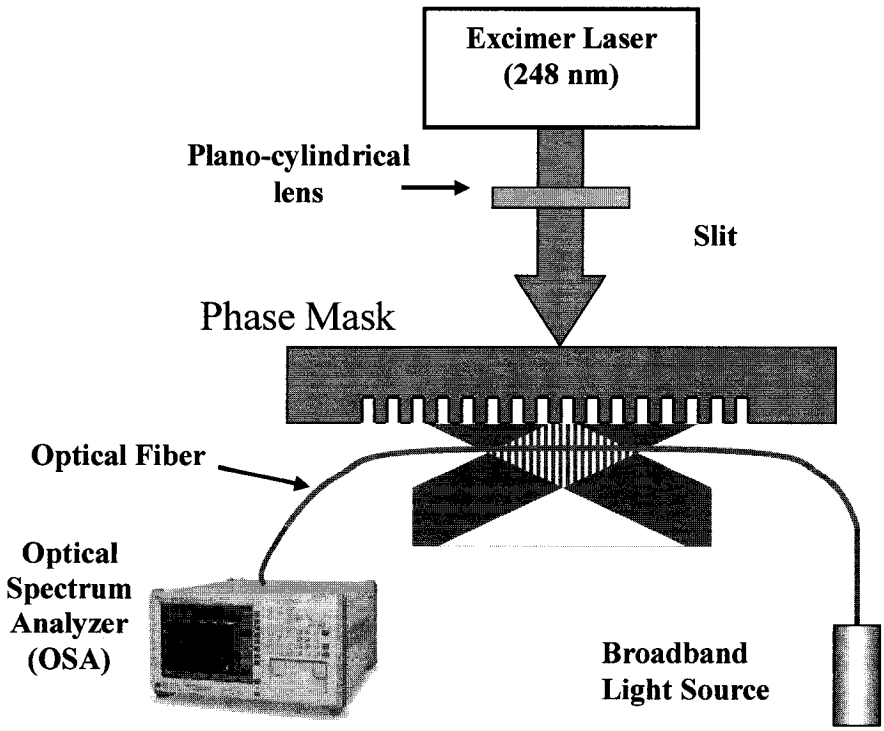

Figure 2.13 *Fiber Bragg grating writing system using an Excimer Laser.*

Alignment process: The first step is to ensure that the two first order diffracted beams are aligned properly. Use a white business card as the image plane, and adjust the rotational stage until the two diffracted beams lie along the same horizontal line. The second step is place the piece of scrap fiber into the fiber holder to check for vertical alignment and focus distance. If everything is aligned and focused, we can see an interference pattern on the white business card. Now, the station is ready to make Bragg gratings.

2.6 Mechanisms of photosensitivity in hydrogen loaded optical fiber

Since the discovery of the photosensitivity and the first demonstration of grating formation in germanium doped silica fibers, there has been considerable effort in understanding and increasing the photosensitivity of the optical fiber. Standard single

mode telecommunication fibers, doped with 3% germania (for example the SMF-28 optical fiber from CORNING), typically display index changes to reach approximately $3x10^{-5}$. The main method of increasing photosensitivity in the optical fiber can be summarized as following:

1. Hydrogen treatment [33].
2. Writing at elevated temperatures [34].
3. Mechanical treatment -- Applied strain on photosensitivity [35].
4. Material considerations, especially Co-doping silica fibers with B_2O_3 and GeO_2 [36].

TABLE 2.2: THE PHOTOSENSITIVITY EVALUATIONS OF FOUR DIFFERENT FIBERS.

Fiber Design	Fiber Δn	Saturated index modulation	Maximum reflectivity of 2mm grating	Time for reflectivity to saturate
Standard low loss fiber ~ 4 mol% germania	0.005	$3.4x10^{-5}$	12%	~ 2 h
High index fiber ~ 20 mol% germania	0.03	$2.5x10^{-4}$	45%	~ 2 h
Reduced fiber ~ 10 mol% germania	0.01	$5x10^{-4}$	78%	~ 1 h
Boron codoped fiber ~ 15 mol% germania	0.003	$7x10^{-4}$	95%	~ 10 min

The photosensitivity evaluations of the various fibers are shown in Table 2.2. It clearly demonstrates that the B-Ge co-doped fibers are the most photosensitive among the series (not include the photosensitivity of the hydrogen loaded fibers). An atypical report written by H.G. Limburger *et al.* in 1993 pointed out the index modulation as high as $1.2x10^{-3}$ [37]. To compare with Limburger's result, recently, a technique called hydrogen

treatment or hydrogenation [33] is used to increase the photosensitivity of the standard optical fiber. By using this technology, the photo-induced index modulation can arrive to 10^{-3} or higher.

Lemaire *et al.* [38] showed a simple, alternative, but highly effective approach for achieving very high UV photosensitivity in optical fibers using high-pressure hydrogen loading at room temperature (hydrogen treatment hydrogenation), before these fibers were written using UV laser. Fiber are drenched at temperature ranging from 20 °C - 75 °C and pressure from around 20 atm to more than 750 atm (the process of hydrogenation in Bragg photonics Inc. is 60 °C and pressure is less 115 atm, or 1700 psi, for 96 hours), which makes for diffusion of hydrogen molecules into the fiber core. After irradiating hydrogen-loaded fibers with pulsed 241-nm light, Lemaire and his colleague observed a large refractive-index change ($\Delta n \sim 3x10^{-3}$) and a large concentration (~ 8 mol%) of induced OH, which was roughly twice the initial concentration of hydrogen. Lemaire suggested that the index modulation was caused by a reaction of hydrogen at normal Ge sites to produce OH groups and oxygen-deficient centers. The photosensitivity evaluations of the various fibers are shown in Table 2.3. Undoubtedly, the hydrogen-loaded optical fibers (SMF-28) are the most photosensitive optical fiber among the tested series. One of the advantages of hydrogen loading is the Bragg gratings can be fabricated in any germanosilicat optical fiber and germanium free optical fibers.

In Lemaire's experiments [40], the grating, which are standard AT&T MCVD (Modified Chemical Vapour Deposition from AT&T Bell labs) single-mod optical fibre with 3-mol% germania and loaded with 3.3 % hydrogen, was formed by using UV side-writing technique using 241 nm radiation with a influence of ~300 mJ/cm^2 at 30 Hz for

10 minutes. This grating has bandwidths of 4 nm and the average core index has increased by ~3.4×10^{-3}. A comparison of the refractive index profile at midpoint of a grating with unsettled fibre is shown in Figure 2.14. Similar bandwidths and index changes were obtained using other MCVD and VAD fibres containing ~3% germania.

TABLE 2.3 THE PHOTOSENSITIVITY EVALUATIONS OF THREE DIFFERENT FIBERS.

Fiber Design	UV Wavelength (writing)	Pulse Energy (Laser)	Pulse frequency	Maximum reflectivity of grating	Time for reflectivity	Ref.
B-Ge codoped silica fiber (Fibercore Ltd.)	248 nm	12 mJ	200 Hz	saturated	< 10 min	[39]
Ge doped silica fiber (Redfern GF1)	248 nm	12 mJ	200 Hz	saturated	75 min	[39]
Hydrogen loaded fiber (SMF-28)	248 nm	10 mJ	50 Hz	100%	< 5 min	[40]

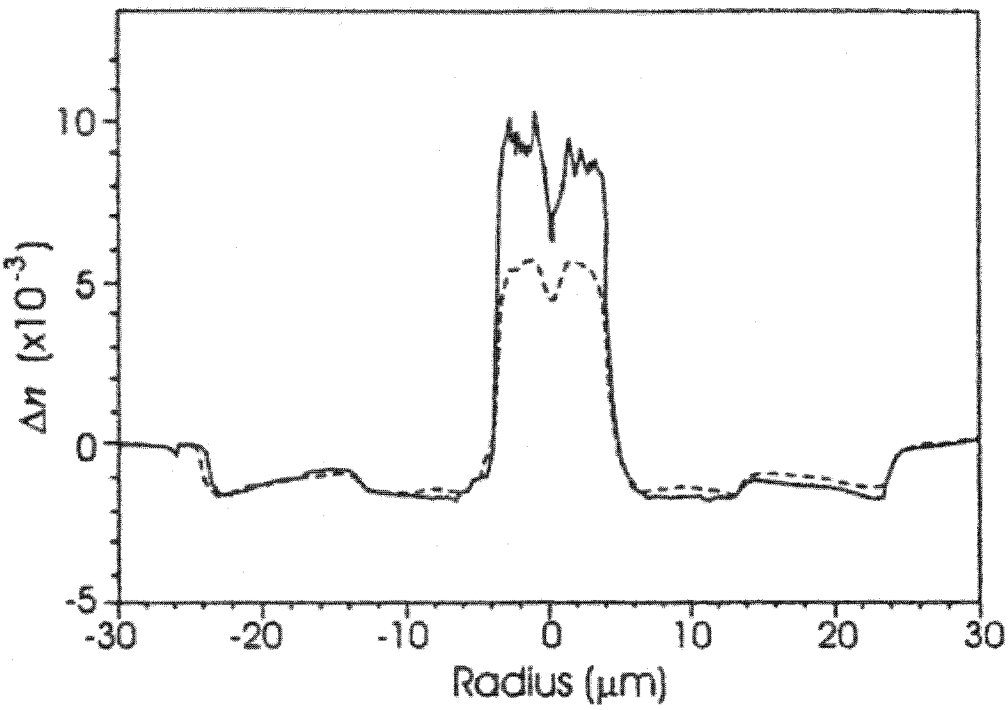

Figure 2.14 *Refractive index profiles for a standard AT&T single-mode fiber with 3% GeO_2, and for a grating which was UV written in the same fiber after loading with 3.3% hydrogen (solid curve). Δn refers to index with respect to un-doped silica. The dash curve is the refractive index profiles for a standard AT&T single-mode fiber with 3% GeO_2* [40].

The Lemaire's work has shown the UV induced loss of changes, which occur in response to write a strong grating in a 9% germanium-doped silica fibre that loaded with 4.1% hydrogen in Figure 2.15. He described in his article [38]: "The spectrum shows a strong short wavelength edge and a prominent Si-OH absorption at 1.39 μm. The concentration can be estimated to be ~8.4-mol%, quite similar to the GeO_2 content of the fiber. A similar spectrum for a 3% GeO_2 doped fiber containing 1.4% hydrogen showed ~2.9% OH and a proportionally lower wavelength edge." The OH concentration is consistently close to the germanium content of the fiber. By studying his achievement, we can summarize the results above mentioned as following: The mechanism is not

depending on the type of fiber or preform processing, but rather on the function of germanium and hydrogen concentration and the UV exposed conditions.

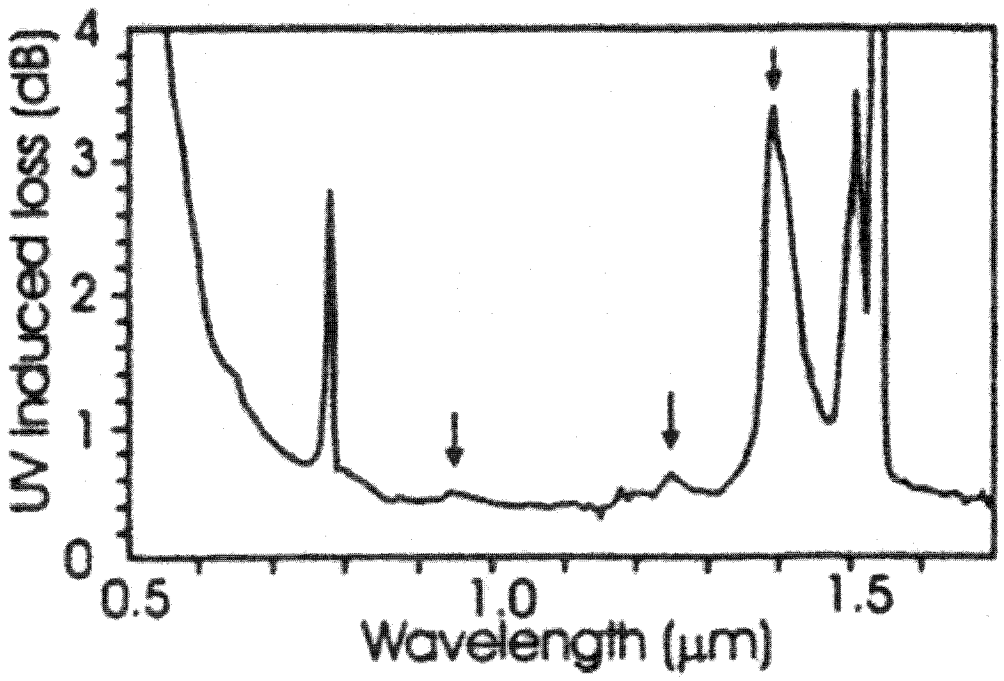

Figure 2.15 *UV induced losses in ~5mm long grating in fiber with 9% GeO_2 and 4.1% hydrogen. Features at 770 nm and 1500 nm are due to the grating. The arrow marked peaks at 0.95, 1.24, and 1.39 μm are due to OH* [38].

Figure 2.16 [41] shows the absorption spectrum changes in the IR for MCVD and VAD fibers exposed to 1 atmospheric pressure of hydrogen gas at 100 °C. During the first 2 hours exposure, the increased absorption, which is due to prominent loss peaks of molecular hydrogen, appears at 1.24, 1.70, and 1.88 μm wavelengths. The absorption increase due to molecular hydrogen is saturated after 10 hours. The absorption band, which is due to OH formation, has two very closely spaced peaks at 1.39 μm (Si-OH) and 1.41μm (Ge-OH) [41].

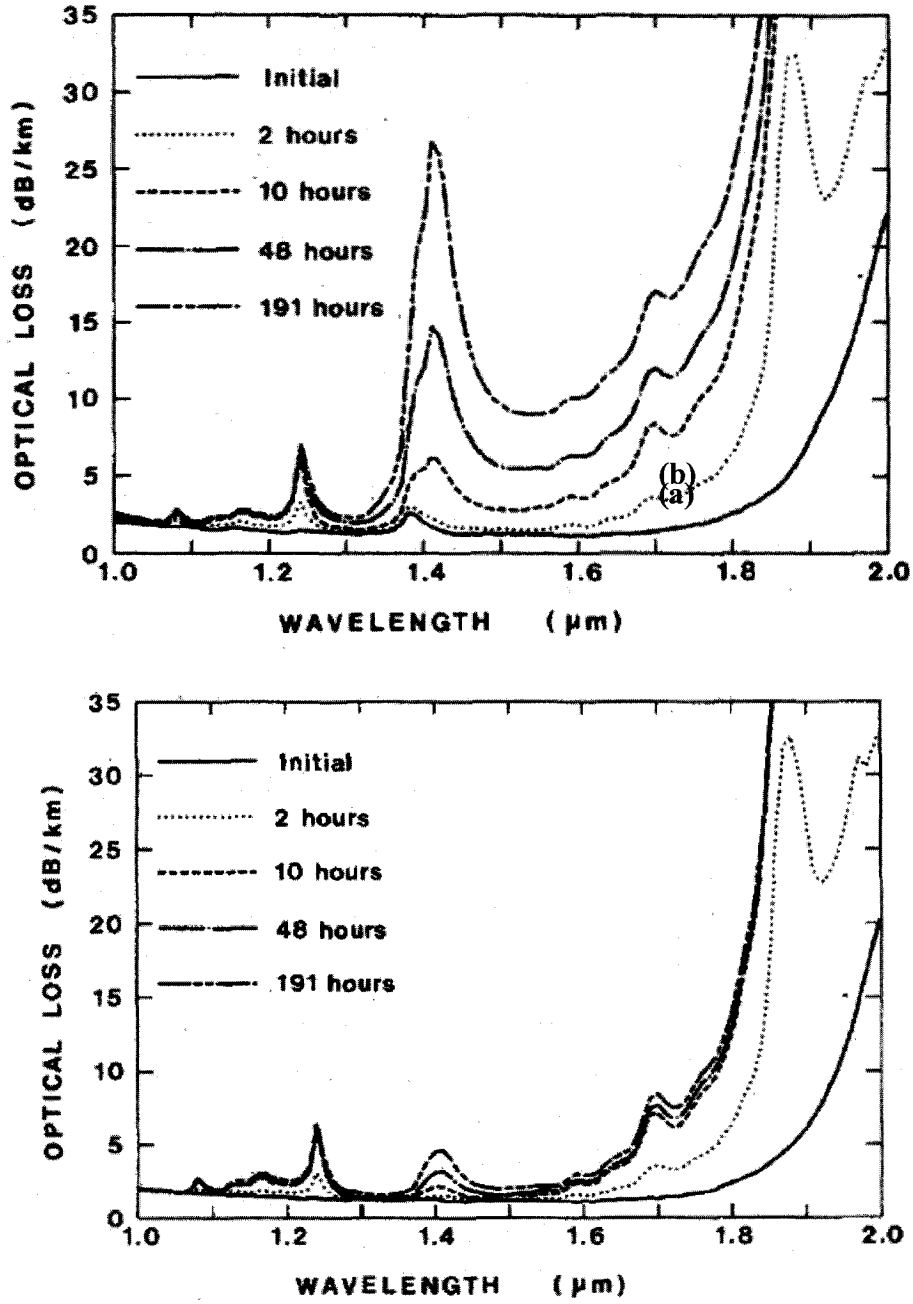

Figure 2.16 *Absorption spectrum changes in the IR for (a) MCVD and (b) VAD fibers exposed to 1 atmospheric pressure of hydrogen gas at 100 °C* [41].

The rate and saturated value of the loss-increases due to molecular hydrogen for the both MCVD and VAD fibers are very similar; therefore, the loss-increase phenomenon due to molecular hydrogen should be considered to be independent on the

fiber doping material or fabrication method. The rate for the absorption increase due to OH formation of the MCVD fiber is extremely larger than that of the VAD fiber. This fact shows that the rate of the OH-formation reaction greatly depends on the fiber doping material or fabrication method.

Optical absorption spectra of a germanosilicate (VAD) preform rods heated in hydrogen atmosphere at 500 °C at different times are shown in Figure 2.17 [42]. The increased intensity of broad absorption band peaking at 240 nm (5.14 eV) is clearly setting out in this figure. This absorption band at 240 nm was assigned to a germanium oxygen deficient center GODC (see Chapter 2.4). This phenomenon denotes that the reaction of hydrogen molecules at germanium (Ge) sites produces GODCs.

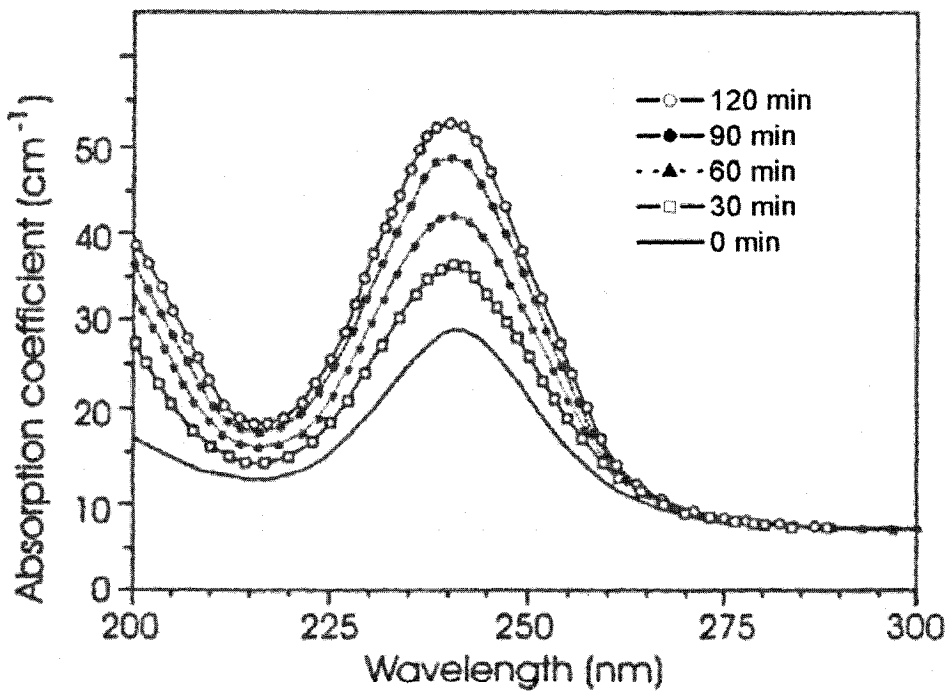

Figure 2.17 *Optical absorption spectra of a germanosilicate (VAD) perform rods heated in hydrogen atmosphere at 500 °C for different times* [42].

Figure 2.15, 2.16, and 2.17 imply that the result of the GODC's formation and OH species is reaction between hydrogen molecules and Si-O-Ge sites of germanium doped fiber. Obviously, the role of Bragg gratings in hydrogen loaded fibre includes undoubtedly both thermal and photolysis mechanisms.

$$\equiv Si-O-Ge-O-Si\equiv \; + \; H-H \; \rightarrow \; = Ge_{\bullet}^{\bullet} + 2(H-O-Si\equiv)$$

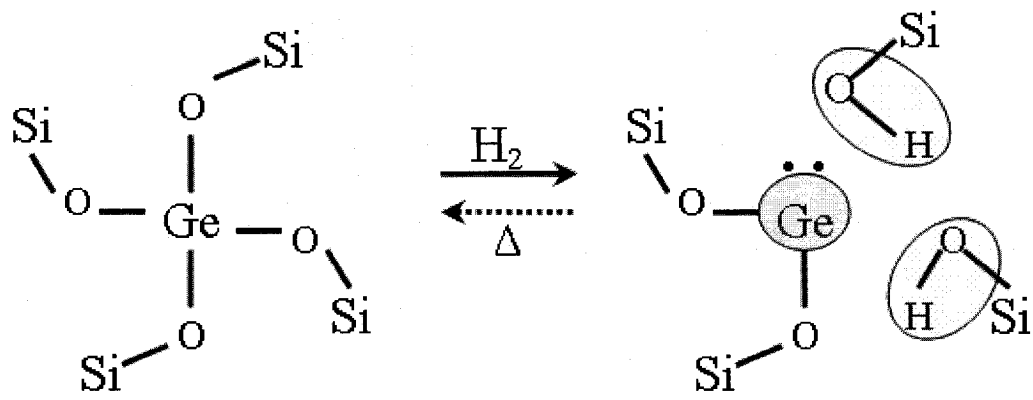

Figure 2.18 *Model of hydrogen loading introduced a large amount of GODC and Si-OH (Ge-OH) groups.*

Up to now, it has been always believed that the photosensitivity of the germanium doped fiber depends on the concentration of GODC. The mechanism of hydrogen loading is deduced as follows: The hydrogen molecules infiltrating the glass matrix by hydrogen loading will break the Si(Ge)-O-Si(Ge) bonds in the SiO_4 (GeO_4) tetrahedral network, resulting in the formation of Si-OH (Ge-OH) groups, and introduce a large amount of GODC. According to this theory, a suggested structure model of germanium doped fiber loaded with hydrogen molecule is shown in Figure 2.18. The OH group adjacent to the Ge^{2+} center lowers the dimension of the glass network and increases the degree of freedom of the structure around the Ge^{2+} center. Such a germanium atom can then moves

freely along a long distance between the equilibrium bond lengths in the ground state and arrives at the excited state.

The hydroxyl groups (OH) can be easily determined by their absorption in the infrared [43]. The fundamental absorption vibration band of OH is located at wavelength 2.7 μm and its overtone at 1.4 μm. The spectrum profile of absorption in UV exposed fibers consists of two distinct peaks associated with Ge–OH and Si–OH formation. In Figure 2.19, Si-OH and Ge–OH absorption bands for the first vibration overtone are 1.39 and 1.41 μm respectively.

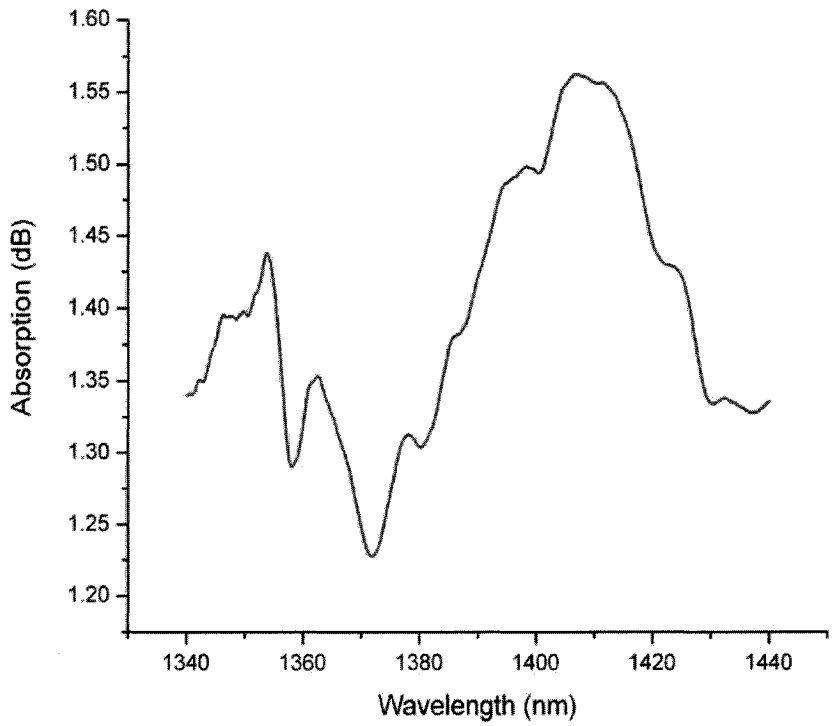

Figure 2.19 *UV induced losses in ~5mm long fiber Bragg grating with 16 dB reflectivity* [43].

The interaction of hydrogen molecules at Ge or Si tetrahedral sites inside the fiber core leads to enhanced permanent UV induced losses, particularly due to the increase in

the OH content inside the fiber. In general, the hydrogen molecules react at normal Si-O-Ge sites, resulting in the formation of Si-OH and oxygen deficient Ge defects, both of which contribute to the observed index change.

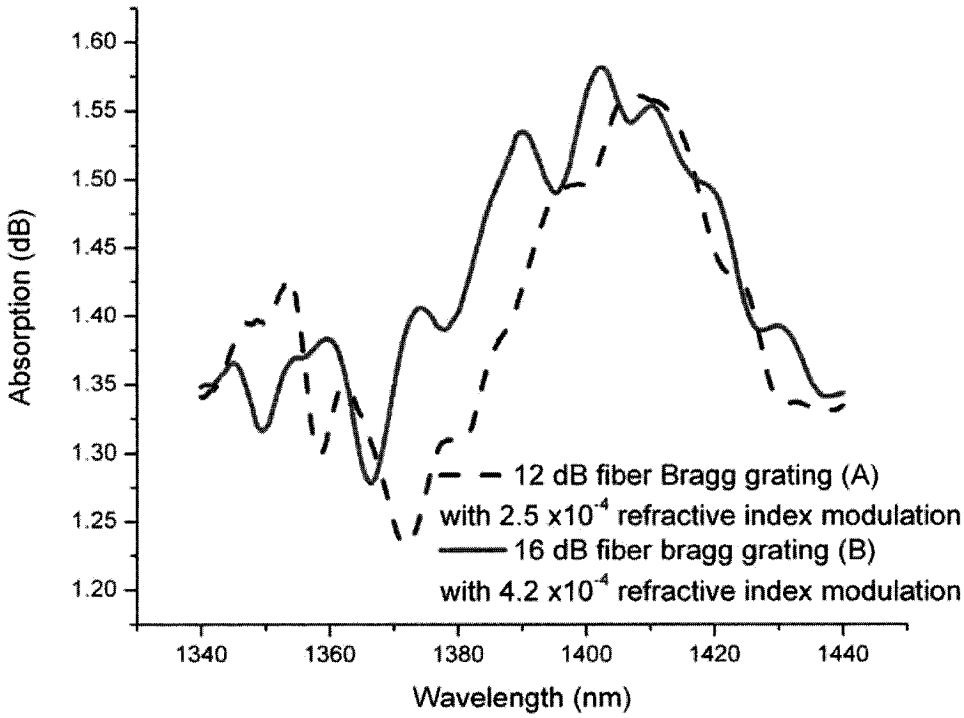

Figure 2.20 *Absorption spectra of hydrogen loaded FBG near 1.4 μm. Fiber Bragg grating A has 12 dB reflectivity at 1550 nm with 2.5x10^{-4} refractive index modulation; fiber Bragg grating B has 16.5 dB reflectivity at 1550 nm with 4.2x10^{-4} refractive index modulation* [43].

The structures of DODC and DID play important roles in the formation of hydrogen loaded FBG and the level of hydrogen loaded FBG reflectivity respectively. As we explained above, the reflectivity of hydrogen loaded FBG is depend on the amount of DID inside the fiber core. The concentration of Ge-OH and Si-OH, which are the byproducts of DID, is related to the concentration of the DID and indirect related to the reflectivity of the hydrogen loaded FBG and show in Figure 2.20. In our previous works,

two hydrogen loaded FBGs, Sample A and B, were tested for the absorption spectra (Figure 2.20) between 1.34 μm to 1.44 μm in our laboratory. The different parameters of the FBGs fabricated in different fibers are described in Table 2.4.

TABLE 2.4: PARAMETERS OF TESTED FIBER BRAGG GRATINGS IN FIGURE 2.20

Parameters	Sample A	Sample B
Bragg wavelength λ (nm) at room temperature	1550.33	1550.03
Grating length L (mm)	8	8
Initial reflectivity at room temperature R (dB)	12	16.5
Initial amplitude of the refractive index modulation at room temperature Δn	2.5×10^{-4}	4.2×10^{-4}

Reflectivity of hydrogen loaded germanium doped FBG depends on refractive index modulation in the fiber core and indirect related to the amount of the Ge-OH and Si-OH in the UV exposed area of optical fiber core. Obviously, in Figure 2.20, the concentration of Ge-OH for the strong FBG (reflectivity of FBG is close 100%) was directly related to doping concentration of Ge inside the optical fiber core and the distinctness of the refractive index modulation for testing samples was based on the amount of Si-OH.

2.7 Hydrogen treatment -- low-temperature hydrogen loading

The following section is a short description of the hydrogen treatment, loading hydrogen molecules into the conventional telecommunication fiber in low temperature range, used for increasing the photosensitive response of optical fibers.

When placing a fiber in a high-pressure hydrogen atmosphere at room temperature, hydrogen molecules will diffuse into the glass network. Loading the fiber with hydrogen prior to UV exposure significantly increases the photosensitivity [38]. Refractive index changing to as high as ($\Delta n \sim 3x10^{-3}$) [44] were reported for standard hydrogen sensitized telecommunications fiber.

Low temperature high-pressure hydrogen-loading or only simple hydrogen loading is the most common method used for increasing the photosensitivity. In vector analytic terms, the diffusion equations can be expressed for any coordinate system as:

$$\frac{\partial C}{\partial t} = \nabla \bullet (D \times C) \tag{2.11}$$

In cylindrical coordinates where the parameters are r, θ, and z defined in the usual manner, equation (3.1) reduces to

$$\frac{\partial C}{\partial t} = \frac{1}{r}\left\{\frac{\partial}{\partial r}\left(rD\frac{\partial C}{\partial t}\right)+\frac{\partial}{\partial \theta}\left(\frac{D}{r}\frac{\partial C}{\partial \theta}\right)+\frac{\partial}{\partial z}\left(rD\frac{\partial C}{\partial z}\right)\right\} \tag{2.12}$$

where D is the diffusion coefficient having the dimensions L^2T^{-1}, and C is the concentration of the substance undergoing diffusion, defined in any standard way.

As the steady-state diffusion of hydrogen through silica is relatively simple to describe, the diffusion process is quite well characterized by the diffusion equation with a diffusivity given by

$$D = D_0 e^{-E/RT} \tag{2.13}$$

where D_0 is a constant independent of ambient gas pressure and temperature; E is the activation energy for the diffusion process; R = 1.99 cal/K-mol is the gas constant, and T is the absolute temperature. The value of diffusion coefficient that the hydrogen diffuses into the silica is [45]:

$$D = 5.65 \times 10^{-4} e^{-(10.14\ \text{Kcal/mole})/RT}\ \text{cm}^2 s^{-1} \tag{2.14}$$

Here, the problem of diffusion is considered as in a cylinder from first principles, by concern the issue of diffusion in one dimension, for a constant value of D. A fundamental assumption is that the value of D remains a constant for a fixed temperature. Equation (3.1) reduces to [46]

$$\frac{\partial C}{\partial t} = D\frac{\partial^2 C}{\partial x^2} \tag{2.15}$$

Equation 3.5 is the simplest mathematic model of the hydrogen molecular diffusion inside the optical fiber; however, it's an extremely complex process in real hydrogenation of optical fiber. For the conventional optical fiber, the core is doped with germanium to get the light-guiding difference of refractive indices between the fiber core and the cladding. The radii of the core and cladding are 4.1 μm and 62.5 μm, respectively. The polymer layers (two polymers) are 62.5 μm thick and warps around the cladding of the fiber. The structure of the single-mode fiber is depicted in Figure 2.21.

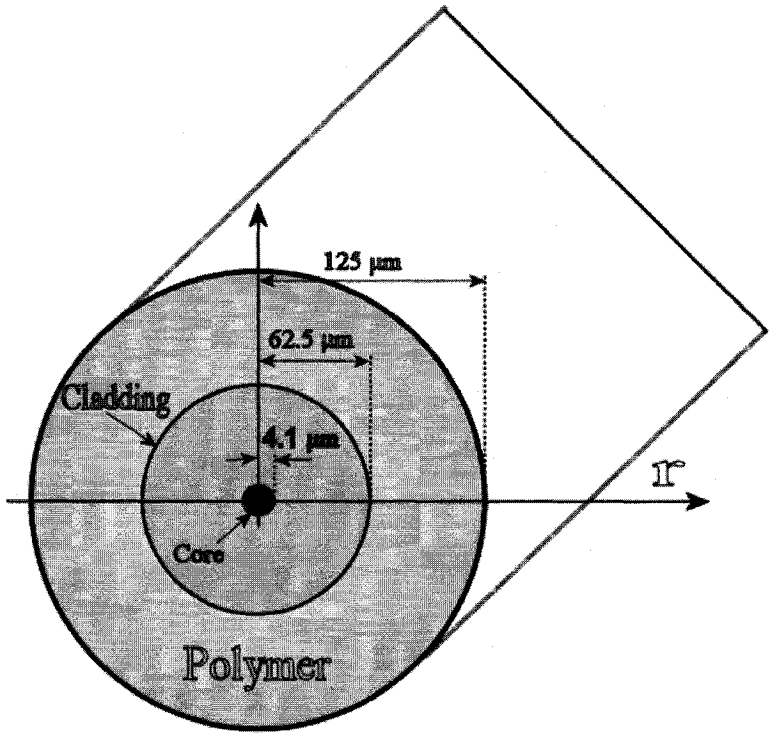

Figure 2.21 *Schematic cross-section of a single-mode fiber: Core (Ge doped silica), Cladding (silica), Polymer (acrylate).*

The concentration of hydrogen molecules and rate of which these molecules diffuse into the core of the optical fiber depend on the pressure and temperature of the hydrogen gas. The pressure of hydrogen gas can increase the saturated hydrogen concentration in the fiber core. Temperature is a significant parameter for the lower temperature hydrogenation. These exhibitions of temperature are: The diffusivity of hydrogen molecules in silica increases with increased temperature. Meanwhile, decreased temperature can result in an increase in the hydrogen concentration saturation level and a significant decrease in the diffusion rate of hydrogen into the core of the optical fiber [16].

The hydrogen concentration in the core of the fiber is related to the pressure of hydrogen in the chamber, diffusion temperature, the type of fibers, and the characteristic

of the FBGs. In general, the grating producer will choose different kind of parameter according to their own data base.

For the design of a hydrogen loading system, safety is of the primary concern given that one is dealing with an explosive gas under high pressure. The fiber chambers are made from copper tubing of small diameter (i.e.1/4 inch). The 1/4 inch copper tubing is capable to hold approximately 20 optical fibers in a small volume, which minimizes the amount of hydrogen required to fill the chamber. The fiber chambers are pumped out with the vacuum pump each time before being filled with high-pressure hydrogen. Heating elements can be placed at various positions along the fiber chamber heating up the hydrogen gas and accelerating the diffusion of hydrogen molecules into the core of optical fiber.

Chapter 3 Fiber Bragg grating temperature sensors and its thermal decay

FBGs have widespread applications in the rapidly growing field of optical sensors. The principle of the dielectric Bragg grating temperature sensor is based on the measurement of the reflected Bragg wavelength. Recently, the most popular design for this kind of sensor is to use the FBG. Fiber gratings are compacting intrinsic to the sensing elements, which are relatively inexpensive to produce, easy to multiplex, and applicable to a range of physical measurands [47]. A FBG is formed by a periodic change in the refractive index caused of a fiber core by exposure to an UV laser beam [22]. Although FBGs are often referring to permanent refractive index structures, exposure to increase temperatures usually results the decay of the refractive index modulation. The grating reflectivity will be erased completely at sufficiently high temperatures.

In order to have a better understanding for next Chapter, this section gives a general overview of the topic regarding FBG temperature sensor and the thermal decay of FBGs.

3.1 Fiber Bragg grating temperature sensors and system configuration

The FBG temperature sensor reflects one particular wavelength and transmits all others and, moreover, the reflected wavelength can vary with the modifying of the sensor's temperature; thus, FBG temperature sensors have been widely used in applications in monitoring temperature. One of the advantages of the FBG temperature sensors is that several of these sensors can be multiplexed in series along with a single optical fiber, so, a single instrument can simultaneously monitor many individual sensors

[47]. Additionally, the FBG temperature sensor also has some other advantages such as immune to EMI, tiny in size, and light in weight.

A FBG is an optical fiber in which the refractive index in the core has a periodic or quasi-periodic profile. One of the most important properties of FBGs is wavelength-selective reflection. Assume that a broadband light is coupled into a fiber with FBG inside. The light that its wavelength matches the Bragg condition will be reflected back. The light that its wavelength does not match the Bragg condition will be transmitted through the fiber.

Mathematically, the Bragg condition is given by [21, 48]:

$$\lambda_B = 2n_{eff}\Lambda \tag{3.1}$$

where λ_B is the Bragg wavelength, n_{eff} is the effective modal index and Λ is the perturbation period.

Most of the work on FBG temperature sensors has focused on the use of these devices providing quasi-distributed point temperature sensing. The thermal response arises due to the inherent thermal expansion of the fiber material as well as the temperature dependence of the refractive index. To explain this phenomenon, we use the following form. The wavelength shift ($\Delta\lambda_B$) as a function of a temperature change (ΔT), for a certain wavelength peak of the mode (λ_B) is given by [47],

$$\frac{\Delta\lambda_B}{\lambda_B} = \left[\frac{1}{n_{eff}}\frac{\partial n_{eff}}{\partial T} + \frac{1}{\Lambda}\frac{\partial \Lambda}{\partial T}\right]\Delta T = (\alpha_{n_{eff}} + \alpha_\Lambda)\Delta T \tag{3.2}$$

where α_Λ is the thermal expansion coefficient and α_n represents the thermo-optical coefficient. Practical values of these constants for typical FBG are $\alpha_\Lambda = 0.55\text{x}10^{-6}\ ^\circ C^{-1}$ and $\alpha_{neff} = 8.8\text{x}10^{-6}\ ^\circ C^{-1}$ [49]. The accuracy of this type temperature sensor can be achieved to

0.7°C (at $\lambda_{Bragg} \sim 1.55$ μm) with a wavelength resolution of 10 pm (0.01 nm), which is the typical wavelength resolution of the optical spectrum analyzer (OSA).

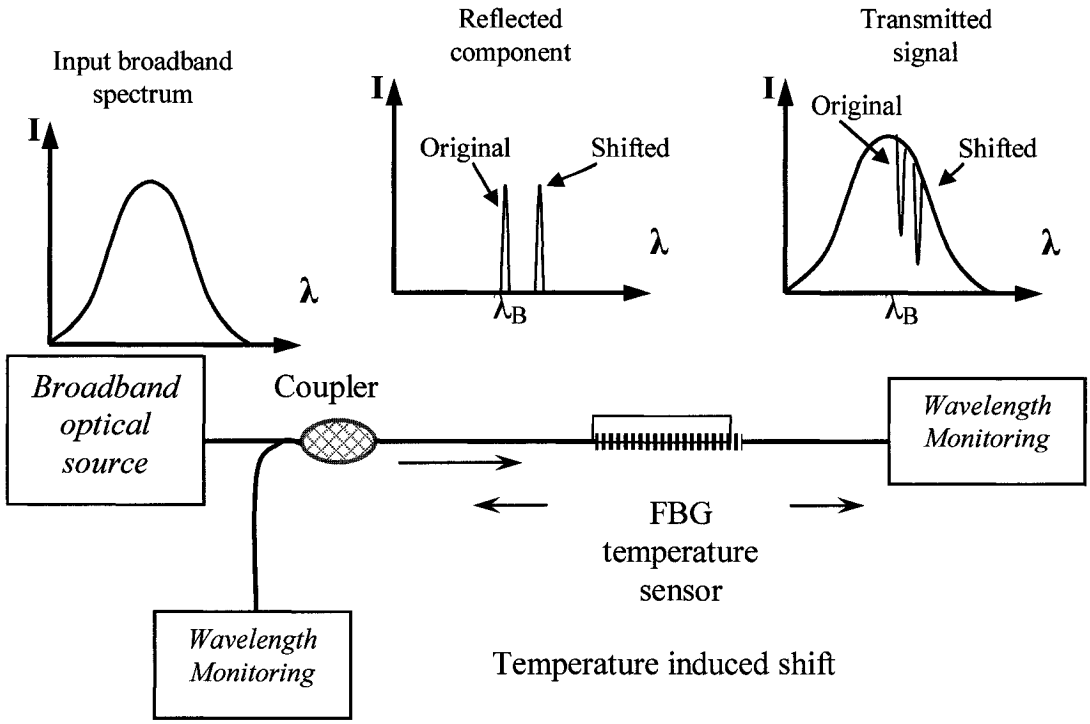

Figure 3.1 *An illustration of fiber Bragg grating-based point sensor.*

Figure 3.1 shows the conceptual configuration of the FBG point temperature sensor. The broadband light source, such as coming from an edge-emitting LED, or a super-luminescent LED or an erbium-doped fiber amplifier, is coupled into a single-mode optical fiber with a FBG inside the fiber. Due to the existence of the grating, the wavelength that match the Bragg condition will be reflected back and the other wavelengths will pass through. Then the wavelength monitoring devices, such as an optical spectrum analyzer (OSA), can be used to monitor the wavelength spectra for both the reflected signal and the transmitted signal, as shown in Figure 3.1.

FBGs are compact intrinsic sensing elements. The nature of the output of Bragg gratings provides the Bragg grating temperature sensors with a built-in self-referencing capability. As the sensed information is encoded directly into wavelength of which it is an absolute parameter, the output does not depend directly on the injected light power, and losses in the connecting fibers as well as couplers. Because this kind of theory is widely acknowledged as one of the important advantages of the FBG temperature sensor, these sensors can be used to measure the temperature precisely in execrable circumstance, and to build the temperature sensor array using wavelength division multiplexing (WDM) and time division multiplexing (TDM) technique.

To sum up, the accuracy of the FBG sensor, especially the FBG temperature sensor, depends on the resolution of wavelength, which is attainable using laboratory instrumentation such as optical spectrum analyzers (OSA) and tunable lasers. Generally, for the conventional FBG temperature sensor, the thermal expansion coefficient (α_Λ) is 0.55×10^{-6} $^\circ C^{-1}$ and the thermo-optical coefficient (α_{neff}) is 8.8×10^{-6} $^\circ C^{-1}$; thus, a wavelength resolution of 10 pm (0.01 nm), which is the maximum wavelength resolution of optical spectrum analyzer AQ6319 in our research laboratory, is required (at $\lambda_B \sim 1.55$ μm) to resolve a temperature change of 0.7 °C.

To increase the accuracy or sensitivity of the FBG temperature sensor, using the technique of an unbalanced Mach-Zehnder interferometer was proposed and implemented [50, 51]. The typical wavelength resolution of this wavelength detection technique is smaller then 1 pm; thus, the sensitivity of the FBG temperature sensor is 0.07 °C. Figure 3.2 shows the basic configuration of applying an unbalanced

interferometer to detect the wavelength shift of the Bragg grating induced by external perturbation.

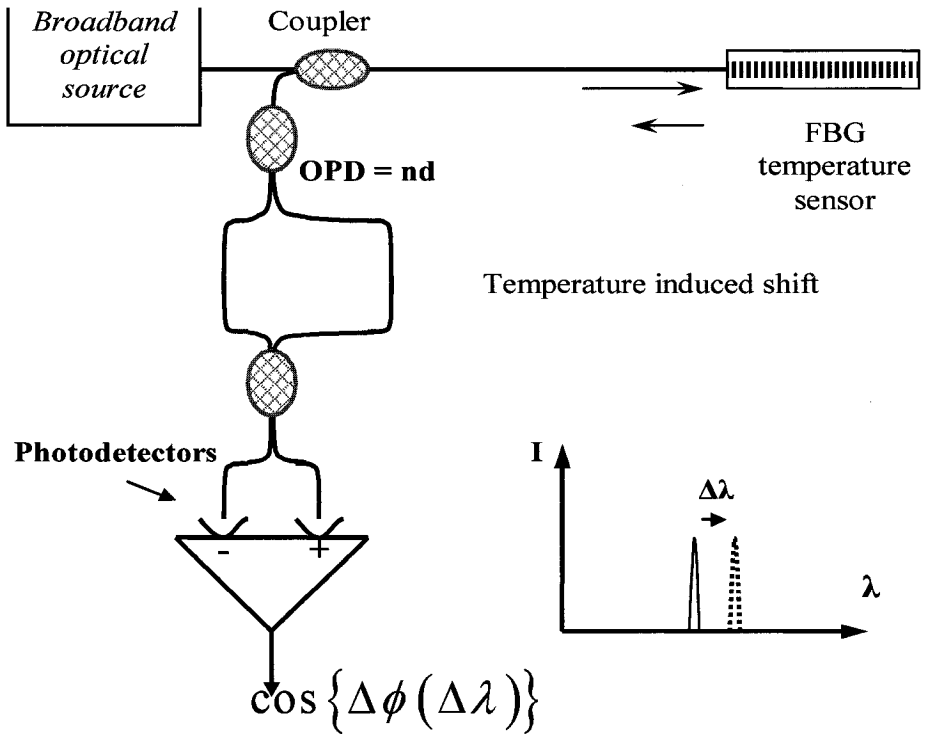

Figure 3.2 *Detection of wavelength shift of fiber Bragg grating temperature sensor is using an unbalanced fiber Mach-Zehnder interferometer.*

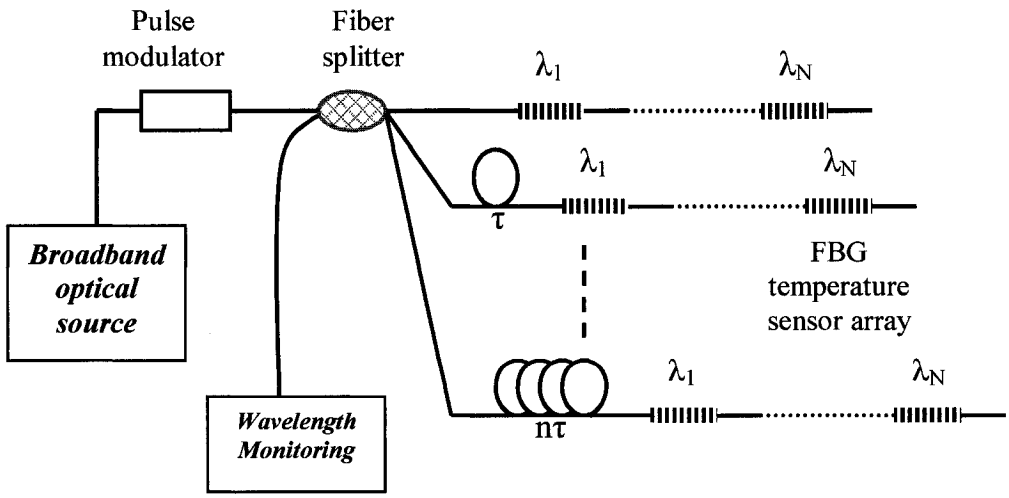

Figure 3.3 *A parallel configuration of combined WDM/TDM multiplexing topology.*

The information capacity is one of the important advantages of the FBG temperature sensors. The benefit of using FBG temperature sensors for distributed sensing is that a large numbers of sensors can be integrated along with a single fiber. Currently, with the rapid advent of optical communication networks, more than 100 wavelength channels can be put in a single fiber by using the wavelength division multiplexing (WDM) technique; hence, if we assign one center wavelength for each grating, more than 100 sensors can be integrated into a single fiber. Furthermore, time division multiplexing (TDM) can multiply above-mention number several times by re-using of the spectrum source. With mixed WDM/TDM in the parallel configuration as in Figure 3.3, several wavelength stepped temperature sensor arrays are concatenated using a fiber splitter. To explain Figure 3.3, the input pulse is split into the FBG temperature sensor arrays. A certain length of fiber delay line separates the time window for each WDM set. By launching a short pulse of light from the source, the reflections from FBG temperature sensors, at longer distant sensor array, will return to the detector at later times. The detection instrumentation is configured to respond to the reflected signals only during a selected window of time after pulse is lunched, because of this reason a WDM/TDM set of sensors is selected for detection.

3.2 Thermal decay of fiber Bragg grating

Some FBG devices require extremely small tolerance on the optical properties over a long time scale to assemble reliable wavelength division multiplexing (WDM) components. Other applications, such as sensors, are required to survive at high temperatures. In the experimental observations of the decay of the gratings' reflectivity, the thermal stability of gratings depends on several factors such as the type of fiber [52],

hydrogenation [53, 54] and the writing wavelength [32]. In 1994, Erdogan *et al.* [55] provided the first detail of grating stability and processed a model to explain the thermal degradation characteristics of FBGs written in germanium and erbium-germanium-co-doped silica fibers. The model demonstrated that the decay of the UV-induced index modulation could be described by a "power law" function of time with a small exponent (<<1). As the experimental results, the UV-induced index modulation initially decays very rapidly, but the rate of decay decreases as time advances, and the decay of grating reflectivity is also a strong function of temperature. In the power-law approach decay measurements are fitted to the following equation:

$$\eta = \frac{1}{1 + A(t/t_1)^{\alpha}} \tag{3.3}$$

where η is the normalized index change (which be described as $\Delta n(t)/\Delta n_0$), t is time, the fitting parameters A and exponent α are proportional to $exp(\alpha T)$ and T respectively. In this equation both A and α are dimensionless, and $t_1 \equiv 1$ minute is induced to keep dimension consistent. Once the parameters (A and α) have been determined, the decay at any temperature and time phase can be calculated using Equation 3.3. The difficulty with this approach is to determine reliable fitting parameters for different types of fibers [55, 56]. As shown in Figure 3.4, the data of Erdogan's experimental observations appear to fit Equation 3.3 equally well. The fitting parameter, exponent α, was chosen to be $\alpha = T/T_0$ with $T_0 = 5250$ K. The factor A can be written in form

$$A = A_0 \exp(aT) \tag{3.4}$$

with the temperature T measured in Kelvin $A_0 = (1.86 \pm 0.22) \times 10^{-3}$ and $a = (7.64 \pm 0.19) \times 10^{-3}$ K^{-1}. Figure 3.5 shows the dependence of the power-law factor A

on temperature, with plotted on a logarithmic scale. In this plot the error bars represent the values for an obtained directly from nonlinear curve fits using Equation 3.3 in which both A and α were allowed to vary freely.

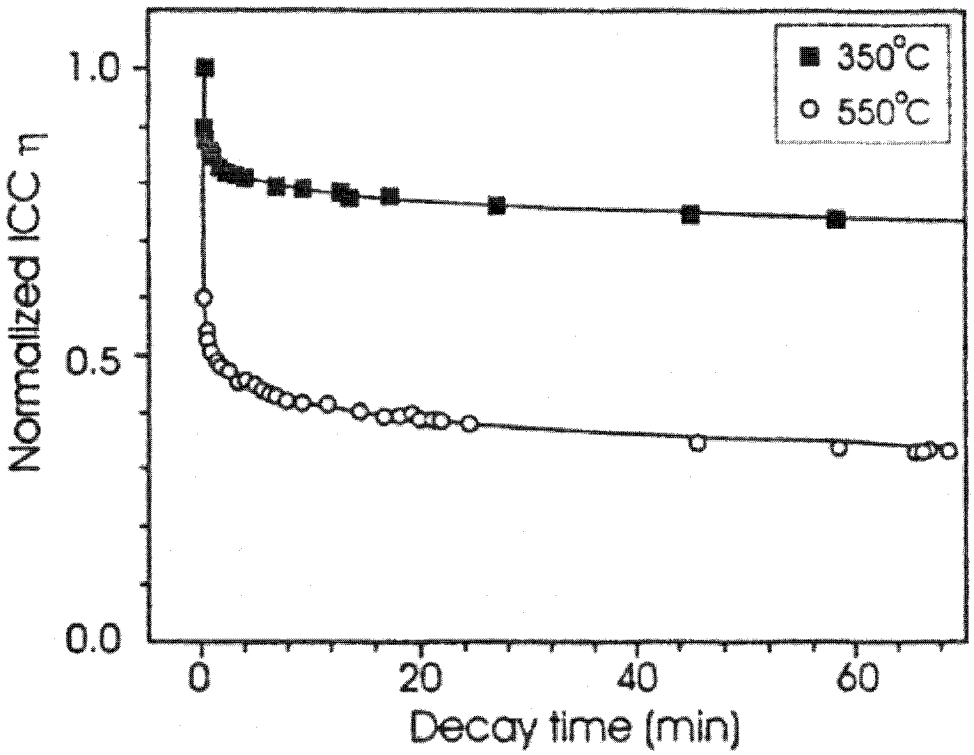

Figure 3.4 *Measured integrated coupling constant normalized to starting value for two gratings heated to 350 and 550°C as a function of decay time. Solid lines are fits to Equation 3.3* [55].

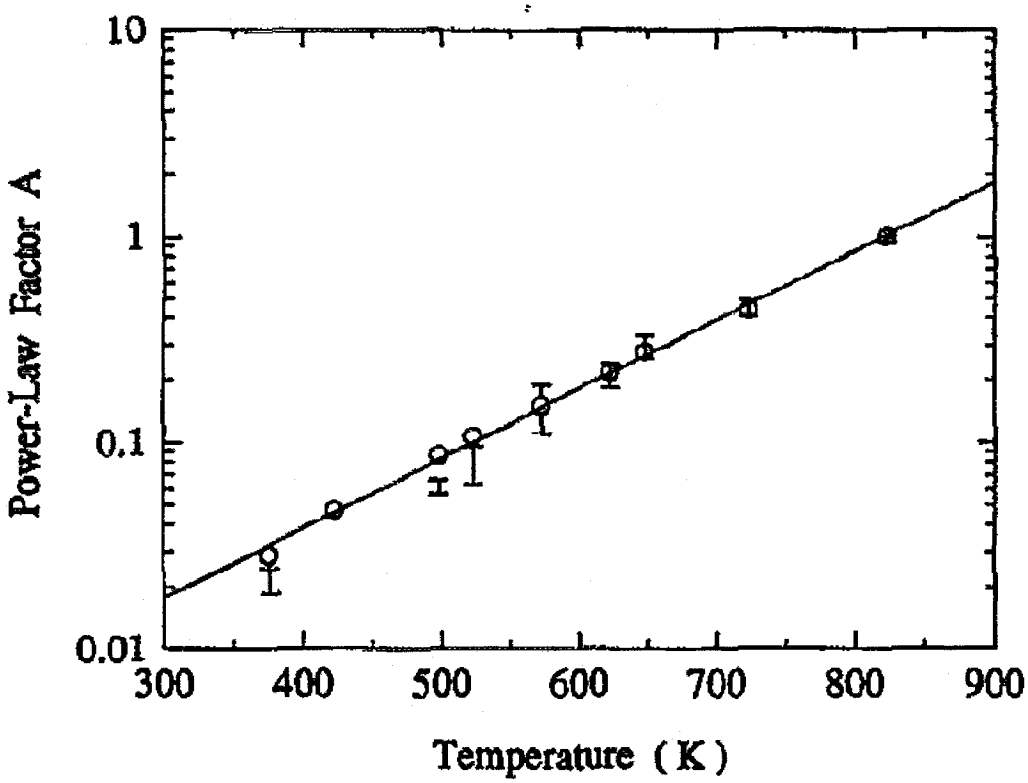

Figure 3.5 *The power law factor A that obtained from curve of Equation 3.3 with α is allowed to vary freely (error bars), and α fixed by α=T/5250 K (open circles)* [55].

A model might be modified to predict the measured behavior [55]. Carriers are excited by the UV irradiation from the single homogeneously broadened absorption spectrum by GODCs at 5 eV. The carriers are then assumed trapped in a continuous distribution of the energy states, rather than at a single trap level. If we consider that it is the breakage of the wrong bonds that creates defects and free electrons, then it is plausible to assume the thermal excitation of these electrons from traps can lead to the reformation of the wrong bond, simultaneously removing the UV-induced index change. The dissociation energy E_a of the trap follows a simple Arrhenius law of the form

$$\frac{\Delta n(t)}{\Delta n_0} = \exp(-\nu t) \tag{3.5}$$

where ν is a frequency factor related to E_a, temperature T, and Boltzmann's constant K_B via $\nu(T) = \nu_0 \exp(-E_a / K_B T)$. Clearly, this is not the case for standard or hydrogenated fibers, as the Arrhenius law predicts that at a constant temperature the trap depopulation as well as the index modulation should decay exponentially to zero, rather than reaching a plateau [55]; therefore, the correct description is the one in which almost all electrons up to a given trap depth, instead of a fraction of electrons at a single trap, are wrap out by the decay process; by this token, the decay history is important in determining the subsequent behavior. Figure 3.6 shows a simplified diagram for this mechanism. $E = 0$ is the point where electrons are free (the conduction band minimum). The thermal releasing of electrons induces the reoccupation of original deep level occupied prior to UV excitation. The essence of the diagram is the separation of the distribution of trapped carriers into energies above and below demarcation energy E_d that depends on time phase and temperature. It is consequently convenient to interpret the experimental data in term of E_d, where $E_d = K_B T \ln(\nu t)$, where ν is obtained by acquiring multiple data sets as a function of temperature and fitting them together.

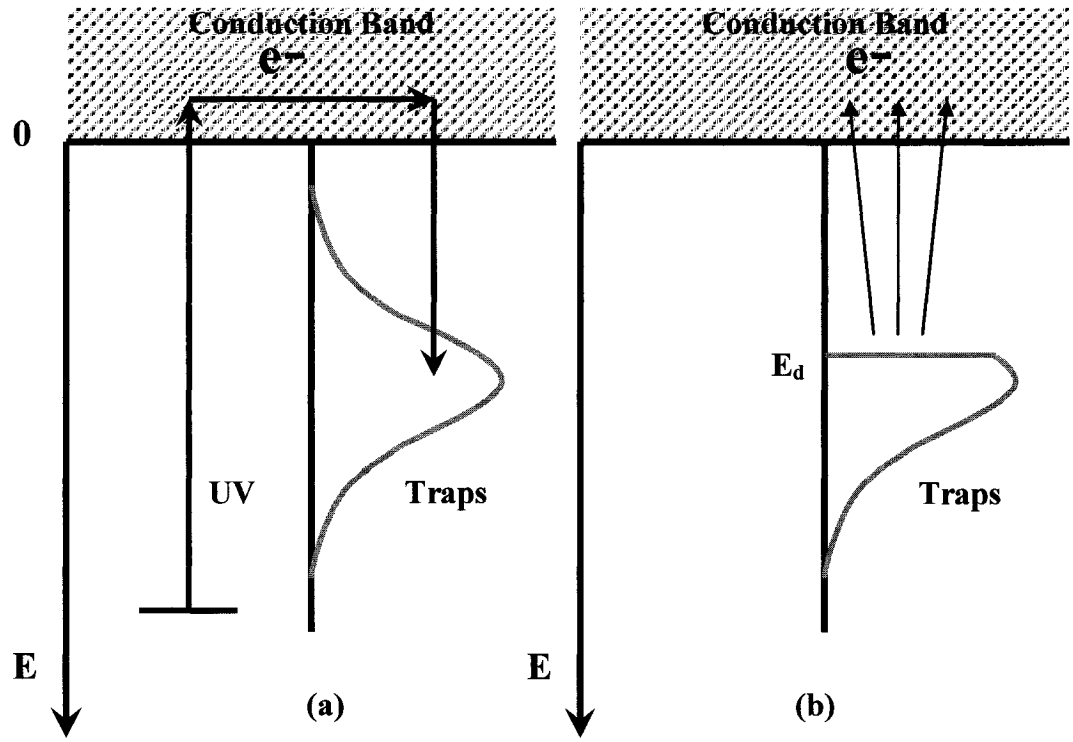

Figure 3.6 *Diagram of the physical model in which (a) electrons excited by UV excitation are trapped in a continuous distribution of traps; and (b) thermal depopulation of the traps at a given time and temperature approximately corresponds to shallower traps ($E<E_d$) being emptied and deeper traps ($E>E_d$) remaining full.*

In Figure 3.7 the experimentally determined values for η (assumed proportional to *N*, the total number of trapped electrons remaining at a given time phase) are plotted versus the demarcation energy E_d. The different symbols correspond to the different decay experiments performed at various temperatures. Plotting the change in reflective index modulation as a function of the demarcation energy gives the aging curve. The parameter η may also be written as

$$\eta = \frac{1}{1+\exp\left[\left(E_d - \Delta E\right)/K_B T_0\right]} \tag{3.6}$$

This form represents a simple analytical form for the dependence of the normalized UV induced index change on the demarcation energy E_d; hence, the aging of the grating should be predicted. From the experimental data of Figure 3.5 and the corresponding fit, the energy distribution of the traps (ΔE) is ~2.8 eV deep, with a width of 1.6 eV. Figure 3.7 immediately suggests which combinations of time and temperature are capable for erasing a given fraction $1-\eta$ of the initial UV induced index change.

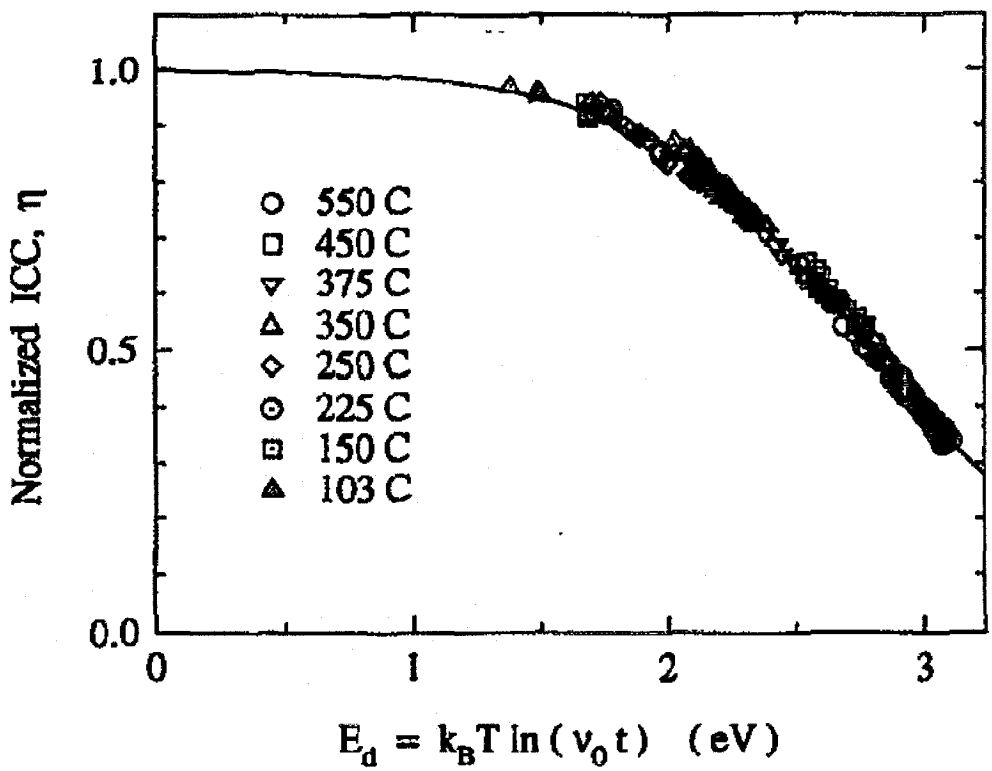

Figure 3.7 *The normalized integrated coupling constant is a function of the demarcation energy E_d. The solid line is a fit using equation 3.6* [55].

3.3 Blue shifting of fiber Bragg grating

A FBG is an optical fiber that the refractive index in the core has a periodic or quasi-periodic profile. One of the most important properties of FBGs is wavelength-

selective reflection. Assume that a broadband light is coupled into a fiber with FBG inside. The light whose wavelength matches the Bragg condition will be reflected back. The light whose wavelength does not match the Bragg condition will be transmitted through the fiber. The mathematical bragg wavelength condition shows in Equation 3.1

For the uniform grating, the maximum reflectance can be expressed as [16]

$$R(L,\lambda) = \tanh^2(\Omega L) \tag{3.7}$$

where L is the grating length. For the single-mode sinusoidal modulated grating, the coupling constant Ω is given by [47]:

$$\Omega = \frac{\pi \Delta n}{\lambda}\eta \tag{3.8}$$

where η is the fraction of the fiber mode power contained by the fiber core , which can be approximately expressed as

$$\eta = 1 - V^2 \tag{3.9}$$

where V is the normalized frequency of the fiber and it given by $V = (2\pi a/\lambda)\sqrt{n_{co}^2 - n_{cl}^2}$, where a is the core radius and n_{co} and n_{cl} are the core and cladding refractive indices, respectively.

Figure 3.8 shows the relationship between the reflectivity and the amplitude of the refractive index modulation for different effective grating length.

The amplitude of the refractive index modulation in the core of the fiber can be determined from the following:

$$\Delta n_{\mathrm{mod}} = \frac{\lambda}{\pi L_{eff}\eta} \tanh^{-1}\left[(1 - T_{\mathrm{min}})^{1/2}\right] \qquad (3.10)$$

where L_{eff} is the effective length of grating and T_{min} is the minimum transmission at Bragg wavelength, i.e. the grating peak reflectivity $R = 1 - T_{\mathrm{min}}$.

According to Equation 3.10, we assume, if the L_{eff} is a constant value, than the amplitude of refractive index modulation is proportion to the grating peak reflectivity and it will be reduced when the FBG thermal decay accrue.

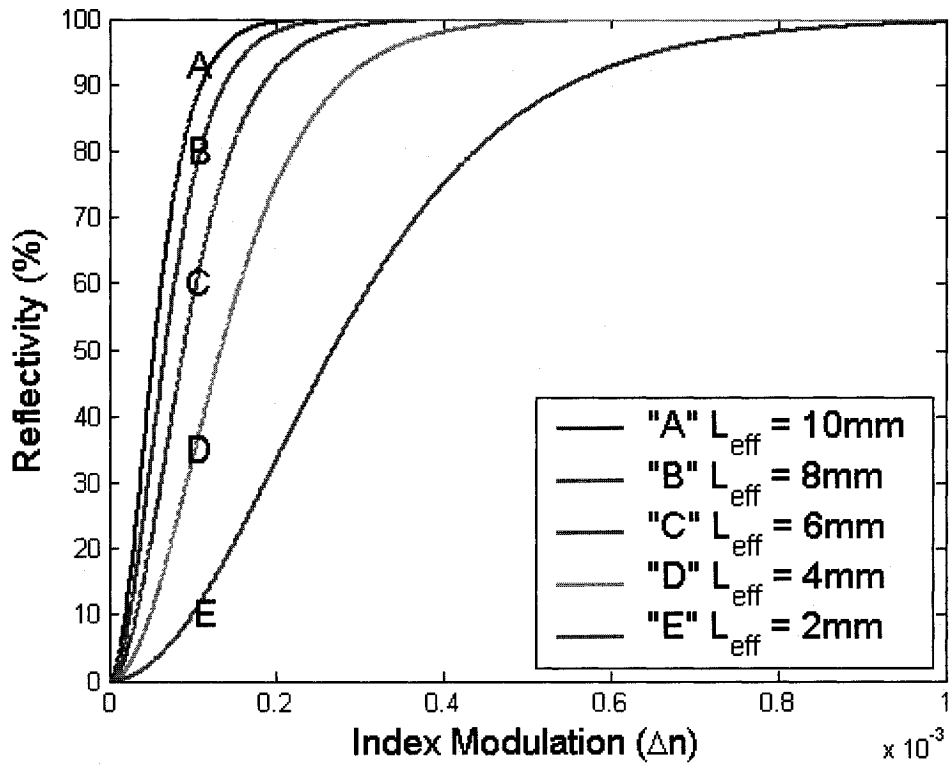

Figure 3.8 *Reflectivity (R) versus refractive Index modulation (Δn) of fiber Bragg grating for different effective grating length. a:* $L_{eff} = 10\,\mathrm{mm}$, *b:* $L_{eff} = 8\,\mathrm{mm}$, *c:* $L_{eff} = 6\,\mathrm{mm}$, *d:* $L_{eff} = 4\,\mathrm{mm}$, *e:* $L_{eff} = 2\,\mathrm{mm}$ [49].

Based on Equation 3.1, the Bragg wavelength could be shorted, when the amplitude of refractive index modulation was reduced caused by the thermal decay of FBG.

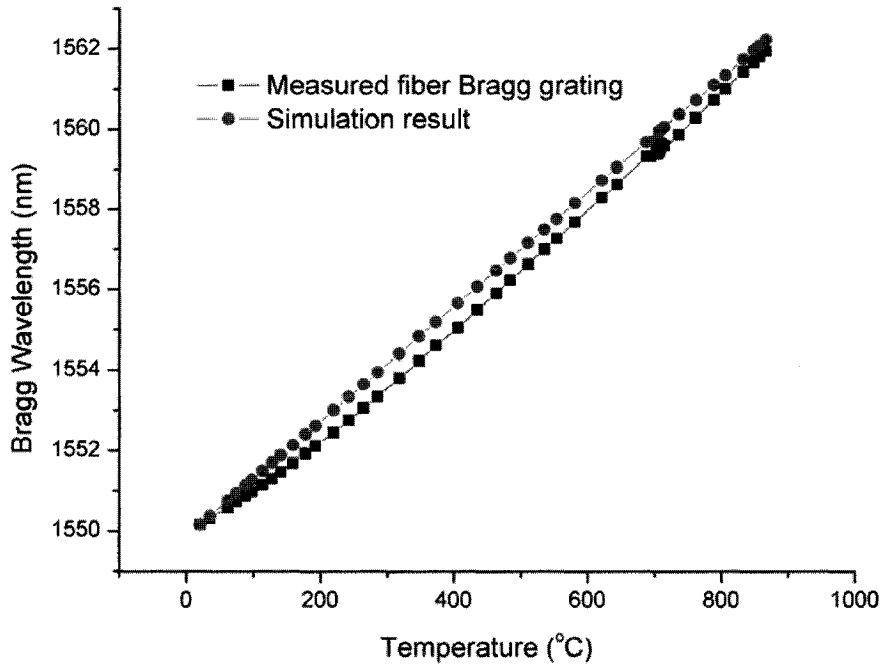

Figure 3.9 *Bragg wavelength versus temperature for hydrogen-loaded fiber Bragg grating* [49].

Whenever the temperature of a FBG changes, the Bragg wavelength (λ_B) shift toward a long wavelength with any increase of temperature due to the thermal effect on refractive index modulation and thermal expansion effect grating period. However, if we keep a non-annealed FBG at any constant temperature (isothermal annealing), a small but non-ignored shift of the Bragg wavelength toward a shorter wavelength was observed with time which correspond to our theory. This observational phenomenon is called "blue shift". The shift of Bragg wavelength λ_B with temperature for the grating fabricated in

hydrogen loaded conventional fiber is shown in Figure 3.9. In our experiment, we observed a very strong blue shift, when we annealed a fresh hydrogen-loaded FBG sample at temperature 703 ^{o}C for approximately two hours. Figure 3.10 shows the shifting of Bragg wavelength in a thermal annealing process.

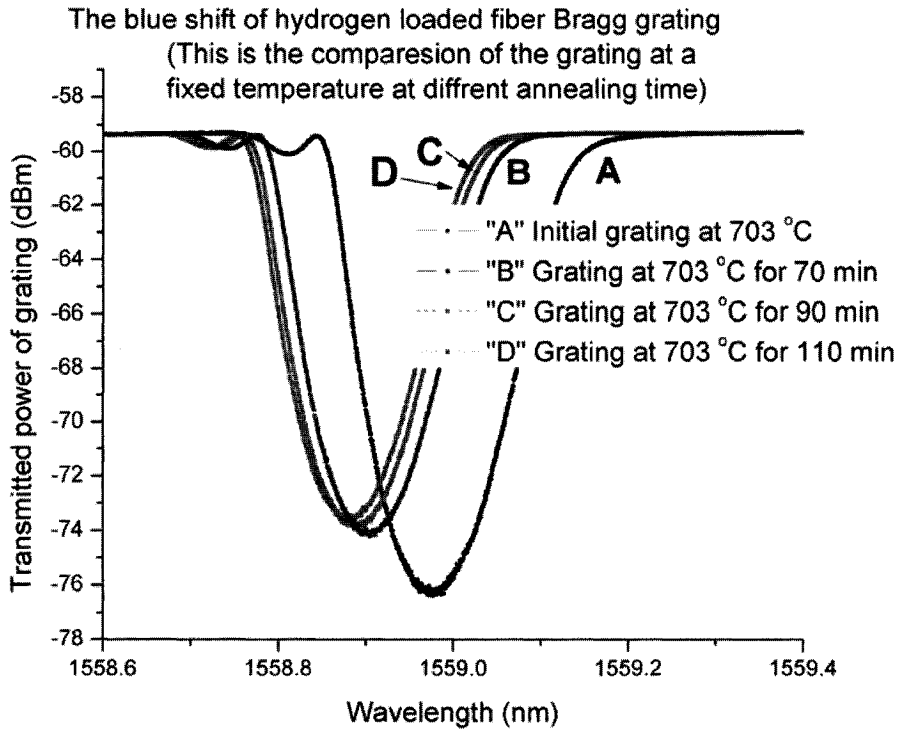

Figure 3.10 *Spectra showing the blue shift of Bragg wavelength written in hydrogen loaded Ge doped fiber at annealing temperature 703.7 °C for about two hours* [49].

The time dependences of grating reflectivity and the Bragg wavelength in iso-thermal annealing process are shown in Figure 3.11. The grating reflectivity and the Bragg wavelength exhibit the similar trend in the isothermal annealing process with an initial rapid decay in the first one hour following by a substantially decreased rate of decay in the rest annealing time.

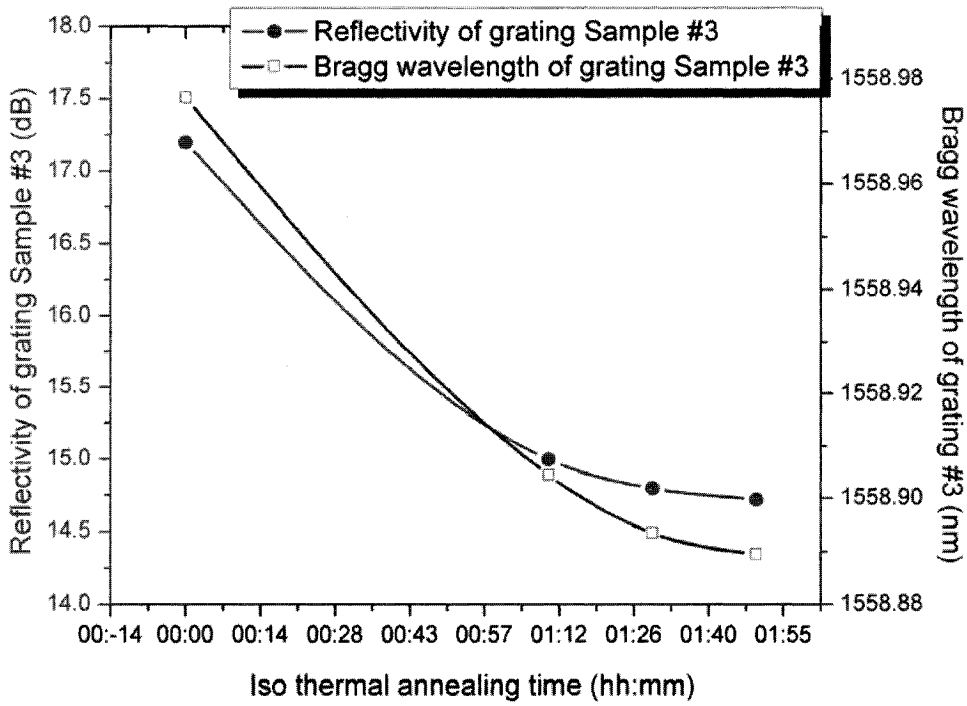

Figure 3.11 *Graph shows the blue shift of Bragg wavelength and the decay of the reflectivity written in hydrogen loaded Ge doped fiber at annealing temperature 703.7 °C for about two hours* [57].

The principal of FBG temperature sensor is based on the detection of the Bragg wavelength shifting. It has several advantages over other temperature sensors. However, the thermal decay and the "blue shift" will limit the usage of FBG temperature sensor in high temperature environmental. To overcome these problems, we will post our research results for the high temperature resistant FBG temperature sensor in next chapter.

Chapter 4 High temperature fiber Bragg grating sensors

4.1 Background

The mechanism of the fringe pattern UV laser induced refractive index changes, as described in previous chapters, has been attributed to the creation of defects, stress relaxation or compaction of the glass structure. The grating temperature limit for thermal stability of UV induced defects can be roughly estimated to be 100-700 °C [39], depending on the type of FBG.

The decay mechanism can be associated to the recombination of defects, as described by Erdogan (see Chapter 3). Likewise, the upper limit of thermal stability for refractive index changes attributed to UV induced stress relaxation or compaction, which is generally higher compared to UV induced defects, can be estimated to be 400-1000 °C, depending on the type of fiber. The decay mechanism in this case could be linked to a temperature at which the viscosity of the glass allows strained bonds and the glass structure to relax towards equilibrium [58]. To improve the temperature stability of FBGs, new dopants could be identified that result in more stable UV induced defects. Another possibility could be to increase the viscosity of the glass.

Another possible way to fabricate more permanent gratings could be using UV induced phase separation or crystallization, which has been observed in GeO_2 doped silica films [59] and SnO_2 doped fibers [60]. However, as the non-exposed regions may also undergo phase separation, when the sensor is exposed to high temperatures, such gratings would not necessarily result in higher thermal stability of the refractive index modulation.

Even if unexposed regions do not undergo phase separation, the exposed areas may experience continued phase separation or crystal growth, resulting in non-stable grating characteristics (increasing or decreasing reflectivity). At the other hand, at higher temperatures diffusion of dopands within the fiber not only limits the stability of gratings, but ultimately limits the thermal stability of the fiber itself.

In 1996, a method was proposed to create high-temperature stable Bragg gratings by periodically altering the concentration of fluorine in the core of the fiber [61]. A change in the fluorine concentration would subsequently result in a change in the refractive index. The limiting thermal stability of such a refractive index structure would depend on the diffusing properties of fluorine. The proposed method to alter the fluorine concentration in the core was based on the chemical Equation 4.1. This equation was proposed by Kirchhof *et al* for the reduction of hydroxyl groups in fluorine doped silica [62]. The reduction of hydroxyl groups was attributed to formation and diffusion of hydrogen fluoride, which was assumed to have a higher mobility than bound fluorine. A different way of looking at the Equation 4.1, is that there is a reduction of fluorine in hydroxyl doped regions.

$$\equiv Si-OH + F-Si \equiv \xrightarrow{Heat} \equiv Si-O-Si \equiv + HF \qquad (4.1)$$

Introduction of hydroxyl groups in the core of the fiber can be achieved either thermally or by UV exposure of hydrogen loaded fibers (see Chapter 2). By using fringed UV exposure, hydroxyl formation can be achieved locally with the periodicity of the interference pattern, creating sub-micron structures. FBGs in which the refractive index modulation is a result of a change in the chemical composition are referred to chemical composition gratings (CCGs).

Although, the Sn-O_2 and fluorine doped FBGs have extremely thermal stability, which are stable at temperature around 1000 °C, but their refractive indices are not compatible with the existing optical system. And high cost of the special Tin and Fluorine doped fibers is also limited the applications.

In this chapter, we will present our research on the low cost high temperature resistance FBG, which is based on hydrogen-loaded FBG. Our experimental results show that the bleaching temperature for this novel FBG, molecular-water induced FBG, exceeds 1100 °C [63] with acceptable reflectivity.

4.2 High temperature hydrogen-loaded FBG

High pressure hydrogenation of germanium doped fibers can significantly enhance photosensitivity within optical fibers and produce strong FBGs with 248 nm fringe pattern UV laser [15]. One explanation for this phenomenon can be deduced from the concentration of germanium–oxygen-deficient center (GODC) [16, 20] and drawing induced defect (DID, a trapped hole with an oxygen vacancy) [20, 29] inside optical fiber. Ge-O bonds play an important role during the index change process. These bonds are broken by UV laser and then react with hydrogen to produce a hydroxyl and a DID. Once the FBG exposed to high temperature, the DID will decompose into a GODC. The Ge-O bonds are weaker than Si-O bonds (Ge-O-Ge is 4.2 eV, Ge-O-Si is 4.5 eV, and Si-O is 5 eV) [30] and the Ge-O bonds can be more readily broken by low energy radiation. One of the weakest bond from the three bonds of the DID will be broken by annealing treatment. Therefore the thermal induced structural change from DID into the GODC is the principal cause of thermal decay of FBG refractivity.

In the experimental observations of the decay of the reflectivity, the thermal stability of gratings depends on several factors such as the type of fiber [52], hydrogenation [53, 54] and the writing wavelength [32]. In 1994, Erdogan *et al.* [55] provided the first detail of grating stability and provided a model to explain the thermal degradation characteristics of FBGs written in germanium and erbium-germanium-co-doped silica fibers. The model demonstrated that the decay of the UV-induced index modulation could be described by a "power law" function (Equation 3.3, Chapter 3) of time with a small exponent (<<1). As the experimental results (Figure 4.1) show, the UV-induced index modulation initially decays very rapidly. The decay is time dependent and it is also sensitive to temperature.

Figure 4.1 demonstrates that the reflectivity decay of tested FBG is 96% after it was placed in a temperature around 700 °C for 2 and half hours [64]. This shows that the annealing temperature has a limited effect on the reflectivity decay of the sensor.

As the experimental results show, the reflectivity of hydrogen loaded FBGs exhibit the similar tendency for all tested grating samples in the isothermal annealing process with an initial rapid decay in a short duration and following with a substantially decreasing rate of decay in an extended period.

Hydrogenation has inarguable advantages in the fabrication of FBG, such as compatibility with standard communication fibers, easy to use, and low cost. However, the hydrogen-loaded FBGs exhibit poor thermal stability within the high temperature environment.

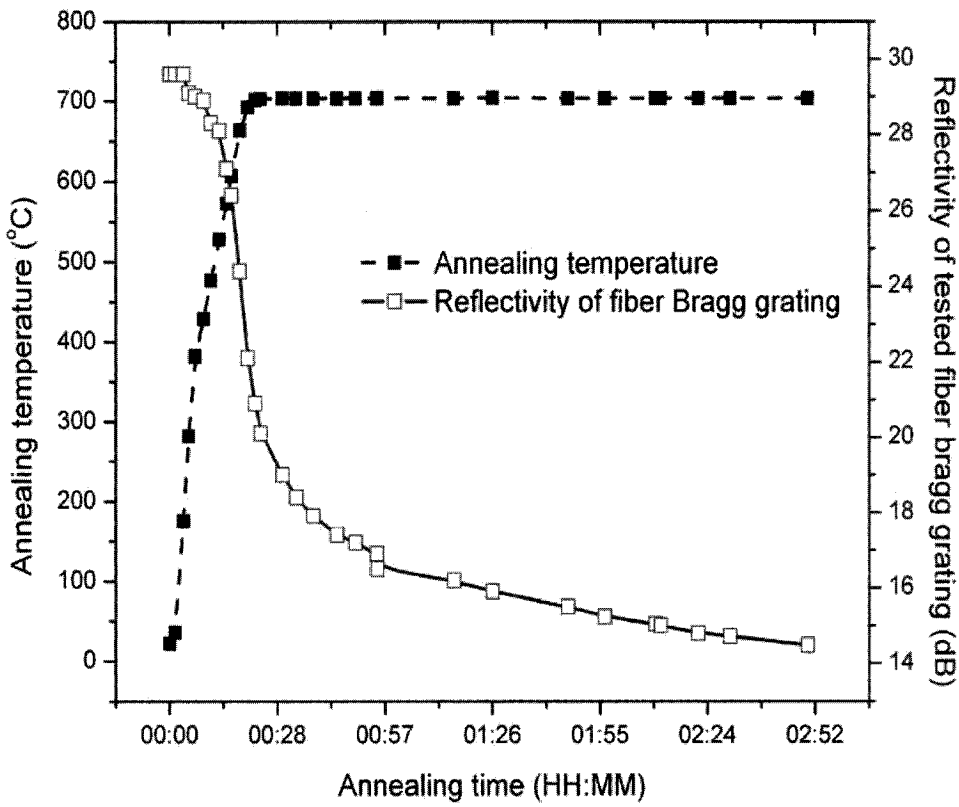

Figure 4.1 *700 °C isothermal annealing process for hydrogen loaded fiber Bragg grating* [64].

There are many reports in the literature [65] have stated that the thermal annealing (treatment) of FBG can increase the thermal stability. Annealing a fiber involves raising the glass to a temperature above the strain point for a short time and slowly cooling back to room temperature. This process not only reduces stress in the glass, but also initiates a number of physical and chemical changes to the glass.

A high temperature hydrogen loaded FBG model proposed by Zhang and Kahriz [66], showed that the thermal stability depends on the reflective index modulation of hydrogen-loaded FBG and the isothermal annealing treatment can increase the thermal stability. The reflectivity of a FBG related to the index modulation of the fiber core in the

grating region, created by exposing the fiber to a UV laser pattern. The elevated temperature activates some of the unstable defects generated during grating inscription [66]. This can strongly diminish the index modulation amplitude, leading to reduction of the grating reflectivity. Additionally, decreasing of Bragg wavelength as a consequence of thermal treatment is also related to the index modulation decay.

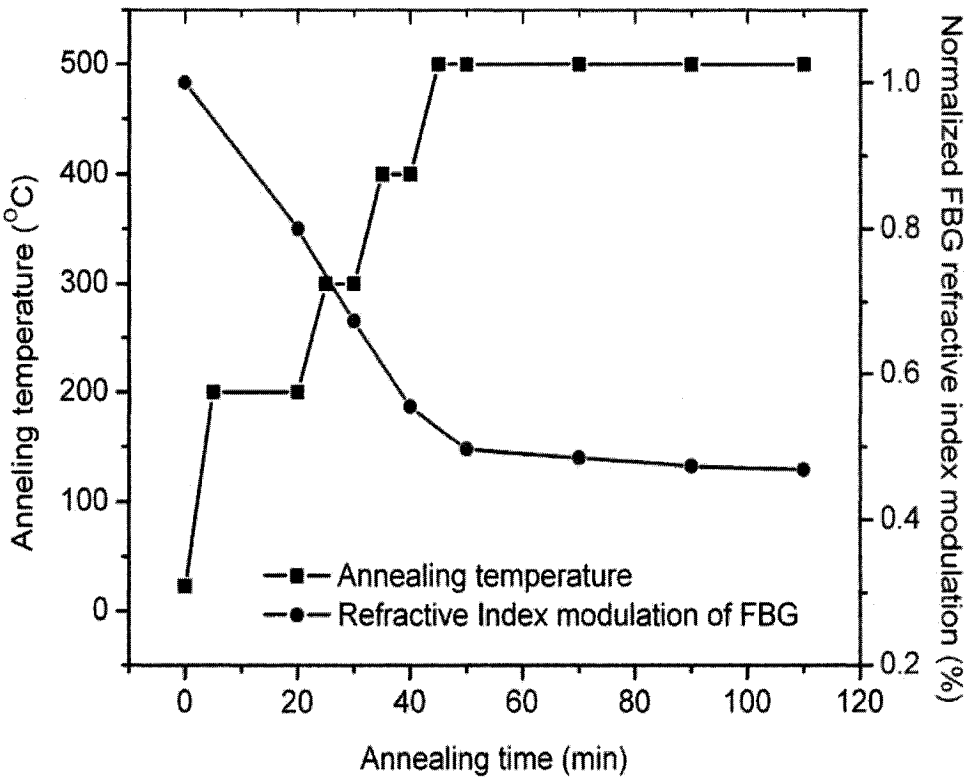

Figure 4.2 *Reflectivity decay in thermal annealing process for hydrogen loaded fiber Bragg grating. The test specimen has 12 dB reflectivity and the initial amplitude of the refractive index modulation Δn at room temperature, 1550.33 nm Bragg wavelength, and 0.4 nm FWHM is* $2.5x10^{-4}$.

For the experimental investigation of the thermal stability for hydrogen-loaded FBGs, the reflectivity spectra have been monitored during the thermal annealing process.

Typical results obtained at high temperatures with the hydrogen loaded FBGs can be observed in Figure 4.2.

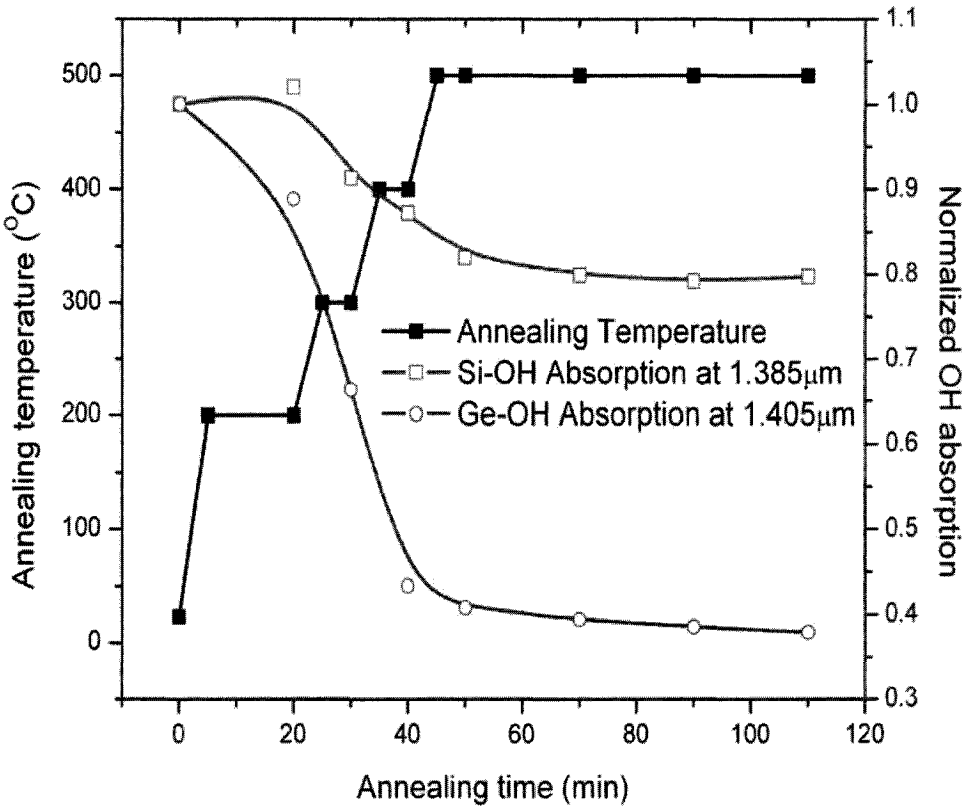

Figure 4.3 *The hydroxyl absorption decay in thermal annealing process for hydrogen loaded fiber Bragg grating. The test specimen has 12 dB reflectivity and the initial amplitude of the refractive index modulation Δn at room temperature, 1550.33 nm Bragg wavelength, and 0.4 nm FWHM is* $2.5x10^{-4}$ [67].

Exposing FBG to UV laser causes Si-OH and Ge-OH defects formation which permanently enhances the ultraviolet photosensitivity response once it is treated by hydrogen. The concentrations of Ge-OH and Si-OH inside the fiber core depend on the concentration of GODC. Therefore, the grating reflectivity of hydrogen-loaded germanium-doped FBG depends on refractive index modulation in the fiber core i.e. it is

related to the amount of the Ge-OH and Si-OH. Figure 4.3 shows the changes of normalized hydroxyl absorption in the thermal annealing process.

To fabricate a hydrogen-loaded FBG, a hydrogen loaded fiber is exposed to 248 nm fringe pattern UV laser, and then annealed at 350° C for 40 second. Under this operation, unwanted hydrogen molecules will be removed from the core of fiber. For the OH absorption experiment of hydrogen loaded FBG, the sample was annealed inside the furnace from room temperature (22.5 °C) up to 500 °C. At each step of 100 degree, the sensor was treated with isothermal annealing for 10 minutes. After each step, the OH absorption spectrum and the reflectivity were measured.

Figure 4.3 is synoptically described the relationship between the components of Ge-OH, and Si-OH. The weak bonds between germanium (Ge) and hydroxyl (OH) are less thermal stable compare to the Si-OH group. Therefore, the absorption of Ge-OH was decreased sharply and the group was almost completely decomposed at annealing temperature of 500 °C. We have shown hypothetically [66] that the thermal stability of hydrogen loaded FBG is related to the amount of Si-OH and the thermal decay of FBG is inversely proportional to the refractive index modulation. The results of the normalized refractive index modulation shown in Figures 4.3, and 4.4 confirm our hypothesis once more.

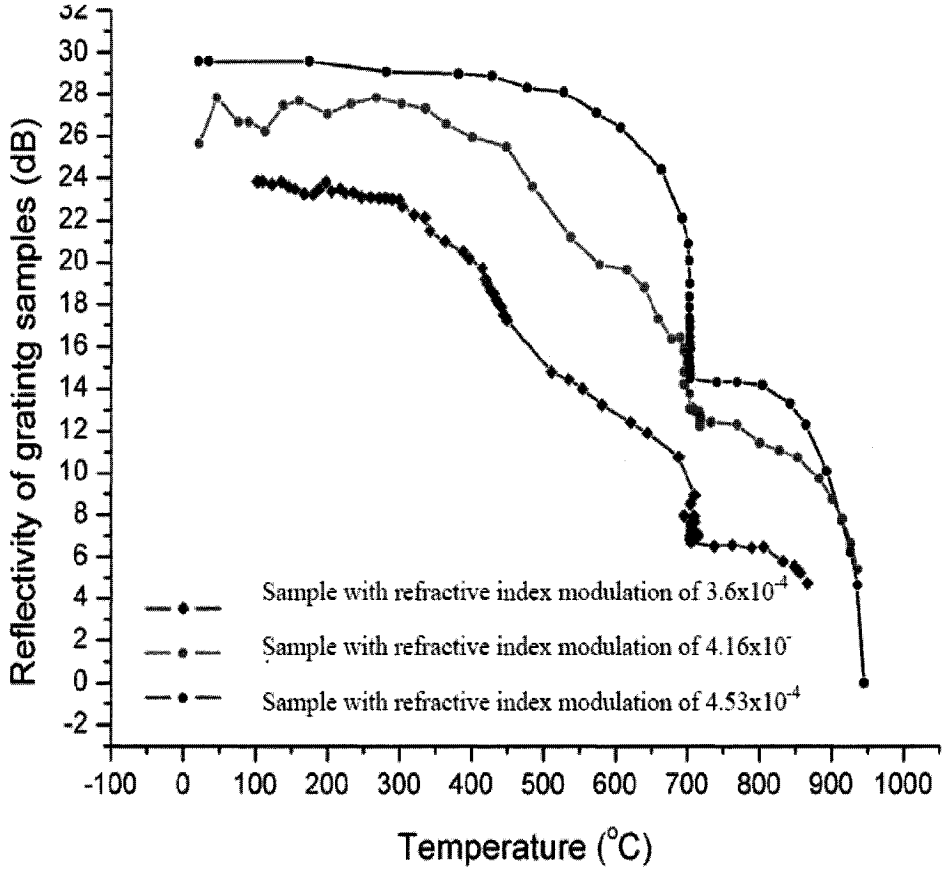

Figure 4.4 *The thermal decay of tested grating samples from room temperature to about 950 °C* [64].

Increasing the reflectivity of hydrogen loaded FBG will result the thermal stability of the device, however, the reflectivity can not be beyond 35 dB, due to the vibration of the FBG writing process [40].

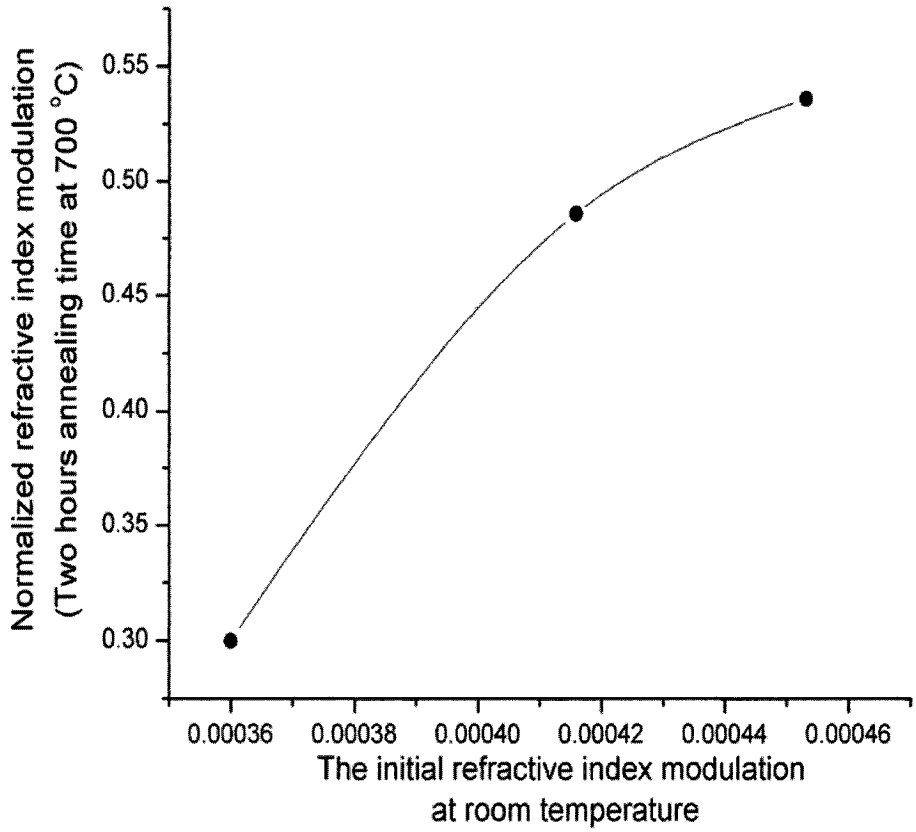

Figure 4.5 *The graph shows the relationship between the normalized refractive index modulation and the initial refractive index modulation for all tested fiber Bragg gratings in isothermal annealing process after two hours.*

Conclusion: The reflectivity of a FBG is related to the index modulation of the fiber core in the grating region, created by exposing it to the UV pattern. The elevated temperature activates some of the unstable defects generated during grating fabrication. This can strongly diminish the index modulation amplitude, leading to reduction in the grating reflectivity. In other words, the thermal stability of FBG is related to the amplitude of refractive index modulation in the grating area (see Figure 4.5).

4.3 Design of molecular-water induced high temperature FBG

As we discussed above, the thermal stability of hydrogen-loaded FBG can be enhanced by increasing the amplitude of refractive index modulation in the grating area. However, the hydrogen-loaded FBG still faces the thermal erasing problem and shows in Figure 4.6.

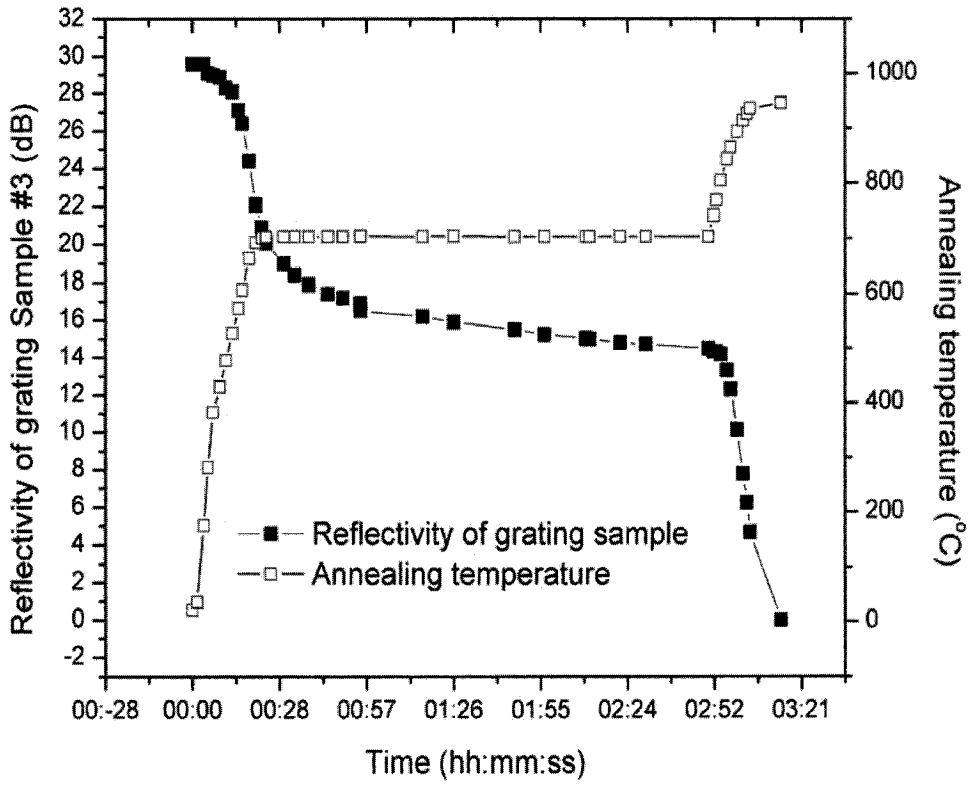

Figure 4.6 *Erasing temperature for a strong hydrogen-loaded fiber Bragg grating sample (30 dB) is around 936 °C with 10 minutes erasing time.*

The Ge-O bonds are weaker than Si-O bonds (Ge-O-Ge is 4.2 eV, Ge-O-Si is 4.5 eV, and Si-O is 5 eV) [30] and the Ge-O bonds can be more readily broken by low energy radiation. One of the weakest bond from three bonds of the DID (trapped hole

with an oxygen vacancy) will be broken by annealing treatment. Therefore the thermal induced structural change from DID into the GODC is the principal cause of thermal decay of FBG refractivity, Figure 4.7.

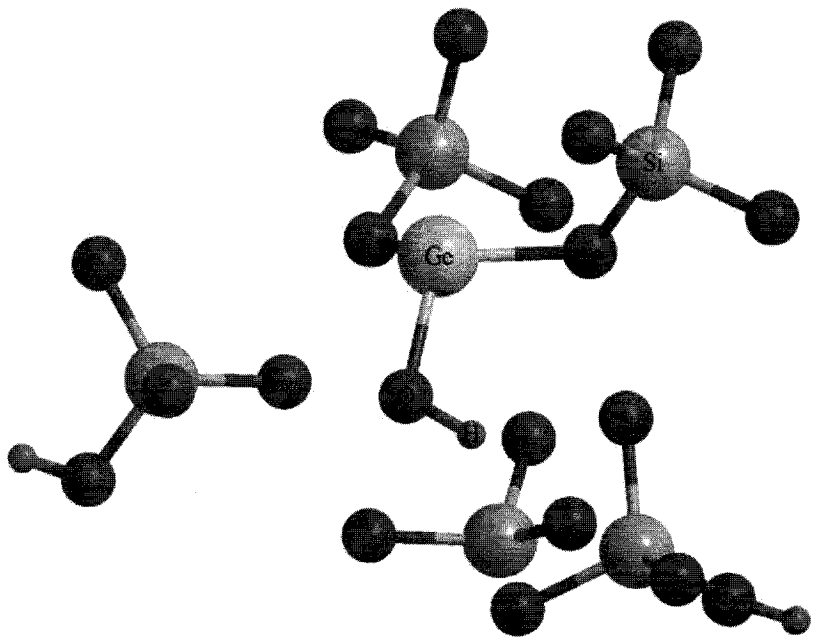

Model above illustrates the original hydrogen-loaded FBG structure
Model below shows the hydrogen-loaded FBG structure after thermal annealing

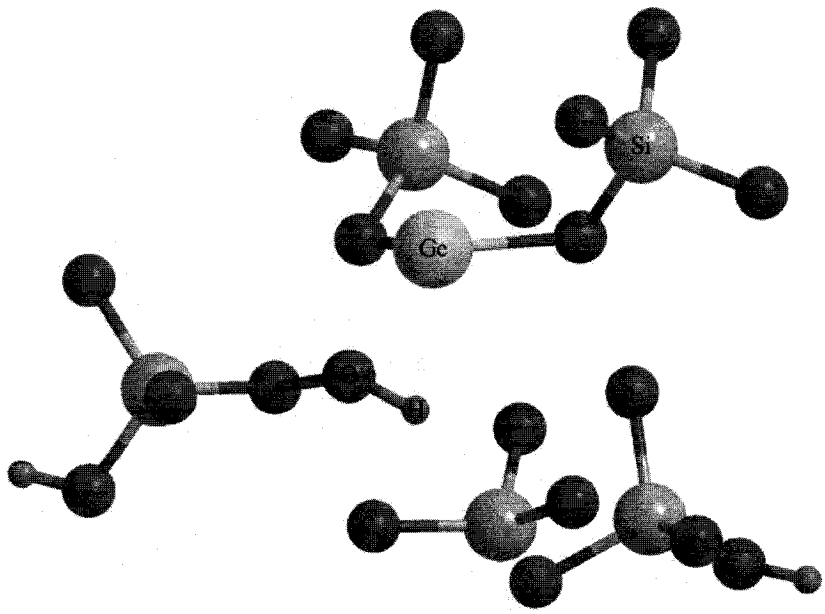

Figure 4.7 *The thermal induced structural change from DID into the GODC is the principal cause of thermal decay of FBG refractivity.*

The thermal stability of hydrogen loaded FBG is limited by the bonding energy of Ge-O bond. This standpoint has been proved by experimental results (Figure 4.6). The highest thermal erasing temperature of hydrogen-loaded FBG is around 940 °C.

FBG high temperature sensor in the temperature monitoring system requires extremely small tolerance on the optical properties over a long time scale to assemble reliable wavelength division multiplexing (WDM) components, and also requires extremely temperature stability over a wide temperature range. The FBG reflectivity decay is the key factor for design and development of high temperature resistant FBG temperature sensor. Our experimental results, Figure 3.10, 3.11, and 4.6, show the fast thermal decay and Bragg wavelength shifting, when the hydrogen-loaded FBG place in the high temperature ambient. The sensing temperature range for the hydrogen-loaded FBG is less than the expected value.

As we explained above, the formation of hydrogen loaded FBG is based on the Ge doped silica structure changed from GODC to the DID. The unstable DID structure can be vibrated by absorbing heat energy, while the hydrogen-loaded FBG is placed in the high temperature ambient. The weakest bond among the three bonds of DID structure is easily broken and resulting the decay of hydrogen-loaded FBG reflectivity.

In order to increase the thermal stability for high temperature resistance FBG temperature sensor, another structure has to be found to replace the DID structure in the FBG area. The new structure should meet the following points:

- The new structure should be more stable than the DID structure.

- The new FBG should be based on the hydrogen-loaded FBG and with limited treatment, in order to reduce the cost and be compatible with existing optical system.
- The new structure should have high bonding energy to the silica or very low diffusivity in the fiber.

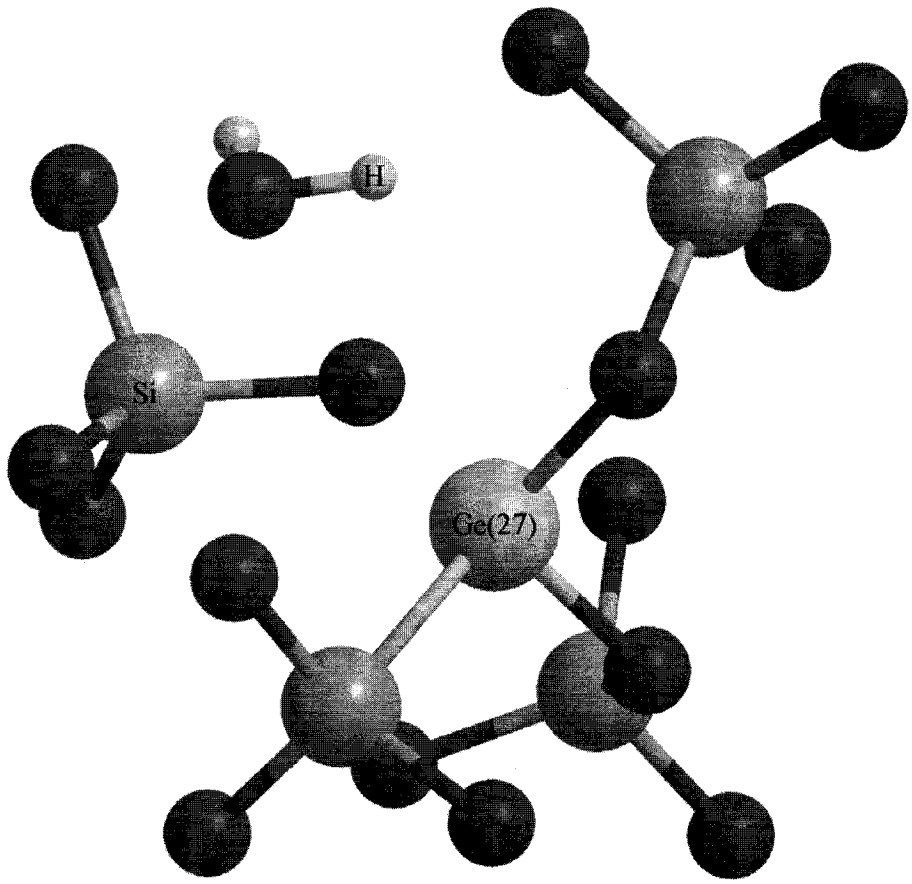

Figure 4.8 *The important elements and water molecule in the hydrogen-loaded FBG are displayed in this model.*

Figure 4.8 shows Ge, Si, Oxygen, and Hydroxyl are the four basic elements of the hydrogen-loaded FBG. Water molecule is an important impurity in the hydrogen-loaded FBG and formatted during the formation of hydrogen-loaded FBG.

Molecular-water impurity is the only independent micro-structure inside the hydrogen-loaded FBG. The bonding energy for H-OH is around 5.2 eV (498KJ/mol), and the refractive index is around 1.33 at 1550nm. The high temperature resistance FBG would be fabricated, if the concentration of molecular water can follow the sequence to modify the refractive index periodicity inside the FBG area.

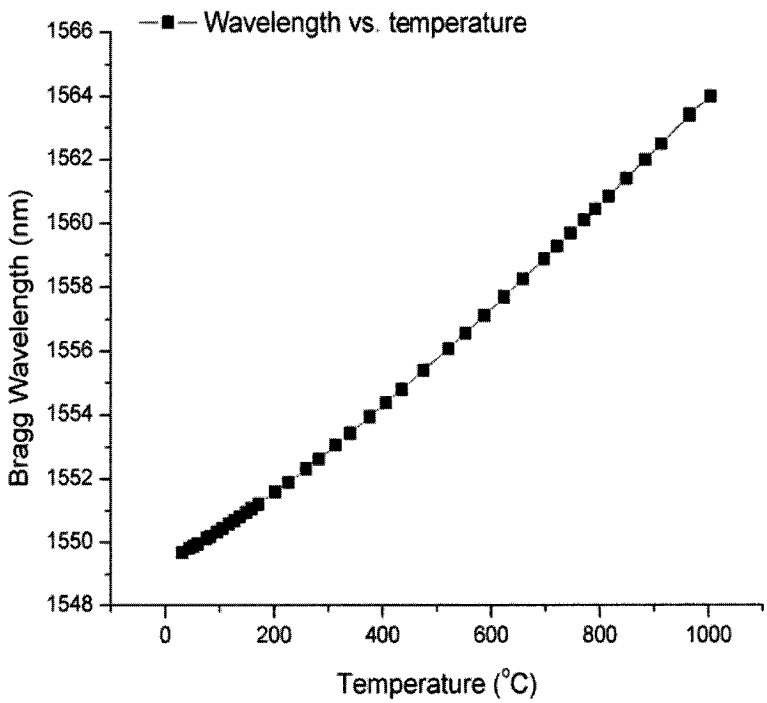

Figure 4.9 *Graph shows the Bragg wavelength versus temperature for the molecular-water induced of fiber Bragg grating.*

In order to verify the design of molecular-water induced FBG, a molecular-water induced FBG was fabricated in our lab. The testing results show the molecular-water induced FBG can be survived at temperature in excess of 1000 °C. Figure 4.9 shows the relationship of this new type FBG between Bragg wavelength and temperature. Figure 4.10 reveals the reflectivity of this molecular-water induced FBG from room temperature up to around 1000 °C.

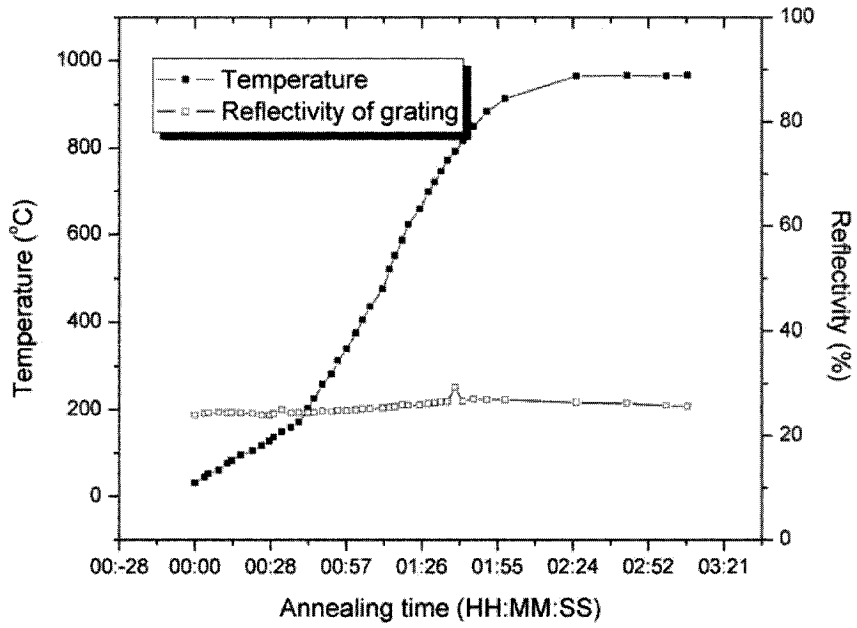

Figure 4.10 *Graph shows the reflectivity versus temperature for the molecular-water induced of fiber Bragg grating.*

4.4 Fabrication of molecular-water induced high temperature resistant FBG

The main principle of molecular-water induced FBG is to modulate the fiber refractive index using molecular water. The advantages of this formation for the new type of FBG in optical fiber can be describer as following. First of all, , the decomposability of molecular water is almost impossible at the temperature from the deep freeze to the melting temperature of silica [67] due to the strong bonding of the molecular water. From this point of view, we can find out the difference between the molecular water FBG and the conventional FBG – the surviving temperature of the molecular water FBG is much higher than the erasing temperature of conventional hydrogen loaded FBG. Secondly, the

molecular water has low diffusivity of (D_{H2O} = 2x10^{-7} cm^2/s at 1000 °C [68]) in the silica fiber.

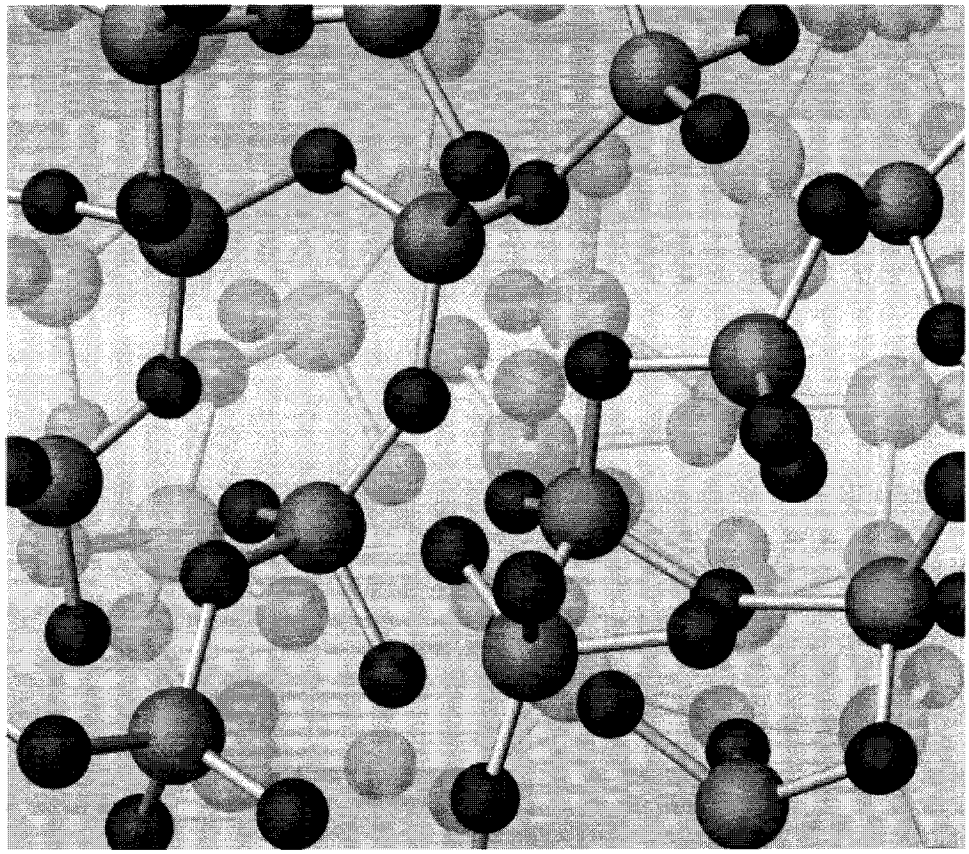

Figure 4.11 *Fused silica structure.*

Optical glass fiber, which is a fused silica as shown in Figure 4.11, is a continued tetrahedral structure and formed by strong, directional covalent bonds. Fused glass has a well-defined local structure: four oxygen atoms enclose a silicon atom and share corners to create cages that are only a nanometer across. The molecular water in the silica is usually fettered in the silica cages that can not diffuse out through the silica net. In general, the known models of water diffusion in the fused glass are based on kinetic scheme of water interaction with silica matrix forming hydroxyl groups; however, they

can not be used in this case, as the molecular waters are formed from the silica matrix, forming hydroxyl groups.

At high temperature range, the molecular water will be diffused from higher concentration segments to the lower concentration parts; however, this diffusion process is extremely slow. Figure 4.10 shows the molecular-water induced FBG has much higher thermal stability compared with hydrogen-loaded FBG.

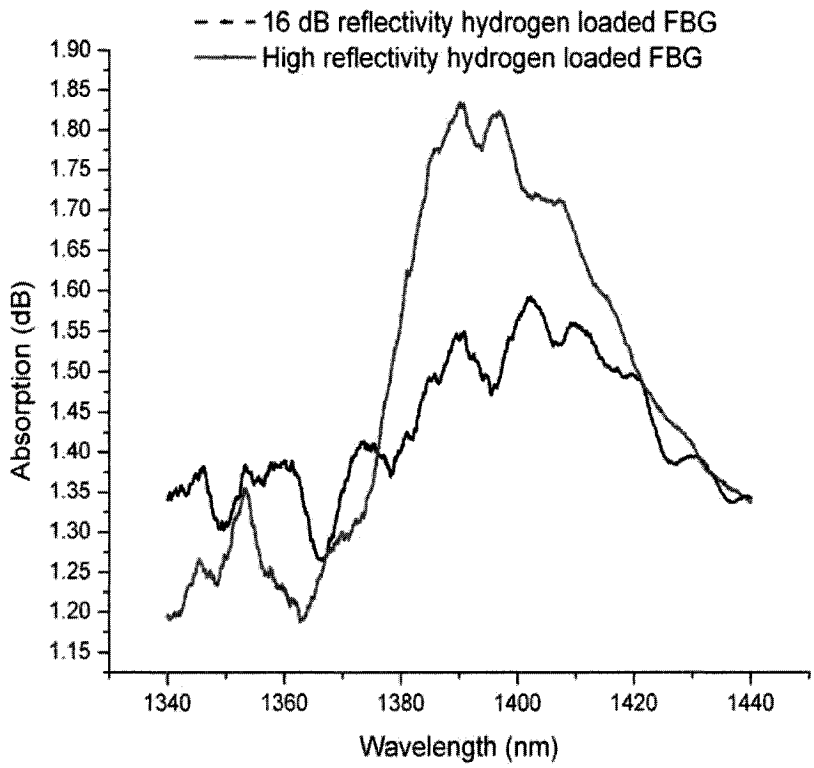

Figure 4.12 *Absorption spectra of hydrogen loaded FBG near 1.4 μm. The molecular water has peak absorption at 1.42 um.*

Molecular-water is one of the impurities inside optical fiber core. The near infrared absorption of molecular water had peak absorption at 1.42 μm, it is shown in Figure 4.12. However, the spectrum profile of absorption for water was commonly covered up by the spectrum profile of Ge-OH absorption.

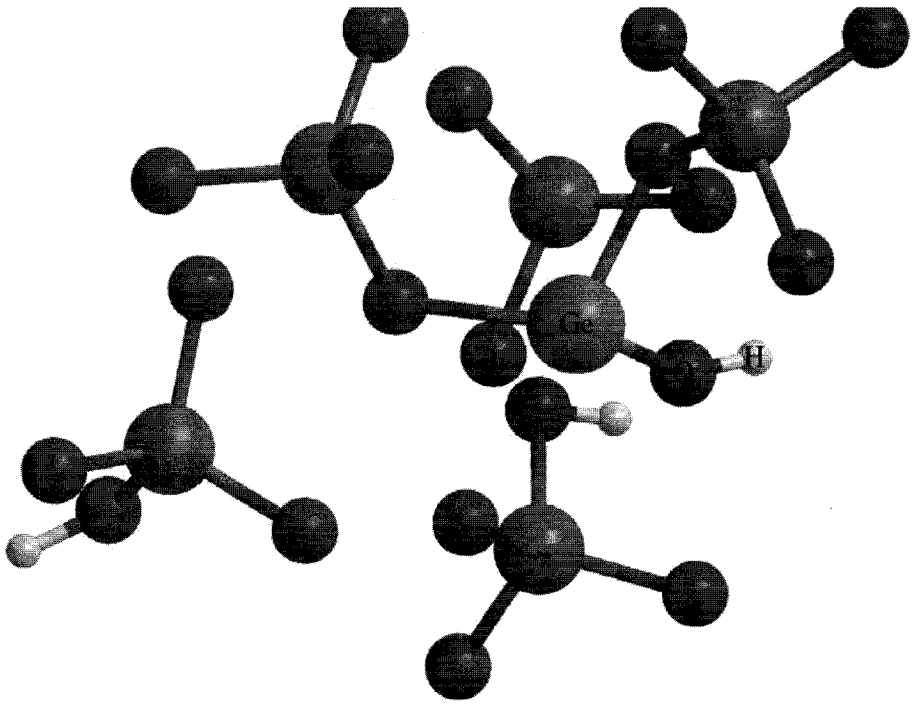

Model above shows the original hydrogen-loaded FBG structure
Model below shows the structure diagram for the formation of molecular water

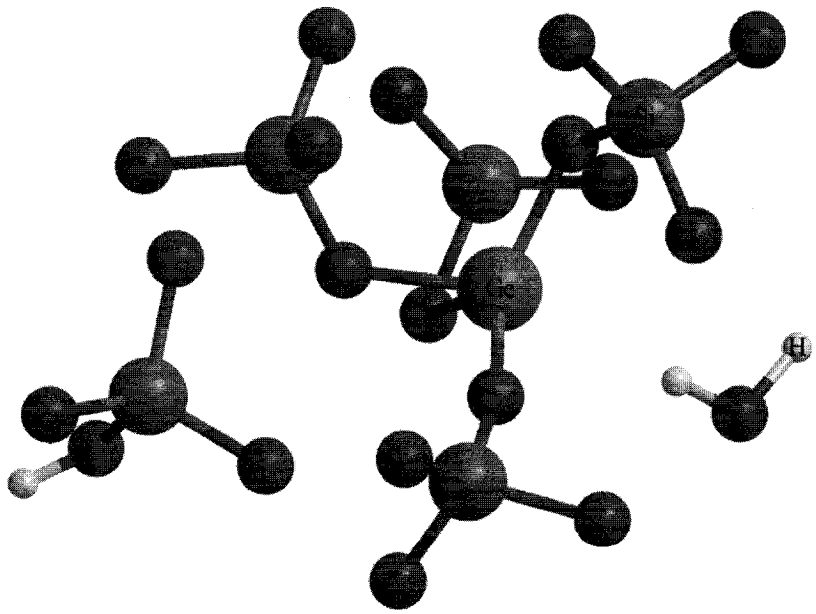

Figure 4.13 *Model shows the structure diagram for the formation of molecular water in the FBG area.*

The formation of molecular water in an FBG is shown in equations 4.2, 4.3, 4.4, 4.5 and Figure 4.13. The Ge-OH and Si-OH will be formed during the writing process for the hydrogen loaded conventional FBG using fringed UV laser. When we increased the treatment energy (temperature) of the FBG, the Ge-OH and Si-OH have been decomposed, and produced the Ge-O and Si-O lattices, and water molecule inside the germanium doped optical fiber.

$$-Ge-O-Ge\equiv+H-H \xrightarrow{h\nu} Ge\vdots+2(H-O-Ge\equiv) \tag{4.2}$$

$$2(H-O-Ge\equiv)\longleftrightarrow Ge-O-Ge+H_2O \tag{4.3}$$

$$-Si-O-Si\equiv+H-H \xrightarrow{h\nu} Si\vdots+2(H-O-Si\equiv) \tag{4.4}$$

$$2(H-O-Si\equiv)\longleftrightarrow Si-O-Si+H_2O \tag{4.5}$$

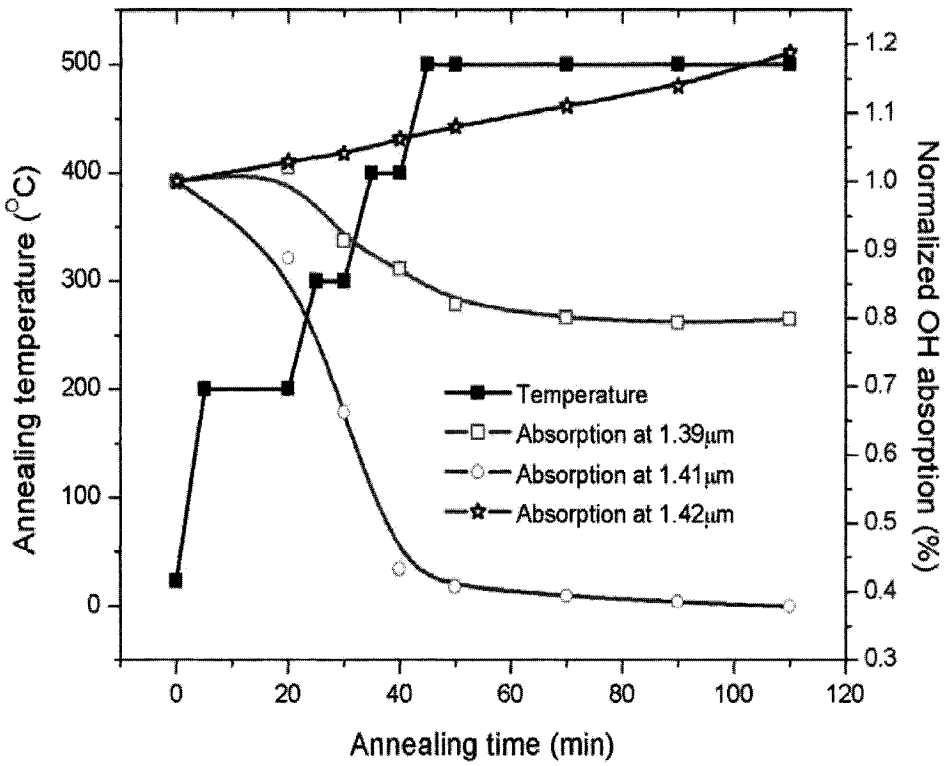

Figure 4.14 *Absorption spectra of hydrogen loaded FBG near 1.4 μm. Normalized magnitude changes of Si-OH absorption (1.39 μm), Ge-OH absorption (1.41 μm), and water absorption (1.42 μm) versus annealing temperature.*

The refractive index modulation of the molecular water FBG can be considered to be formatted by the periodic change of molecular-water inside fiber. The relationship between molecular-water composition and the decomposition of the Ge-OH and Si-OH displays in Figure 4.14.

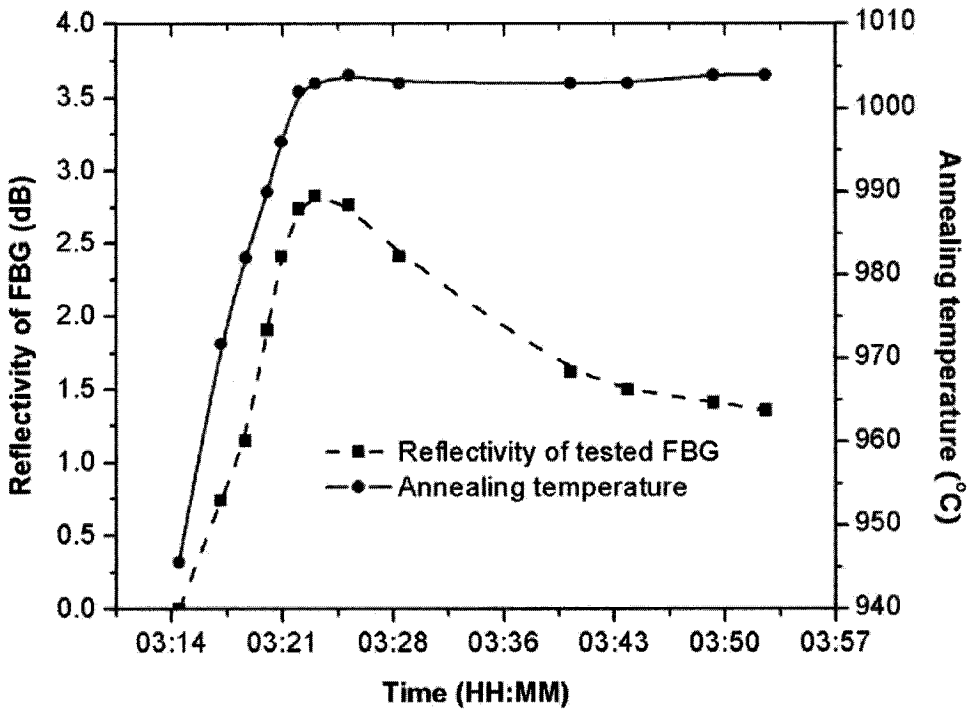

Figure 4.15 *molecular-water induced high temperature resistant fiber Bragg grating was fabricated using hydrogen loaded conventional fiber Bragg grating at temperature around 1000 °C.*

Molecular water is the essential part of the high temperature resistance FBG. In our experiments, the molecular-water induced reflectivity was observed starting at temperature around 950 °C. The molecular-water induced reflectivity of high temperature resistance FBG, which is shown in Figure 4.15, can be described as two correlative steps: the grating grown up (950 °C to 1000 °C) and the grating stabilization (isothermal annealing at 1005 °C).

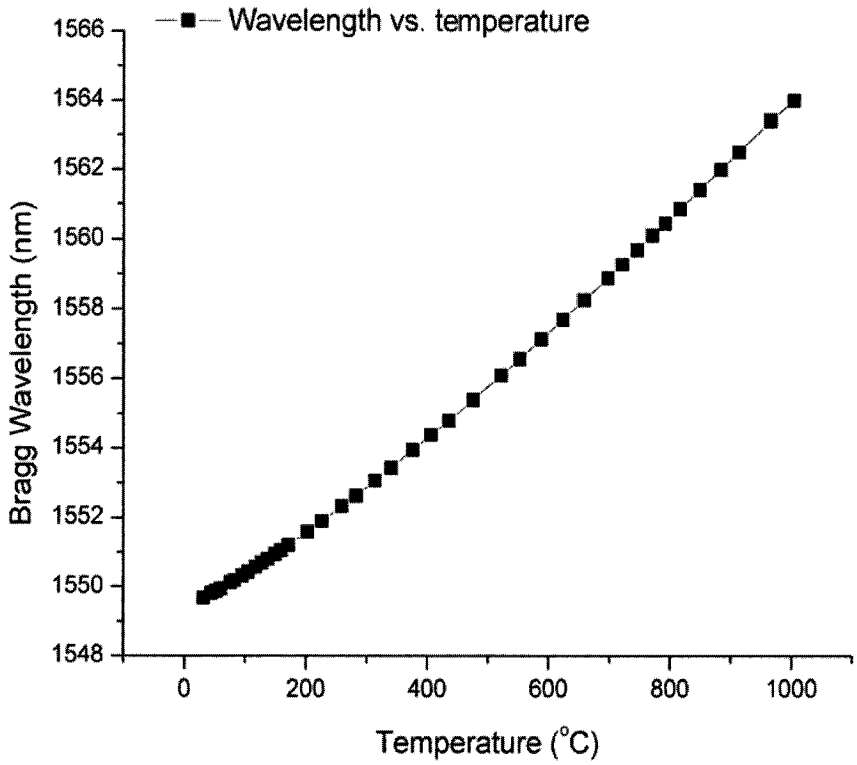

Figure 4.16 *Bragg wavelength versus temperature for molecular-water induced high temperature fiber Bragg grating from room temperature to 1000 °C.*

The temperature sensitivities of the gratings were determined by observing the change of Bragg wavelength with temperature. The spectral response of molecular-water induced high temperature FBG was displayed in Figure 4.16.

Figure 4.17 reveals the sensitivity of the Bragg wavelength for the high temperature FBG with respect to temperature. The sensitivity of the sensor at low temperatures is 0.009 nm/°C and changes to 0.0175 nm/°C at temperature around 1000 °C. This results show the sensitivity of the high temperature FBG is slightly higher than the conventional hydrogen loaded FBG (0.0166 nm/°C compare with 0.015 nm/°C [49] at temperature around 700 °C). As the Figure 4.17 shows, this variation of the sensitivity

with respect to temperature range between 600 °C to 1000 °C basically fits a linear model at high temperatures.

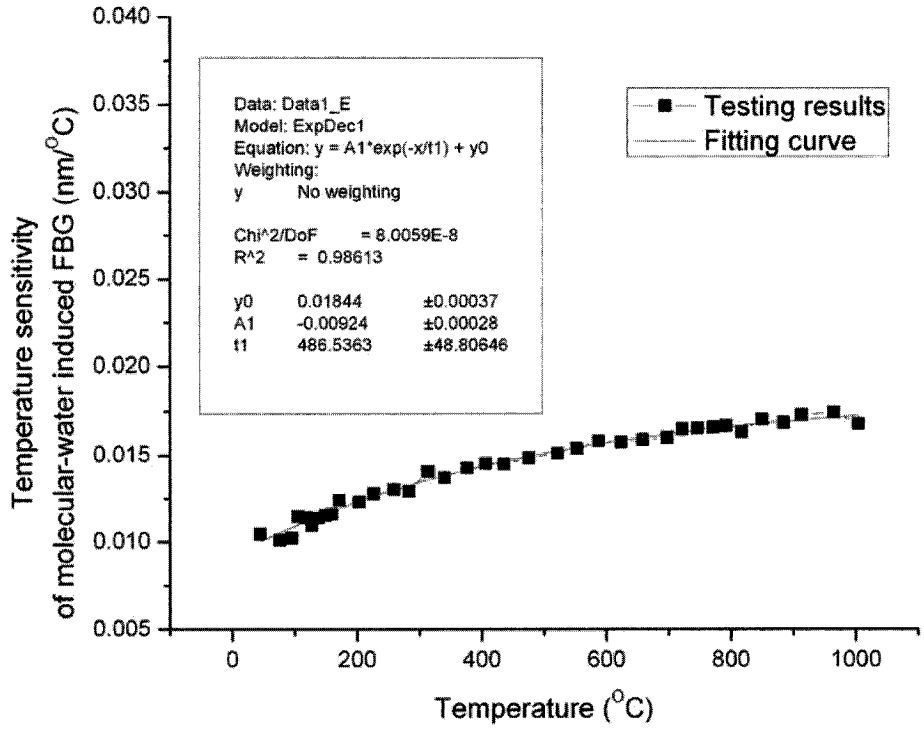

Figure 4.17 *Temperature sensitivity for molecular water induced high temperature fiber Bragg grating from room temperature to 1000 °C.*

Conclusion:

A high temperature resistance (from room to over 1000 °C) FBG temperature sensor based on the hydrogen-loaded FBG is designed, developed, and tested.

In this unique high temperature resistance FBG, its refractive index is formed by a periodic modulation of molecular-water inside the fiber core. The molecular-water induced FBGs were produced through hydrogen loaded conventional fiber with 248 nm UV laser as well as thermal processing technique. The recorded spectra show the tested

FBGs has thermal stability at high temperatures. The spectral response of tested FBG does not differ from hydrogen loaded FBGs.

Chapter 5 Microwave irradiation on the formation of molecular-water induced FBG

In this chapter, a novel microwave technique for high temperature resistance FBG temperature sensor is investigated both theoretically and experimentally. Especially, the effect of microwave irradiation on the parameters of FBGs for high temperature sensing application was studied.

5.1 Design of microwave irradiated hydrogen-loaded FBG

As we discussed before the decomposition of molecular-water is nearly impossible at the temperatures from the deep freeze to the melting temperature of silica [67] due to its strong bonding of the molecular-water. From this point of view, we can figure out the difference between the molecular-water FBG and the conventional FBG – the "bleach" temperature of the molecular-water FBG is much higher than the erasing temperature of conventional hydrogen loaded FBG. Also, the molecular-water has low diffusivity of inside the silica fiber. At high temperature range, the molecular-water will be diffused from the higher concentration segments to the lower concentration parts; however, this diffusion process is extremely slow. As a result, the molecular-water induced FBG has a much higher thermal stability compared to hydrogen loaded FBG.

According to Equation 4.3 and 4.5, high temperature resistance FBG can be fabricated using hydrogen-loaded FBG (reflectivity 31 dB, FWHM 0.5 nm) together with thermal annealing treatment at around 1000 °C. The fabrication of molecular-water induced FBG and recorded changes of Bragg reflectivity are shown in Figure 5.1. The mechanism of fabrication is the process of composite molecular-water in the FBG area.

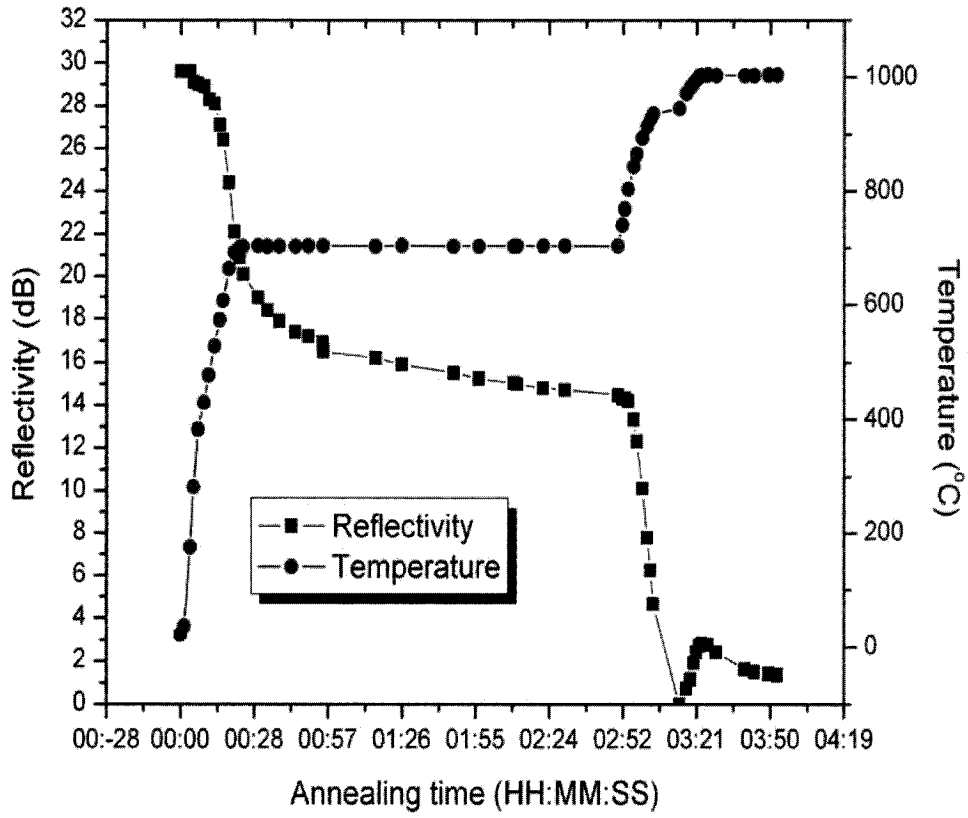

Figure 5.1 *The molecular-water induced reflectivity of FBG fabricated using hydrogen loaded FBG and thermal annealing processing.*

As our experiment results showed, the molecular-water induced FBG can be used to measure temperatures from room temperature to over 1000 °C. However, the low reflectivity (around 25% at 1000 °C, Figure 4.8) is its weak point. As we explained above, the main point of molecular-water induced FBG is concerned about the concentration of molecular-water inside a fiber core; the molecular-water is induced from the hydroxyl, which is produced by the dissociation of Ge-OH and Si-OH. From this point of view, we truly believe that the reflectivity of molecular-water induced FBG at high temperature environment is related to the amount of Si-OH (the concentration of Ge-OH is limited by the Ge doping concentration inside the optical fiber core) and also related to the hydrogen

loaded FBG reflectivity. Unfortunately, the reflectivity of hydrogen-loaded FBG is limited to around 35 dB, due to the vibration in the fabrication process. In order to increase the reflectivity of hydrogen-loaded FBG or to increase the concentration of Si-OH and Ge-OH, a new treatment should be applied to the hydrogen-loaded FBG.

We have focused our intentions to produce more hydroxyls in the FBG by changing water-molecules inside the fiber.

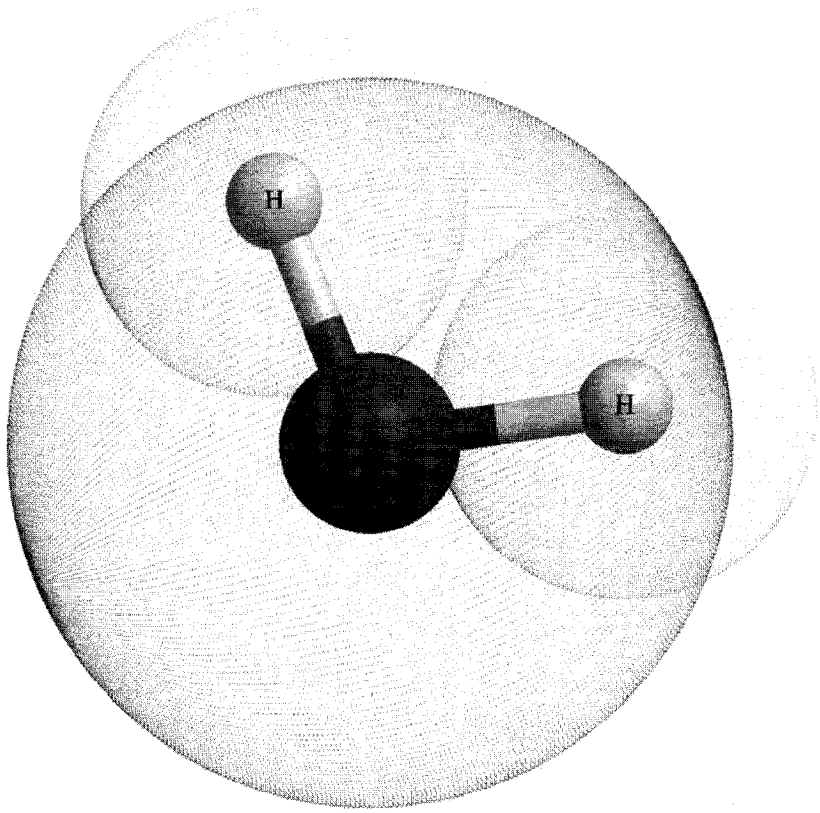

Figure 5.2 *The approximate shape of water-molecule.*

The water-molecule, Figure 5.2, is often described as having four, approximately tetrahedral arrangement, sp^3-hybridized electron pairs, two of which are associated with hydrogen atoms leaving the two remaining lone pairs [69]. In a perfect tetrahedral arrangement the bond-bond, bond-lone pair and lone pair-lone pair angles would all be

109.47° and such tetrahedral bonding patterns are found in condensed phases such as hexagonal ice.

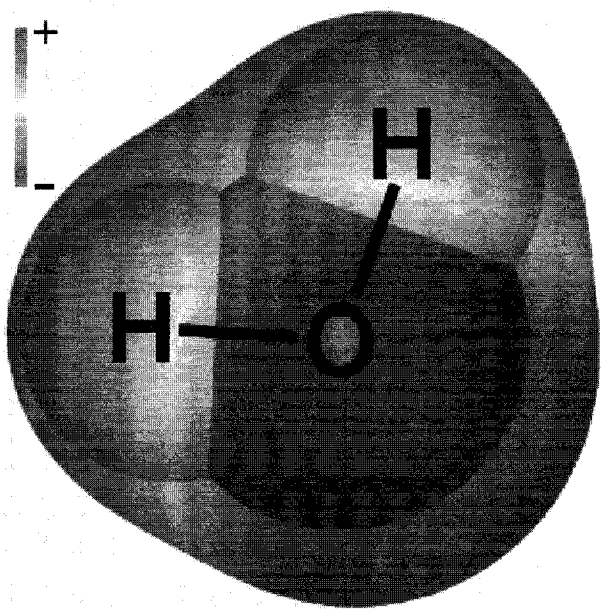

Figure 5.3 *The approximate charge distribution of water-molecule* [70].

The electron density distribution for water is shown Figure 5.3 [70]. The polarizability of the water-molecule is centered around the O-atom (1.4146 $Å^3$) with only small polarizabilities centered on the H-atoms (0.0836 $Å^3$). For an isolated water molecule, the calculated O-H length is 0.957854 Å and the H-O-H angle is 104.500°. The charge distribution depends significantly on the atomic geometry and the method for its calculation but is likely to be about -0.7e on the O-atom (with the equal but opposite positive charge equally divided between the H-atoms) for the isolated molecule. The experimental values for gaseous water molecule are O-H length 0.95718 Å, H-O-H angle 104.474°. These values are not maintained in liquid water, where ab initio (O-H length 0.991 Å, H-O-H angle 105.5°) and neutron diffraction studies (O-D length 0.970 Å, D-O-D angle 106°) suggest slightly greater values, which are caused by the hydrogen

bonding weakening the covalent bonding. These bond lengths and angles are likely to change, due to polarization shifts, in different hydrogen-bonded environments and when the water molecules are bound to solutes and ions. Commonly used molecular models use O-H lengths of between 0.957 Å and 1.00 Å and H-O-H angles of 104.52° to 109.5°.

The water-molecule is electrically neutral, but the positive and negative charges are not distributed uniformly. This is shown clearly by the gradation in color from green to purple in the Figure 5.3. The electronic (negative) charge is concentrated at the oxygen end of the molecule, owing partly to the nonbonding electrons, and to oxygen's high nuclear charge which exerts stronger attractions on the electrons. This charge displacement constitutes an electric dipole form the hydrogen side toward into oxygen side; you can think of this dipole as the electrical "image" of a water molecule.

As it is known, opposite charges attract, so the partially-positive hydrogen atom on one water-molecule is electrostatically attracted to the partially-negative oxygen on a neighboring molecule. This process is called (somewhat misleadingly) hydrogen bonding. Notice that the hydrogen bond is somewhat longer (117 pm) than the covalent O-H bond (99 pm). This means that it is considerably weaker; it is so weak, in fact, that a given hydrogen bond cannot survive for more than a tiny fraction of a second. However, if the water molecule is design to be vibrated and more close to the Si-O-Si, than it may result two Si-OH and shows in Figure 5.4.

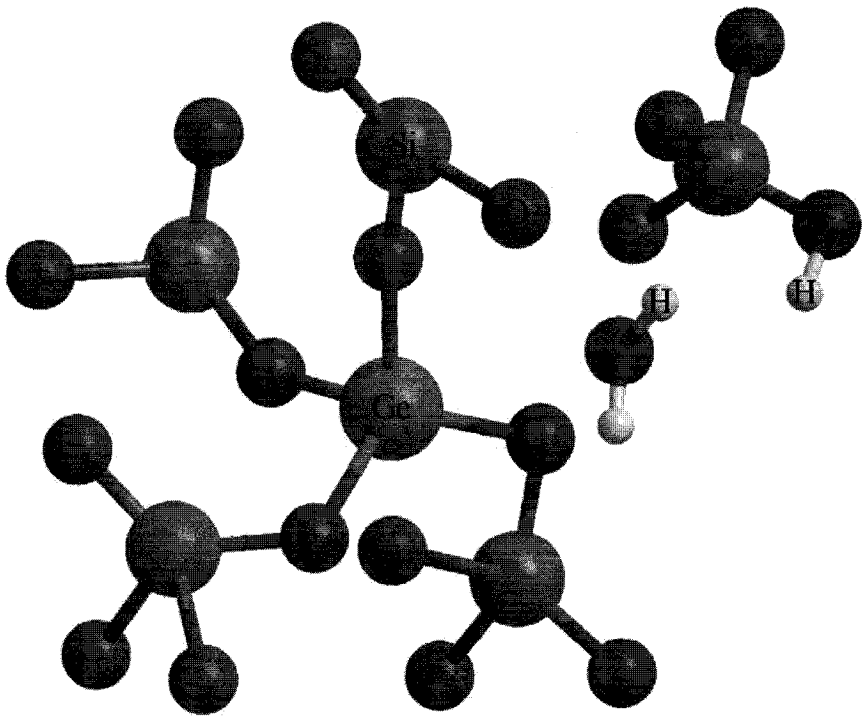

Model above shows the Ge-doped silica fiber with water impurity
Model below displays the reaction between water-molecule and Ge-doped silica

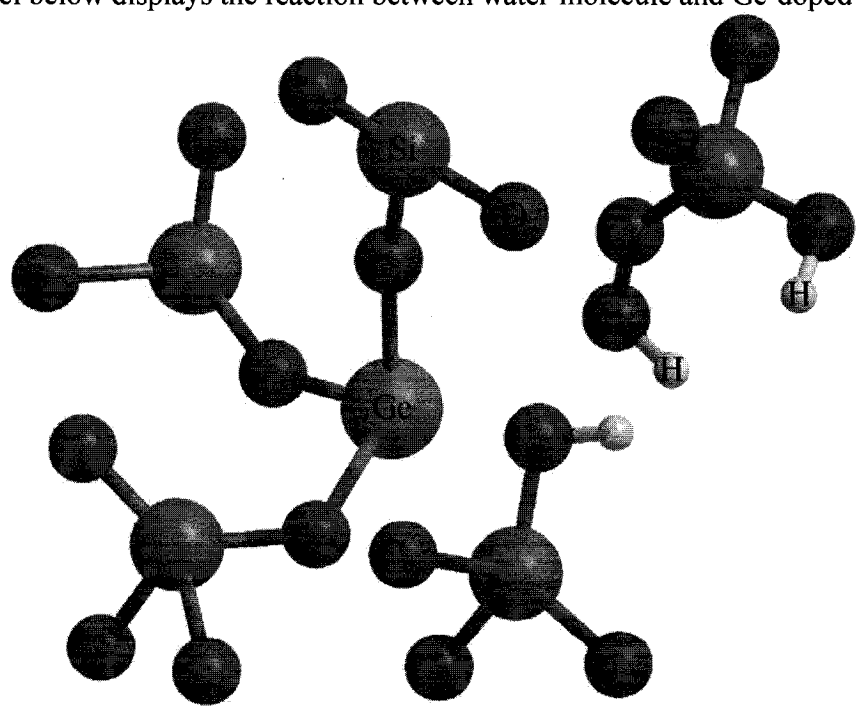

Figure 5.4 *The water molecule reacts with Ge doped silica to produce Si-OH and Ge-OH.*

Electromagnetic radiation in the microwave wavelengths (on the order of millimeters and centimeters) can be absorbed by water molecules. The way this happens, is that energy is transferred from the oscillation of electric and magnetic fields to the mechanical vibration of water molecules. There is a slight charge separation in these molecules, so they behave like small dipoles. Dipoles try to orient themselves with an external field (think of many magnetic needles being swung back and forth when you oscillate a large magnet above them), thus the molecules acquire kinetic energy.

In order to increase the Si-OH concentration, a new technique, which is microwave irradiation for the hydrogen-loaded FBG, was developed in our lab to fabricate the strong reflectivity hydrogen loaded FBG.

5.2 Experimental results

In fact, this new technique is a way to force the dissociation of impurity water in the fiber core, so that the Si-OH could be obtained in three reactions under microwave (Equation 5.1, 5.2, and 5.3). The water dipole attempts to continuously reorient in oscillating electric field. Depend on the frequency of electric field, the dipole may move to the field in time, lag behind it or remain apparently unaffected. When the dipole lags behind the field then interactions between the dipole and the field leads to an energy loss by heating. The re-orientation process may be modeled using a 'wait-and-switch' process where the water molecule has to wait for a period of time until favorable orientation of neighboring molecules occurs and then the hydrogen bonds switch to the new molecule. Furthermore, some of the molecular-water will be dissociated into H and OH [71], and re-bond with Si=O and Si-O-Si to produce more Si-OH. The possible reaction of

hydrogen loaded FBG under microwave irradiation are shown in Equation 5.1, 5.2, and 5.3.

$$H_2O \xrightarrow{Microwave} H + OH \tag{5.1}$$

$$Si = O \; + \; H \xrightarrow{Microwave} Si\text{-}OH \tag{5.2}$$

$$Si - O - Si \; + \; H - OH \xrightarrow{Microwave} 2(Si - OH) \tag{5.3}$$

The three hydrogen-loaded FBG samples mentioned in Table 5.1 were subjected to series of testing under the microwave irradiation.

In order to verify our theory for the increment of Si-OH and the FBG reflectivity after microwave irradiation, Sample A was placed inside Microwave (Goldstar 700W) for 5 min at maximum power level. The obtained 1.34 μm to 1.44 μm inferred absorption spectra for the Sample A before and after microwave irradiation are shown in Figure 5.5.

TABLE 5.1: PARAMETERS OF THE HYDROGEN-LOADED FBGS.

Parameter at room temperature	Sample A	Sample B	Sample C
Bragg wavelength λ_B	1550.145 nm	1550.03nm	1548.65nm
Initial reflectivity	15 dB	19 dB	27dB
Fiber type	SMF-28	SMF-28	SMF-28
FWHM	0.5 nm	0.45 nm	0.6 nm

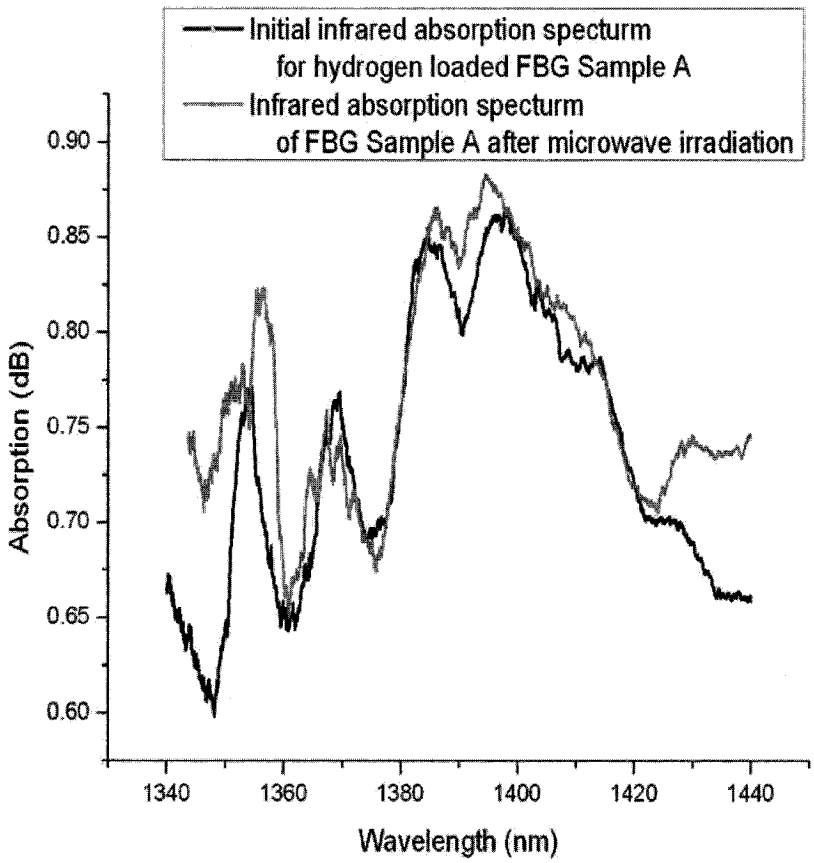

Figure 5.5 *Absorption spectra of hydrogen loaded FBG (Sample A) before (Black) and after (Grey) microwave irradiation in the range between 1.3 and 1.4 μm.*

The hydroxyl (OH) element is an essential component in the fabrication of molecular-water induced FBG and can be easily determined by their absorption in the infrared range. The fundamental absorption vibration band of OH is located at wavelength of 2.7 μm, while its first vibration overtone for Si-OH and Ge–OH absorption bands are 1.385 and 1.405 μm respectively [72]. Figure 5.5 shows clearly the increased Si-OH absorption at 1.385 μm, due to effect of microwave irradiation to the hydrogen-loaded FBG.

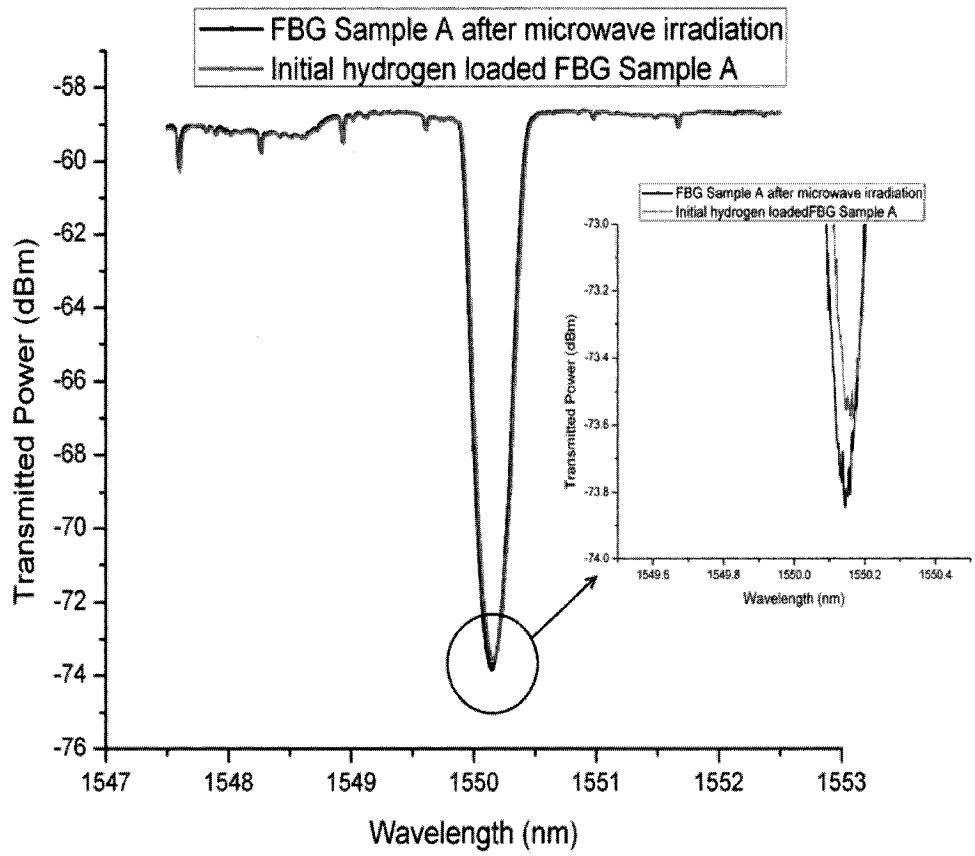

Figure 5.6 *Transmitted spectra of hydrogen-loaded FBG Sample A before (Grey) and after (Black).*

As we mentioned in Equation 4.3, the molecular-water can be also produced from Ge-OH. However, for the strong hydrogen-loaded FBG, Ge-OH absorption (1.405 μm) as well as Ge-OH concentration is limited by the germanium doping concentration inside fiber core [64]. Figure 5.5 shows peak Ge-OH absorption which is corresponding to our hypothesis – after microwave irradiation the peak Ge-OH absorption is not changed obviously. Figure 5.6 shows the change of FBG reflectivity before and after microwave irradiation.

As it can be seen from the Figure 5.6, the radiation influences the structure of glass and, therefore, the peak reflectivity (or the peak absorption) of the FBG was increased. The effect of microwave irradiation for the hydrogen loaded FBG is relied on the concentration of OH [73] and molecular water inside the hydrogen-loaded FBG, and also depends on the time of microwave irradiation to the FBG. Figure 5.7 shows a strong reflectivity change (ca. 8.5 dB) of Sample B after 7 minutes microwave irradiation.

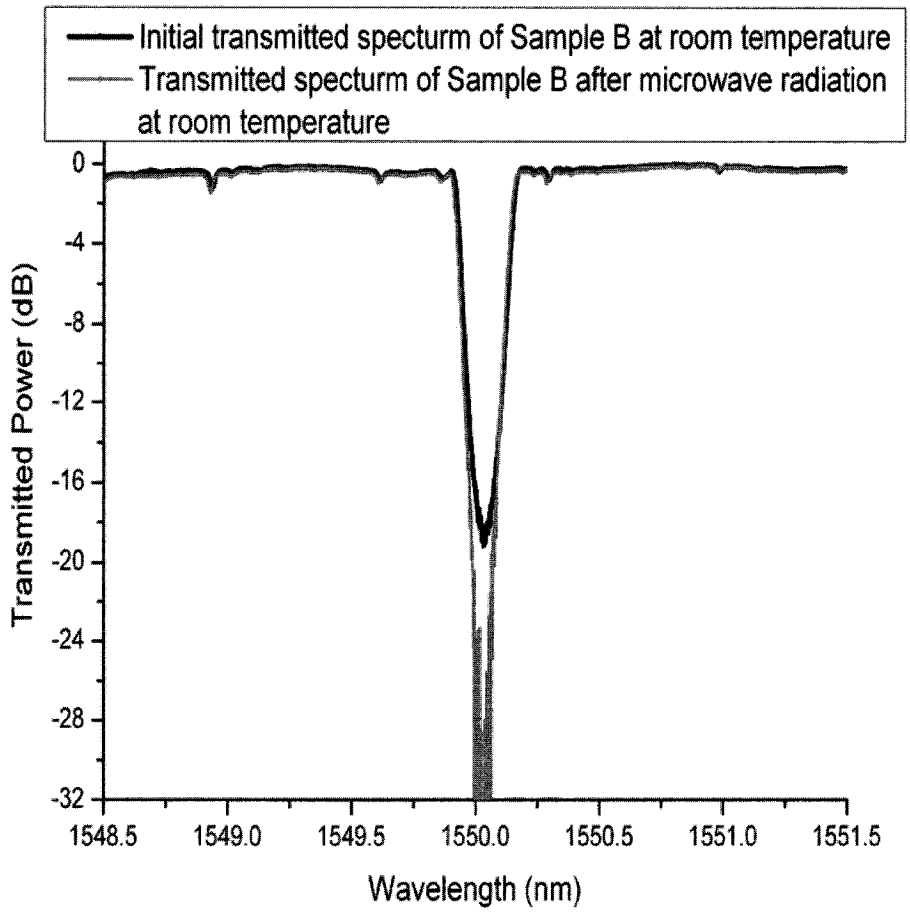

Figure 5.7 *Transmitted spectra of hydrogen loaded FBG (Sample B) before (Black) and after (Grey).*

We have showed in our previously [73] that, the reflectivity of molecular-water induced FBG is related to the amount of Si-OH inside the hydrogen-loaded FBG. As we mentioned in the Equation 4.3 and 4.5, the molecular-water is recomposed by the decomposition of Ge-OH and Si-OH. Based on this point, it's easily to see that the reflectivity of molecular-water induced FBG is related to the amount of Si-OH and indirectly related to the hydrogen loaded FBG reflectivity.

The sample C was microwave radiated for 15 minutes at maximum power. The spectrum of the microwave radiated hydrogen loaded FBG (Sample C) is shown in Figure 5.8.

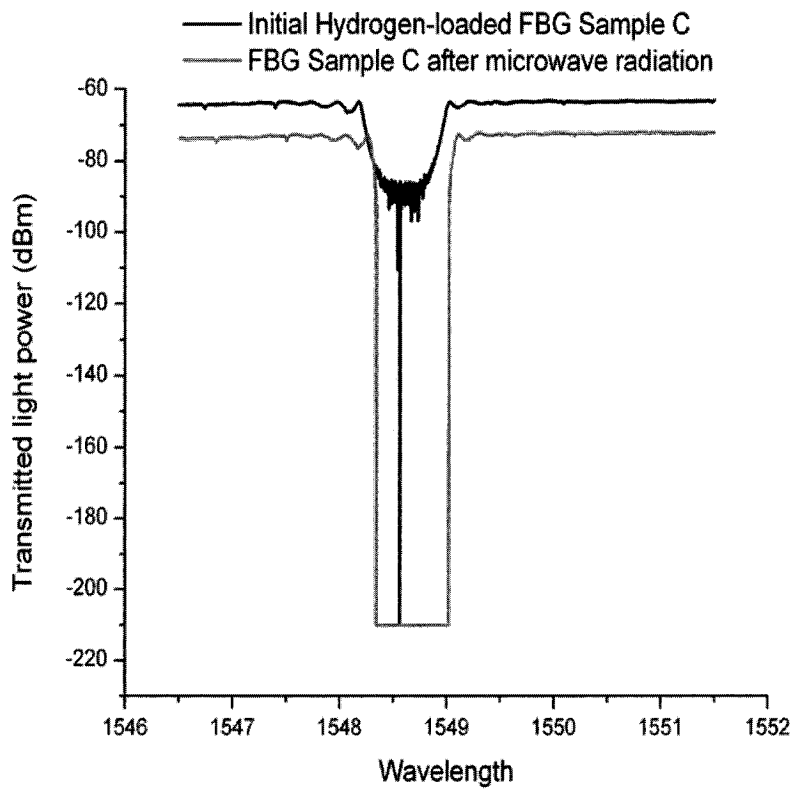

Figure 5.8 *Transmitted spectra of hydrogen loaded FBG (Sample C) before (Black) and after (Grey).*

The reflectivity of molecular-water induced FBG is contributed from the production of molecular-water inside the fiber core at high temperatures. In order to demonstrate the thermal behavior of the sample in the high temperature range, we displayed the recorded data from 200 °C to over 1100 °C, and the results are showing in 4.9.

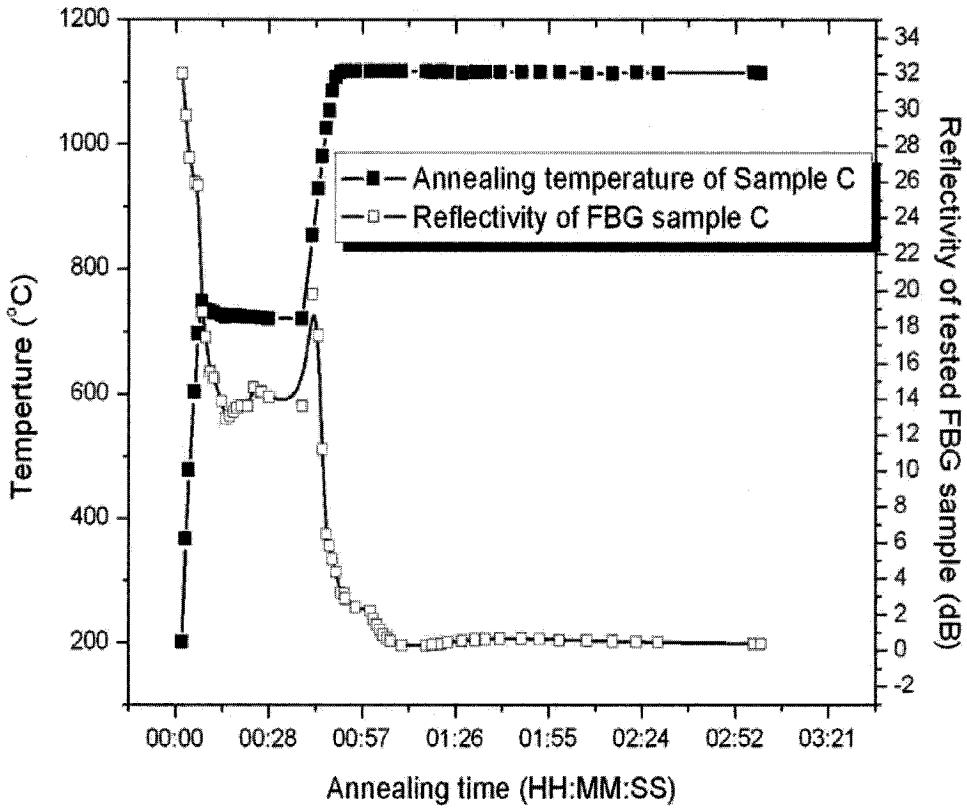

Figure 5.9 *The molecular-water induced reflectivity of FBG Sample C is fabricated by using microwave irradiated hydrogen-loaded FBG together with thermal processing.*

Comparing Figure 5.2 and Figure 5.9, at 200 °C, the reflectivity of microwave irradiated FBG was slightly (circa 4 dB) higher than the conventional FBG; When the annealing temperature was increased to 700 °C, the reduction of the reflectivity for both

fabrication processes of molecular-water induced FBG display the same decay characteristics. Once the annealing temperature was increased to 850 °C, a strong reflectivity increment (circa 6 dB) of the high reflectivity molecular-water induced FBG fabrication was observed.

The erasing point of the initial hydrogen loaded FBG was observed at 940 °C for hydrogen-loaded FBG in Figure 5.1, however, this erasing point was absent for the molecular-water induced FBG as shown in Figure 5.9. The highest testing temperature for molecular-water induced FBG is over 1100 °C. The reflectivity of Sample C remained 8.3% over two hours during 1100 °C isothermal annealing process.

Conclusion:

The Si-OH is an essential part for the high temperature resistance FBG, especially in the process of fabrication for molecular-water induced high temperature resistance FBG. Our experimental results showed that the Si-OH absorption increased after FBG was microwave irradiation. Also, changes of Bragg peak in the hydrogen-loaded germanium-doped FBG after microwave irradiation were observed. A strong reflectivity increment (circa 6 dB) of the molecular-water induced FBG was recorded at 1000 °C between microwave irradiated and un-irradiated FBGs during the high temperature comparison experiments; moreover, it was also observed that the highest erasing temperature for the microwave irradiated hydrogen-loaded FBG device could reach to 1100 °C.

Chapter 6 Discussion, contribution and future direction

6.1 Discussion and conclusions

FBGs are usually formed by a periodic change in the refractive index caused of a fiber core by exposure it to 248 nm UV laser [22]. Although FBGs are often referring to permanent refractive index structures and immunity to electric and magnetic filed, the properties of hydrogen-loaded FBGs can be modified using microwave irradiation technique [74].

The principle for the fabrication of hydrogen-loaded FBG is based on the structural changes from GODC to the DID, which is resulting a large amount of hydroxyl. Under microwave radiation, the hydroxyls will be vibrated along the rotated electric-magnetic field and result in the changes of FBG reflectivity. As indicated in Chapter 5, this is the first report for such a phenomenon in this field.

The reflectivity of high temperature resistance FBG, molecular-water induced FBG, is relying on the amount of molecular-water, which is generated from the composition of hydroxyl in the FBG area; however, the concentration of hydroxyls inside hydrogen-loaded FBG is limited by the vibration during the fabrication process. The maximum reflectivity of hydrogen-loaded FBG is around 35 dB [40].

The main topic of this research has been related to molecular-water induced FBG. The research has resulted in significantly better understanding of the underlying mechanism of the refractive index change, which has been attributed to changes in the molecular-water concentration in the fiber core. The mechanisms regarding thermal stability/decay of molecular-water induced FBG at high temperatures have also been

studied. The decay of molecular-water induced FBG is governed by molecular-water diffusion/decomposition and a model was developed to explain diffusion of molecular-water in the fiber core.

Molecular-water has played a central role in the fabrication of the high temperature sensor; however, the concentration of molecular-water is limited by the concentration of hydroxyls in these devices. To improve the reflectivity of "pure" molecular-water induced FBG, which is produced from hydrogen-loaded FBG; an innovative technique was developed. In order to have more water molecules to increase the FBG reflectivity, the application of microwave radiation on the production of molecular-water induced FBG is design and developed to generate more hydroxyls in FBG area of hydrogen-loaded FBG.

Studies on the dynamics of molecular-water formation have resulted in a proposed model for some of the mechanisms that occur during grating fabrication, and a method that can be used to manufacture these gratings in a reproducible manner has been provided.

The contributions of this thesis in the field of high-temperature sensors can be summarized as follows:

- For the first time the effect of microwave irradiation for the hydrogen-loaded FBG is reported. The performance of hydrogen-loaded FBG under this condition is investigated.
- It was shown that the concentration of Si-OH and Ge-OH can be increased in the core of hydrogen-loaded FBG using radiated microwave.

- It was shown that reflectivity of molecular-water induced FBG depends on the concentration of Si-OH and Ge-OH, and can be increased using microwave irradiation technique.
- Successfully, we achieved to fabricate the high temperature resistant FBG sensor that can be stable at temperature as high as 1100 °C.
- We found that hydrogen-loaded FBG is not immune to the EMI. It should be well protected, if it is used in an intense EMI field.

6.2 Future direction

The research outcomes presented in this thesis explain several properties of microwave effect on hydrogen-loaded FBG and molecular-water induced high temperature sensors; still, there are more issues that need to be studied.

- How to optimize the intensity of microwave radiation and the radiation time on the device performances?
- Protection of these devices when they are in use under harsh mechanical environment is another issue to be investigated.

References

1. Rebecca Stanfield, "Darkening Skies: Trends Toward Increasing Power Plant Emissions," April 4, 2002, U.S. PIRG Education Fund 218 D Street SE, Washington, DC (2003).
2. "The U.S. Greenhouse Gas Inventory," Greenhouse Gas Inventory Program Office of Atmospheric Programs U.S. Environmental Protection Agency (EPA), 1200 Pennsylvania Ave. NW (MS 6204J), Washington, DC 20460, USA (2005).
3. Human-Related Sources and Sinks of Carbon Dioxide, U.S. Enviromental Protection Agency, http://www.epa.gov/climatechange/emissions/co2_human.html.
4. Alex Gabbard, "Coal Combustion: Nuclear Resource or Danger?" ORNL Review, Vol.26, Nos.3 and 4, Summer/Fall 1993.
5. US Department of Energy, "Mercury Emissions and Controls Research and Development," 2006.
6. Ryoichi Okura, So Shioshita, Yasuyuki Kawasato, "Completion of High-efficiency Coal-fired Power Plant," Hitachi Review Vol. 52, No. 2, PP. pp. 79-83, 2003, Japan.
7. G.-N. Stamatelopoulos and E. Sadlon , "Advancement in coal-fired power plants: High Efficiency using Advance Meterials," ALSTOM, http://www.power.alstom.com/home/events/past_events/events_power_gen_europe/_files/file_19054_59459.pdf

8. Environmental Working Group, "Estimated mercury emissions from coal burning power plants," 2007
9. The Endress+Hauser group, www.endress.com (February 2006).
10. K. Natesan,A. Purohit, and D. L Rink,"Fireside Corrosion of Alloys for Combustion Power Plants," Argonne National Laboratory, Twenty-First annual International Pittsburgh coal Conference, Osaka, USA, September 13-17, 2004.
11. BHEL, Bhart Heavy Electricals Limited, www.BHEL.com
12. Sungchul Kim, Seungwoo Kim, Jaejoong Kwon, and Byoungho Lee,"Fiber Bragg Grating Strain Sensor Demodulator Using a Chirped Fiber Grating," IEEE Photonics Technology Letters, 13, pp. 839-841, (2001)
13. "Advancing Smart Sensing Specifications for FBG-based Sensor Arrays" LxSix Photonics, www.lxsix.com, 2005.
14. Byoungho Lee, "Review of the present status of optical fiber sensors," Optical Fiber Technology 9, pp. 57–79 (2003)
15. R. Kashyap, Fiber Bragg Gratings, Academic Press (1999).
16. A. Othonos and K. Kalli, Fiber Bragg Gratings: Fundamentals and Applications in Telecommunications and Sensing, Artech House, (1999).
17. N.M. Theune, M. Kaufmann, P. Krämmer, M. Willsch, T. Bosselmann, "Applications of Fiber Optical Sensors in Power Generators: Current and Temperature Sensors," Proceedings OPTO 2000 Conference, 22-25 May 2000.
18. Lars Gruener-Nielsen, Joerg Hueber, "Photosensitive fiber for highly reflective Bragg gratings," WL16, Technical Digest, Optical Fiber Comminication Conference (OFC97), 1997.

19. D.K.W. Lam and B.K. Garside, "Characterization of single-mode optical fiber filters." Applied Optics, 20 (3), pp. 440-445 (1981).

20. G. Meltz, W. W. Morey, W. H. Glenn, "Formation of Bragg gratings in optical fibers by transverse holographic method," Optics Letters, 14 (15), pp. 823-825 (1989).

21. P. St. J. Russell, J. L. Archambault, L. Reekie, "Fibre gratings," Physics World, pp. 41-46 October (1993).

22. K. O. Hill, Y. Fujii, D. C. Johnson, B. S. Kawasaki, "Photosensitivity in optical fiber waveguides: Application to reflection filter fabrication," Applied Physics Letters, 32(10), pp. 647-649 (1978).

23. I. Riant, "UV-photoinduced fibre gratings for gain equalisation," Optical Fiber Technology, 8, pp. 171-194, (2002).

24. M. Vengsarkar, P. J. Lemaire, J. B. Judkins, V. Bhatia, T. Erdogan, J. E. Sipe, "Long-period fiber gratings as band-rejection filter," Journal of Lightwave Technology, 14(1), pp. 58-65 (1996).

25. S. Choi, K. R. Kim, and K. Oh, "Interferometric inscription of surface relief gratings on optical fiber using azo polymer film," Applied Physics Letters, 83, pp. 1080-1082 (2003).

26. J.-L. Archambault, L. Reekie, P. St. J. Russel, "100% reflectivity Bragg reflectors produced in optical fibres by single excimer laser pulses," Electronics Letters, 29, pp. 453- 455 (1993).

27. D. Wiesmann, J. Hübner, R. Germann, I. Massarek, H.W.M. Salemink, G.L. Bona, M.Kristensen and H. Jäckel, "Large UV-induced negative index changes in

germanium-free nitrogen-doped planar SiO2 waveguides," Electronics Letters, 34, pp. 364 (1998).

28. M. Douay, W. X. Xie, T. Taunay, P. Bernage, P. Niay, P. Cordier, B. Poumellec, L. Dong, J. F. Bayon, H. Poignant, E. Delevaque, "Densification involved in the UV-based photosensitivity of silica glasses and optical fibers," Journal of Lightwave Technology, 15, pp. 1329-1342 (1997).
29. Akifumi Sakoh, Masahide Takahashi, Toshinobu Yoko, Junji Nishii, Hiroaki Nishiyama, Isamu Miyamoto, "Photochemical process of divalent germanium responsible for photorefractive index change in GeO2-SiO2 glasses." Optics Express, 11 (21), pp. 2679-2688 (October 2003).
30. R. M, Atkins, V. Mizrahi, and T. Erdogan, "248 nm induced vacuum UV spectral changes in optical fibre preform cores: support for a color centre model of photosensitivity," Electronics Letters, 29, pp. 385 –387 (1993).
31. R. M, Atkins, and V. Mizrahi, "Observations of changes in UV absorption bands of signal mode germamosilicate core optical fibres on writing and thermally erasing refractive index gratings," Electronics Letters, 28, pp. 1743-1744 (1992).
32. D. S. Starodubov, V. Grubsky, J. Feinberg, B. Kobrin, S. Juma, "Bragg grating fabrication in germanosilicate fibers by use of near-UV light: a new pathway for refractive index changes," Optics Letters, 22, pp. 1086-1088 (1997).
33. B. Malo, J. Albert, K.O. Hill, F. Bilodeau, and D.C. Jonson, "Effective index drift from molecular hydrogen diffusion in hydrogen-loaded optical fiber and its effect on Bragg grating fabrication," Electronics Letters, 30(5), pp. 442-444, (1994)

34. P. J. Lemaire, A. M. Vengsarkar, W. M. Reed, D. J. DiGiovanni, "Thermally enhanced ultraviolet photosensitivity in GeO2 and P2O5 doped optical fibers," Applied Physics Letters, 66, pp. 2034-2036 (1995).

35. E. Salik, D. S. Starodubov, V. Grubsky, and J. Feinberg "Increase of photosensitivity in Ge-doped fibers under strain," TuH5 - Fiber Bragg Gratings, Optical Fiber Comminication Conference (OFC2000), March 5-10, 2000.

36. D. L. Williams, B. J. Ainslie, J. R. Armitage, R. Kashyap, and R. Campbell, "Enhanced UV photosensitivity in boron codoped germanosilicate fibres," Electronics Letters, 29(1), pp. 45-47 (1993).

37. H.G. Limberger, P.Y. Fonjallaz,; R.P. Salathe, "Spectral characterisation of photoinduced high efficient Bragg gratings in standard telecommunication fibres," Electronics Letters, 29(1), pp. 47-49 (1993).

38. P. J. Lemaire, R. M. Atkins, V. Mizrahi and W. A. Reed, "High-pressure H2 loading as a technique for achieving ultrahigh uv photosensitivity and thermal sensitivity in GeO2 doped optical fibers," Electronics Letters, 29, pp. 1191-1193 (1993)

39. T Sun, S Pal, J Mandal, K T V Grattan, "Fibre Bragg grating fabrication using fluoride excimer laser for sensing and communication applications," School of Engineering, City University, Northampton Square, London, UK, Central Laser Facility Annual Report, pp. 147-149, (2001/2002)

40. Bragg Photonics Inc. 880 Selkirk, Pointe-Claire (QC) Canada

41. K. Noguchi, N. Shibata, N. Uesugi, and Y. Negishi, "Loss Increase for Optical Fibers Exposed to Hydrogen Atmosphere" Journal of Lightwave Technology, Volume 3, Issue 2, pp. 236 – 243, (Apr 1985).

42. Koichi Awazu, Hiroshi Kawazoe, and Masayuki Yamane, "Simultaneous generation of optical absorption bands at 5.14 and 0.452 eV in 9 SiO2 :GeO2 glasses heated under an H2 atmosphere." Journal of Applied Physics, 68(6) pp. 2713-2718 (1990).

43. Bowei Zahng, Mojtaba Kahrizi, "High Temperature Resistance Temperature Sensor Based on the Hydrogen Loaded Fiber Bragg Grating," IEEE Sensors 2005 Conference, Irvine, California, USA (Oct. 31 - Nov. 3, 2005).

44. V. Grubsky, D. S. Starodubov, J. Feinberg, "Photochemical reaction of hydrogen with germanosilicate glass initiated by 3.4-5.4-eV ultraviolet light," Optics Letters, 24, pp. 729-731 (1999).

45. J. Stone, "Interactions of Hydrogen and Deuterium with Silica Optical Fibers: A Review," Journal of Lightwave Technology, LT-5, pp. 712-733 (1987).

46. T. A. Nguty and R. J. Potton, "Photochemical changes in hydrogen-loaded optical fibres with application to Bragg grating formation," Measurement Science and Technology, 8, pp. 1055–1058 (1997).

47. A.D. Kersey, M.A. Davis, H.J. Patrick, M. LeBlanc, K.P. Koo, C.G. Askins, M.A. Putnam, and E.J. Friebele, "Fiber Bragg grating sensors," Journal of Lightwave Technology, 15, pp.1442 (1997).

48. Bowei Zhang, Mojtaba Kahrizi, "Wide range periodic waveguide temperature sensor," Proceeding of the Canadian Conference on Electrical and Computer Engineering (CCECE) 2003, pp. 117-121, Montreal, Canada, (2003).

49. B. Zhang and M. Kahrizi, "High-temperature Bragg grating waveguide sensor," Sensor Letters, Volume2, Number 2, pp. 113-116, June 2004.

50. Francis T.S. Yu and Shizhuo Yin, Fiber Optic Sensors, the Pennsylvania State University, University Park, PA, U.S.A., (2002).

51. A. D. Kersey, T. A. Berkoff, and W. W. Morey, "High-resolution fibre-grating based strain sensor with interferometric wavelength-shift detection," Electronics Letters, 28, pp. 236–238 (1992).

52. G. Brambilla, and H. N. Rutt, "Fiber Bragg gratings with enhanced thermal stability," Applied Physics Letters 80, pp. 3259-3261 (2002).

53. Tsung-Ein Tsai, Glen M. Williams, and E. Joseph Friebele, "Index structure of fiber Bragg gratings in Ge–SiO2 fibers," Optics Letters 22, pp. 224-226 (1997).

54. R.J. Egan, H.G. Inglis, P. Hill, Peter A. Krug, F. Ouellette, "Effects of hydrogen loading and grating strength on thermal stability of fiber Bragg gratings," in Technical Digest series on Conference on Optical Communications, OFC'96, Paper TuO3, pp. 83-84 (1996).

55. T. Erdogan, V. Mizrahi, P. J. Lemaire, and D. Monroe, "Decay of ultraviolet induced fiber Bragg gratings," Journal of Applied Physics, 1, pp. 73-80 (1994).

56. S. Kannan, J. Z. Y. Guo, P. J. Lemaire, "Thermal stability analysis of UV-induced fiber Bragg gratings," Journal of Lightwave Technolology, 15, pp. 1478-1483 (1997).

57. Photonics North 2004: Photonic Applications in Telecommunications, Sensors, Software, and Lasers. Edited by Armitage, John C.; Lessard, Roger A.; Lampropoulos, George A. Proceedings of the SPIE, Volume 5579, pp. 116-126 (2004).

58. A. K. Varshneya, Fundamentals of inorganic glasses, Academic press, 1994.

59. H. Hosono, J. Nishii, "High photosensitivity and nanometer-scale phase separation in GeO2-SiO2 glass thin films," Optics Letters, 24, pp. 1352-1354 (1999).

60. G. Brambilla, P. Hua, "Phase separation in highly-photosensitive tin-doped and codoped silica optical fibers and preforms," in Bragg gratings, Photosensitivity, and Poling in Glass waveguides, Paper BThA1, OSA, Italy (2001).

61. M. Fokine, "Formation of thermally stable chemical composition gratings in optical fibers," Journal of the Optical Society of America, B 19, pp. 1759-1765 (2002).

62. J. Kirchhof, S. Unger, H-J. Pißler, and B. Knappe, "Hydrogen-induced hydroxyl profiles in doped silica layers", OFC'95, Vol. 8, 1995 OSA Technical Digest Series, paper WP9.

63. B. Zhang and M. Kahrizi, "Thermal behavior of microwave irradiated hydrogen loaded fiber Bragg grating," Journal of Applied Physics, submitted.

64. Bowei Zhang and Mojtaba Kahrizi, "Hydrogen loaded fiber Bragg grating for high temperature sensor applications," Proceedings of SPIE -- Volume 5579, Photonics North 2004, November 2004, pp. 116-126.

65. Youlong Yu and Hwayaw Tam, A technique for enhancing the thermal stability of hydrogen-loaded fiber Bragg grating, Chinese Optics Letters, 1, pp. 256-258 (2003).

66. Bowei Zhang, "High temperature sensors based on hydrogen loaded fiber Bragg gratings," Thesis for the Degree of Master of Applied Science in the Department of Electrical and Computer Engineering of Concordia University (2004).

67. M. Tomozawa, D-L. Kim and V.L. Lou, "Preparation of High Purity, Low Water Content Fused Silica Glass," GE Research & Development Center, Class1, 2001CRD184, December 2001.

68. K. M. Davis and M. Tomozawa, "Water diffusion into silica glass: Structural changes in silica glass and their effect on water solubility and diffusivity," Journal of Non-Crystalline Solids, Volume 185, Issue 3, pp. 203-220, 1 June 1995.

69. http://en.wikipedia.org/wiki/Water_(molecule)

70. http://www.lsbu.ac.uk/water/molecule.html

71. Vaks V. L., Domrachev G. A., Rodygin Yu. I., Selivanovskii D. A., Spivak E. I.," Dissociation of water by microwave radiation," Russian acad. sci., inst. applied physics, URSS, Volume 37, Number 1, pp. 85-88 (9 ref.), 1994.

72. V. Grubsky, D.S. Starodubov and J. Feinberg, Contributed talk, "Effect of molecular water on thermal stability of gratings in hydrogen-loaded optical fibers," Optical Fiber Communication Conference, San Diego, California, February 21-26, 1999.

73. Bowei Zhang and Mojtaba Kahrizi, "High Temperature Resistance Fiber Bragg grating temperature sensor Fabrication," IEEE Sensors Journal, Vol. 7, No. 4, pp. 586-591, April 2007.

74. Bowei Zhang and Mojtaba Kahrizi, "Fabrication of high temperature resistant fiber Bragg grating using microwave irradiated hydrogen-loaded fiber Bragg," Applied Optics, submitted.

Glossary

DID	Draw Induced Defect; A trapped hole with an oxygen vacancy
EMI	Electromagnetic interference
FBG	Fiber Bragg grating
Ge-OH	Germanium Hydroxyl
GODC	Germanium Oxygen Deficient Center
MCVD	Modified Chemical Vapour Deposition
Si-OH	Silicon Hydroxyl
VAD	Vapor (Phase) Axial Deposition